

Peter Heftberger

Structure and elasticity of fluid membrane domains

Doctoral Thesis

For obtaining the academic degree of
Doktor der technischen Wissenschaften

Doctoral Programme of Technical Sciences
Technical Physics



Graz University of Technology

Supervisor:
Assoc.-Prof. Dr. Georg Pabst

Institute of Materials Physics
in cooperation with: Institute of Molecular Biosciences, University of Graz

Graz, April 2015

EIDESSTATTLICHE ERKLÄRUNG

AFFIDAVIT

Ich erkläre an Eides statt, dass ich die vorliegende Arbeit selbstständig verfasst, andere als die angegebenen Quellen/Hilfsmittel nicht benutzt, und die den benutzten Quellen wörtlich und inhaltlich entnommenen Stellen als solche kenntlich gemacht habe. Das in TUGRAZonline hochgeladene Textdokument ist mit der vorliegenden Dissertation identisch.

I declare that I have authored this thesis independently, that I have not used other than the declared sources/resources, and that I have explicitly indicated all material which has been quoted either literally or by content from the sources used. The text document uploaded to TUGRAZonline is identical to the present doctoral dissertation.

Datum / Date

Unterschrift / Signature

Acknowledgment

First and foremost I would like to thank my advisor Georg Pabst for supporting and encouraging me and our research that we have been doing in the past three years. I learned a lot from his knowledge and experiences in biophysics and scattering techniques, and from the way he is doing science. I am also thankful for all the trips to other labs and conferences that Georg supported, where I got to know so many new colleagues and friends. Georg is not only a great scientist and advisor but also a great person and I really enjoyed working with him. I also enjoyed sharing the same office with Benjamin for three years, where we had enthusiastic, useful and entertaining discussions about our science and other things. Benjamin is a great physicist and friend, and therefore working and traveling with him was always interesting and particularly great fun.

I further would like to thank Karl Lohner as he always took time to answer questions about my research and to discuss and encourage my research. I also want to thank all other group members for their help especially in chemistry issues and the general helpful and friendly working environment.

Benjamin and I took also part in the "asymmetry-project" and therefore I want to thank all the collaborators and friends for the amazing, exhausting and funky beamtimes we had in Oak Ridge, Hamburg and Lund: Fred, Milka, Jonathan, Drew, Erwin, JK, Rob and Scatter Monkey. Special thanks to Fred for SANS measurements and all the enjoyable discussions about domains, scattering, Baseball...

I wish to thank my girlfriend Regina, for her general support and her understanding during the last three years and especially during the last weeks; and thank you for reviewing my thesis.

Abstract

Based on the scattering density profile (SDP) model that is used to analyze small angle neutron and x-ray scattering data (SANS and SAXS) of unilamellar vesicles (ULVs), a high resolution analysis technique for the analysis of SAXS and SANS data from multilamellar vesicles (MLVs) as well as from ULVs has been developed. It is capable of obtaining high resolution structural as well as elastic information about homogeneous bilayers from standalone x-ray data as well as from a joint analysis of SAXS and SANS data, using a genetic algorithm for a robust optimization procedure. The analysis was tested against several phosphatidylcholine lipids with and without cholesterol. Results such as bilayer thickness and area per lipid compare well with previously reported results from a joint SAXS/SANS SDP analysis of ULVs. The addition of SANS data to the analysis slightly improved lipid backbone information but did not have a significant impact on overall structural properties, such as bilayer thickness and area per lipid.

This technique was further enhanced to analyze SAXS data from co-existing liquid ordered and disordered (L_o/L_d) domains in MLVs in order to get a deeper biophysical understanding of the lipid raft phenomena in cell membranes. Therefore the analysis enables to compare structural and elastic properties, such as bilayer thickness, hydrocarbon chain length, area per lipid and bending fluctuations between coexisting L_o/L_d phases in situ of two ternary lipid mixtures DOPC/DSPC/CHOL and DOPC/DPPC/CHOL. A height mismatch between L_o and L_d domains of $\sim 10 \text{ \AA}$ and a decrease in area per lipid of $\sim 20 \text{ \AA}^2$ as well as in bending fluctuations of $\sim 65\%$ for the more condensed L_o domains was found. Further on, the impact of lipid composition and cholesterol concentration on L_o/L_d domains was studied and interestingly, additional cholesterol significantly affects the properties of the L_d phase while the

CHOL enriched L_o domains remain nearly unaffected. Finally, the melting of L_o domains as a function of temperature was examined and the results revealed a cholesterol diffusion to L_d domains accompanied by a decrease of L_o/L_d domain height mismatch.

Structural properties were further on studied as a function of domain size in the four component mixture POPC/DOPC/DSPC/CHOL. By exchanging POPC by DOPC, the domain size increases from nanoscopic to macroscopic, accompanied by an alignment of domains across bilayers in MLVs. To obtain structural information of non-aligned coexisting nanoscopic domains, the SAXS data analysis was further enhanced and the results revealed a different behavior of bilayer thickness, area per lipid and domain height mismatch between nanoscopic and macroscopic domains as a function of domain size. The increase of height mismatch between L_o/L_d domains in the nano domain regime was found to be five times steeper than in the macro domain regime, supporting line tension theory that controls domain size. The height mismatch decrease for shrinking L_d domains is mainly attributed to a thickening of nanoscopic L_d domains that could be understood by a squeezing of domains due to their L_o surrounding. The strong decrease in area per lipid for nanoscopic domains is also a result of this potential "squeezing effect".

Kurzfassung

Ein Modell für Streulängendichten (SDP), zur Analyse von Röntgen- und Neutronenstreudaten von unilamellaren Lipid Vesikeln (ULVs), wurde weiterentwickelt um auch Streudaten von multilamellaren Vesikeln (MLVs) analysieren zu können. Die Optimierung der Modellparameter gegen die experimentellen Streudaten basiert auf einem genetischen Algorithmus, womit es möglich ist detaillierte Informationen über die Struktur und die Elastizität von homogenen Lipid Membranen zu erhalten. Die Methode kann entweder auf Röntgendaten alleine, oder auf Röntgen- und Neutronendaten gemeinsam angewendet werden. Um die Analysemethode zu verifizieren, wurden strukturelle Parameter, wie Membrandicke und Fläche pro Lipid, von vier verschiedenen Phosphatidylcholine Lipiden und von binären Mischungen mit Cholesterin bestimmt und mit bereits publizierten Resultaten einer SDP Analyse von ULVs verglichen. Die Werte stimmten innerhalb berechneter Unsicherheiten überein, wobei die Kettenlänge des Lipids und die Position des Lipid-Rückgrates, nach Berücksichtigung zusätzlicher Neutronendaten in der Analyse, besser bestimmt waren, ohne jedoch gesamtheitliche Parameter wie Membrandicke und Fläche pro Lipid beeinflusst zu haben.

Diese Analysetechnik wurde wieder weiterentwickelt, damit auch Röntgenstreudaten von koexistierenden flüssig geordneten und ungeordneten Domänen (L_o/L_d) in multilamellaren Vesikeln analysiert werden können, um einen tieferen Einblick in die physikalische Natur von "lipid rafts" in Zellmembranen zu bekommen. Strukturelle und elastische Eigenschaften von koexistierenden L_o/L_d Domänen, wie Membrandicke, Kettenlänge, Fläche pro Lipid und Biegefluktuationen, konnten nun mit Hilfe dieser Methode für zwei ternäre Mischungen DOPC/DSPC/CHOL und DOPC/DPPC/CHOL bestimmt werden. Der Höhenunterschied zwischen L_o und den dünneren L_d Domänen beträgt $\sim 10 \text{ \AA}$, des Weiteren weisen

die L_o Domänen einen um $\sim 20 \text{ \AA}^2$ kleineren Wert für die Fläche pro Lipid auf und zeigen um $\sim 65 \%$ geringere Biegefluktuationen. Auch wurde der Einfluss von Lipid Kompositionen und Cholesterin auf L_o/L_d Domänen bestimmt, wobei Cholesterin vor allem die Eigenschaften von L_d Domänen beeinflusst hat. Schließlich wurden die Eigenschaften und das Schmelzen von L_o Domänen in Abhängigkeit von der Temperatur untersucht. Aufgrund der Ergebnisse, wie der Verringerung des Höhenunterschiedes zwischen L_o und L_d Domänen, konnte auf eine mögliche Diffusion von Cholesterin zu L_d Domänen geschlossen werden.

Strukturelle Eigenschaften von Domänen wurden auch als Funktion ihrer Größe untersucht. Als Modellsystem wurde das vier Komponenten System POPC/DOPC/DSPC/CHOL verwendet, bei dem die L_d Domänengröße durch den kontinuierlichen Austausch von POPC mit DOPC, von nanoskopisch bis makroskopisch variiert werden kann, das letztendlich auch zu einer vertikalen Überlagerung von Domänen führt. Um auch strukturelle Information über nanoskopische Domänen zu erhalten, die keine vertikale Ordnung aufweisen, wurde die Analysemethode wieder weiterentwickelt und angepasst. Die Resultate zeigen ein unterschiedliches Verhalten von nanoskopischen und makroskopischen Domänen als Funktion ihrer Größe hinsichtlich Membrandicke, Fläche pro Lipid und L_o/L_d Höhenunterschied, welcher im Nanodomänen Bereich fünfmal stärker ansteigt als im Makrodomänen Bereich. Kleiner werdende L_d Domänen zeigen auch einen Anstieg in der Membrandicke und einen Abfall in der Fläche pro Lipid, das durch das laterale Zusammendrücken der L_d Domänen durch ihre L_o Umgebung erklärt werden kann.

Contents

Abstract	vii
Kurzfassung	ix
List of Figures	xv
List of Tables	xix
List of Abbreviations	xxi
1. Introduction	1
1.1. Cell membrane and lipid rafts	1
1.2. Lipid bilayer models	5
1.2.1. The effect of cholesterol on lipid bilayers	6
1.2.2. Binary lipid mixtures	8
1.2.3. Ternary lipid mixtures	10
1.2.4. Phase behavior of multicomponent lipid membranes	13
1.2.5. On domain size, critical fluctuations and microemul- sion of complex lipid mixtures	14
1.2.6. L_o/L_d domain size as a function of lipid composition	18
1.2.7. Protein partitioning and function in L_o/L_d phases .	21
1.3. Experimental methods to examine lipid domains	23
2. Methods	27
2.1. Scattering techniques	27
2.1.1. Small angle x-ray scattering (SAXS)	27
2.1.2. Small angle neutron scattering (SANS)	29
2.2. Scattering density profile model (SDP-analysis for MLVs) .	31
2.2.1. Parsing scheme for phosphatidylcholine lipids	32

Contents

2.2.2.	Incorporation of cholesterol in the SDP model	36
2.2.3.	SDP analysis for MLVs	38
2.2.4.	Constraining the free parameter space	40
2.2.5.	Determination of bilayer structural parameters	42
2.2.6.	Optimization routine based on the genetic algorithm	43
2.2.7.	Joint refinement of small angle x-ray and neutron scattering	45
2.3.	SDP-GAP analysis for phase separated bilayer mixtures	47
2.3.1.	Parsing scheme for lipid mixtures	48
2.3.2.	Analysis of aligned L_o/L_d domains	50
2.3.3.	Analysis of non-aligned coexisting L_o/L_d domains	52
2.3.4.	Determination of area per lipid for complex lipid mixtures	53
3.	Results and Discussion	57
3.1.	High resolution SAXS and SANS data analysis of homogeneous lipid mixtures containing cholesterol	57
3.1.1.	SDP-GAP analysis for x-ray data only	57
3.1.2.	The effect of cholesterol on saturated and unsaturated PC lipids	59
3.1.3.	Joint analysis of SAXS and SANS data	60
3.2.	Structural and elastic properties of coexisting L_o/L_d domains in three component lipid mixtures	62
3.2.1.	Global SAXS data analysis for coexisting fluid membrane domains in MLVs	63
3.2.2.	Cholesterol affects intra- and interbilayer structure of L_o/L_d membrane domains	66
3.2.3.	The influence of temperature on coexisting L_o/L_d domains	67
3.3.	Influence of domain size on coexisting L_o/L_d domains in complex lipid mixtures	70
3.3.1.	Lipid composition and x-ray scattering profiles	70
3.3.2.	Coexisting liquid domains behave differently than their corresponding pure L_o and L_d phases	73
3.3.3.	Structural bilayer properties as a function of domain size	75

3.3.4. Correlation between domain size and domain height mismatch	77
3.3.5. Bending fluctuations and the increase in L_d phase fraction	79
3.3.6. Temperature dependent behavior of L_o/L_d domains and their influence on the critical temperature	81
4. Conclusion	87
5. Outlook	91
Bibliography	93
A. First author papers	117
B. Co-authored papers	119
C. Scientific publications	121

List of Figures

1.1.	Cell structure and components.	2
1.2.	Schematic representation of a lipid bilayer and the chemical structure of a glycerophospholipid molecule.	3
1.3.	Fluid mosaic model of a cell membrane by Singer and Nicholson.	4
1.4.	Hypothetical model for plasma membrane compartmentalization.	5
1.5.	Schematic illustration of supported bilayers and liposomes.	6
1.6.	Schematic representation of structures of lamellar lipid phases.	7
1.7.	Generic phase diagrams for binary lipid mixtures with and without cholesterol.	9
1.8.	Ternary phase diagram of a low, a high melting temperature lipid and cholesterol.	11
1.9.	Schematic representation of lipid domain alignment.	15
1.10.	Domain formation in giant unilamellar vesicles across the critical temperature T_C	17
1.11.	Phase behavior of liquid domains in complex lipid mixtures.	18
1.12.	DOPC/POPC exchange rate ρ_{DOPC} controls domain size.	20
2.1.	X-ray and neutron scattering cross sections.	28
2.2.	Schematic representation of a SAXS experiment.	30
2.3.	Contrast matching in neutron scattering experiments.	31
2.4.	ED/NSLD profile of a DOPC bilayer from MD-simulations.	34
2.5.	Generic parsing scheme (upper panel) and volume probability distribution (lower panel) for DPPC.	35
2.6.	Cholesterol-lipid interactions shown by MD-simulations.	36
2.7.	Volume probability distribution of a PC bilayer containing cholesterol.	37

List of Figures

2.8.	Schematic representation of bilayer undulations.	39
2.9.	Various Structure factors for different numbers of bilayer stacks N	41
2.10.	Illustration of bilayer structural properties.	42
2.11.	Chemical representation of POPC (A) and POPC-d ₃₁ (B).	47
2.12.	Schematic representation of a SAXS experiment for L_o/L_d phase coexistence.	48
2.13.	Parsing scheme of the DOPC/DPPC/CHOL (0.12/0.58/0.30) lipid mixture (L_o phase) based in MD-simulations.	49
2.14.	Illustration of structure and form factors of L_o/L_d phases.	51
2.15.	Cartoon of aligned (A) and unaligned (B) L_o (grey) and L_d (black) domains.	52
2.16.	Estimated tieline endpoint behavior as a function of temperature for DOPC/DSPC/CHOL (A) and DOPC/DPPC/CHOL (B).	55
3.1.	SAXS data analysis of SOPC MLVs at 30 °C.	58
3.2.	Joint analysis of SAXS and SANS data from POPC uni- and multilamellar vesicles at 30 °C.	61
3.3.	Overview of lipid compositions examined in this work (black circles).	63
3.4.	Global SAXS data analysis for coexisting L_o/L_d domains of tieline midpoint sample A_{t1} at 22 °C.	64
3.5.	Temperature behavior of A_{t2} midpoint sample.	67
3.6.	Bilayer thickness d_B as a function of temperature for tieline midpoint samples A_{t1} (squares) and B_{t1} (triangles).	68
3.7.	Global SAXS data analysis of coexisting liquid nano (A) and macro (B) domains at 20 °C.	72
3.8.	Comparison of lamellar repeat distance d between endpoints (triangles) and midpoints (squares) as a function of ρ_{DOPC}	74
3.9.	Comparison of bilayer thickness d_B between endpoints (triangles) and midpoints (squares) as a function of ρ_{DOPC}	75
3.10.	Comparison of lateral area per lipid A between endpoints (triangles) and midpoints (squares) as a function of ρ_{DOPC}	76

List of Figures

3.11. Comparison of L_o/L_d domain height mismatch Δd_B between endpoints (triangles) and midpoints (squares) as a function of ρ_{DOPC}	77
3.12. Comparison of bending fluctuations η between endpoints (triangles) and midpoints (squares) as a function of ρ_{DOPC}	79
3.13. L_d phase fraction of coexisting phases as a function of ρ_{DOPC}	80
3.14. Temperature dependent bilayer thickness d_B of coexisting L_o (grey triangles) and L_d (open squares) domains.	82
3.15. Temperature dependent water layer thickness d_W between L_o (grey triangles) and L_d (open squares) domains.	84

List of Tables

3.1. Overview of lipid compositions (molar fractions) studied in this work according to the published compositional phase diagram DOPC/POPC/DSPC/CHOL [1].	71
3.2. Dependence of the critical exponent β on T_C	85

List of Abbreviations

L_d	liquid disordered phase
L_d	liquid disordered
L_o	liquid ordered
L_α	liquid crystalline phase
L_β	gel phase
L'_β	solid ordered
L_o	liquid ordered phase
CH_2	methylene
CH_3	methyl
AFM	atomic force microscopy
CH	methine
CHOL	cholesterol
DOPC	1,2-dioleoyl- <i>sn</i> -glycero-3-phosphocholine
DPPC	1,2-dipalmitoyl- <i>sn</i> -glycero-3-phosphocholine
DRM	detergent resistant membrane
DSM	detergent soluble membrane
DSPC	1,2-dioctadecanoyl- <i>sn</i> -glycero-3-phosphocholine
ED	electron density
ESR	electron spin resonance spectroscopy
FRET	Förster resonance energy transfer
GA	genetic algorithm
GAP	global analysis program
GUV	giant unilamellar vesicle
H-bond	hydrogen bond
IDL	Interactive Data Language

List of Abbreviations

MCT	modified Caillé theory
MD	molecular dynamic
MLV	multilamellar vesicle
NMR	nuclear magnetic resonance
NSLD	neutron scattering length density
pBSM	porcine brain sphingomyelin
PC	phosphatidylcholine
PE	phosphatidyletanolamine
POPC	1-palmitoyl-2-oleoyl- <i>sn</i> -glycero-3-phosphocholine
PS	phosphatidylserine
PSM	N-palmitoyl sphingomyelin
SANS	small angle neutron scattering
SAXS	small angle x-ray scattering
SDP	scattering density profile
SLD	scattering length density
SM	sphingomyelin
ULV	unilamellar vesicle
VP	volume probability

1. Introduction

1.1. Cell membrane and lipid rafts

The cell membrane is more than just a structural assembly designed to separate the interior of a cell, the cytoplasm, from the outside (Fig. 1.1). It is a complex and flexible two dimensional liquid that contains more than 1000 different lipid species and proteins [2]. The cytoplasm is an even more complex construct containing the most important parts of a cell, such as the nucleus, endoplasmatic reticulum, mitochondria, ribosomes and the Golgi complex to name but a few [3]. In this interior of the cell plasma membranes can also be found as the outer shell of organelles. Membranes have different functions, which are important for the execution and regulation of biological processes, such as transportation, cell defense and adhesion, as well as cell-cell signaling. The major group of lipid species in the plasmamembrane are glycerophospholipids, which are represented by a choline group, a phosphate group, a glycerol group, and two fatty acid chains (Fig. 1.2 C,D). Lipids can be illustrated in a very simple way as it is shown in Fig. 1.2 B, where the hydrophilic polar head is shown in green and the second part, the apolar hydrophobic tail, is shown in purple. A lipid bilayer as it is shown schematically in Fig. 1.2 A is then formed by the asymmetric alignment of two lipid layers (leaflets), where the headgroups are exposed to water and the hydrocarbon chains form an oil-like phase packed inner part of the bilayer [4]. Another component of the membrane is cholesterol that accounts for about 20–50 % of all lipids and is important for the fluidity of membranes and for the function of membrane proteins [5].

The bulk plasma membrane can be described as a fluid mosaic model with proteins embedded in the bilayer (Fig. 1.3), which was proposed by

1. Introduction

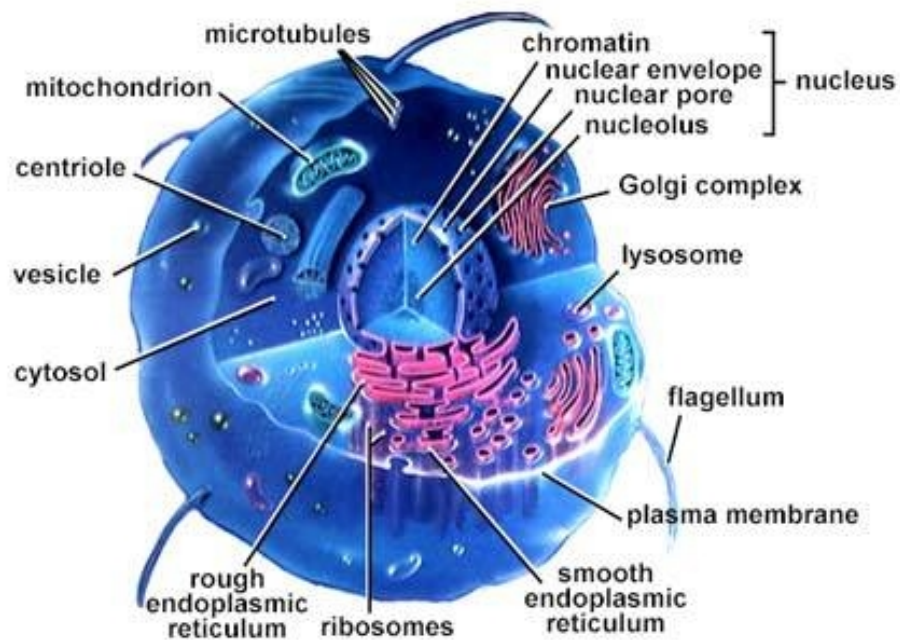


Figure 1.1.: Cell structure and components. The cell is a complex system composed of a nucleus, organelles and an outer shell, the cell membrane to name only a few components. The nucleus contains the genetic information in form of DNA and in the cytosol there are many more important components like the mitochondrion and the endoplasmic reticulum as shown in the figure. [6]

Singer and Nicholson in 1972 [8]. This model supports the free diffusion of proteins within the fluid 2D matrix, whereas Marguet et al. [9] showed that the interaction of lipids and proteins with the cytoskeleton can limit their free diffusion within the membrane. Moreover, liquid domains enriched in sphingolipids and cholesterol within the membrane may also influence diffusion and functionality of lipids and proteins [10]. These functional domains are called rafts and are thought to be important for cell signaling and trafficking. Rafts are supposed to be highly dynamic platforms in the range of nanometers, whereas direct visualization of lipid rafts in live cells is still missing [11, 12]. More generally, the dimension of spatial organization in cell membranes cannot be only in the range of a few nanometers but also on the order of 50–100 nm, characterizing interaction sites for membrane fusion such as exo- and endocytosis [13].

1.1. Cell membrane and lipid rafts

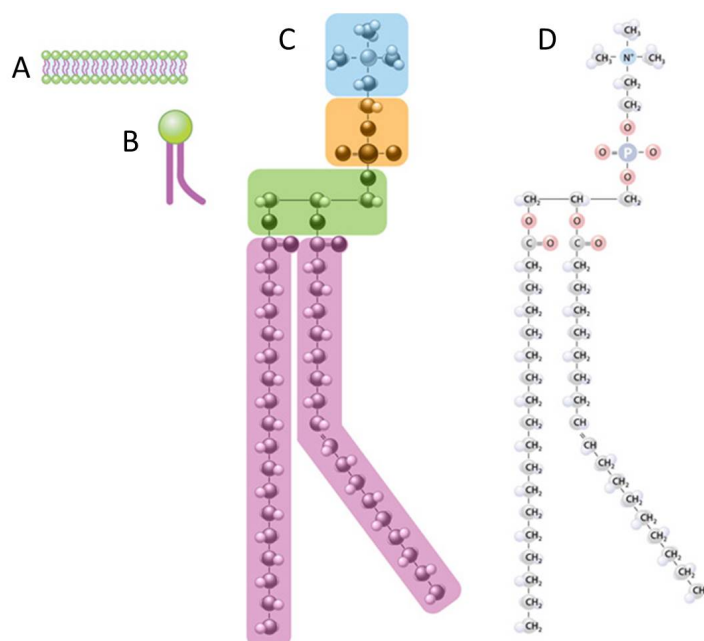


Figure 1.2.: Schematic representation of a lipid bilayer and the chemical structure of a glycerophospholipid molecule. Panel (A) shows a model of a cell membrane composed of glycerophospholipids. A lipid molecule is divided into a hydrophilic headgroup (green) and hydrophobic tails (purple) (B). The lipid headgroup region is further classified into a choline (blue), a phosphate (orange) and a glycerol (green) group (C). Panel (D) exhibits a fully atomistic representation of the lipid molecule. [7]

At an immune synapse the membrane exhibits even larger micron size scale clusters of proteins and lipids [14].

Cold detergent extraction [16] and mechanical disruption [17] of membranes are two techniques to look for raft associated lipids and proteins. These techniques can also induce artifacts and therefore they are not appropriate methods for measuring membrane organization of live cells [18]. Also fluorescence microscopy techniques were not able to visualize rafts or raft associated proteins such as GPI-anchored proteins in domains, but a homogeneous distribution of these proteins in the cell membrane could be observed [19]. Nevertheless, the development of better fluorescence microscopy and spectroscopy techniques has brought forth some new experiments with indications for the existence of dynamic raft-based

1. Introduction

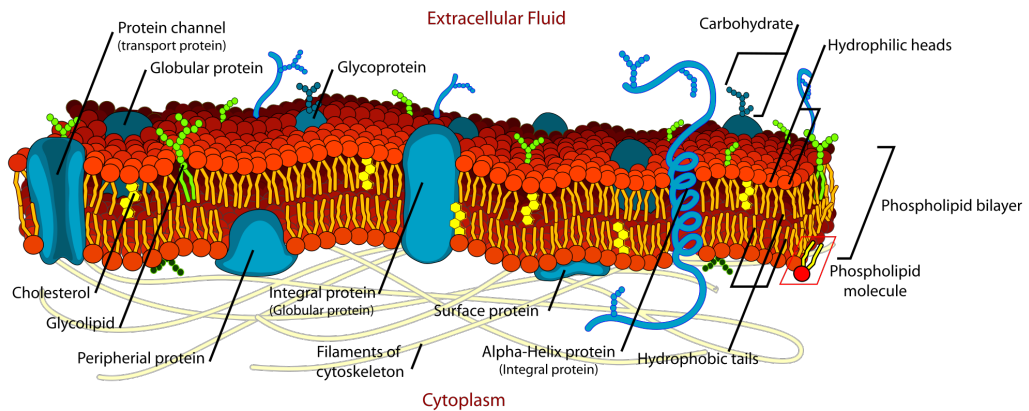


Figure 1.3.: Fluid mosaic model of a cell membrane by Singer and Nicholson. The membrane is shown as a two-dimensional liquid, consisting of phospholipid molecules (red) with embedded proteins (blue) that are free to move. Different types of proteins are mentioned, such as protein channels, integral and surface proteins. The intracellular cytoskeleton is shown as yellow filaments and supports the mechanical stability of the cell shape and prevents deformation. [15]

membrane heterogeneities [20–30]. Hancock et al. [20] suggested that there is a heterogeneity in nanoscale assemblies, which are smaller than the optical resolution limit. Electron microscopy and near-field scanning optical microscopy experiments supported these nanoscale heterogeneities [21–23]. Furthermore fluorescence correlation spectroscopy and high resolution fluorescence resonance energy transfer (FRET) experiments determined a size of < 120 nm and ~ 10 nm for the nano assemblies with a fluctuation time below a second [25, 31]. These fluctuating heterogeneities in live cells could be also observed by electron spin resonance experiments of spin labeled lipids in plasma membranes [29].

All these experiments that were done with different cell types could not show these raft like nano domains directly, but suggest the existence of small and highly dynamic heterogeneities in cell membranes. On the other hand there are a couple of studies indicating that the plasma membrane organization can be explained by other models than the raft hypothesis. Studies about domain formation of GPI anchored proteins in plasma membranes showed a stronger dependence on the cortical actin filament than on cholesterol concentration [31–35]. Recently Frisz et al. [35, 36] have

1.2. Lipid bilayer models

mapped sphingolipid rich domains in the plasma membrane of intact fibroblast cells by secondary ion mass spectrometry, whereas isotope-labeled cholesterol was evenly distributed throughout the membrane. Mueller et al. [37] support this hypothesis by single molecule experiments with model membranes where they found out that sphingolipid clustering is not only caused by cholesterol lipid interactions but also by interactions with the actin cytoskeleton. Finally, also a couple of studies suggest that the plasma membrane itself plays an active role in the lateral membrane organization and is more important than the sphingolipid cholesterol interaction [33, 38–42]. The raft hypothesis is still the most accepted model for domain formation in plasmamembranes, whereas there are now several alternative hypothesis, which has been mentioned in the previous lines, such as the clustering by interaction of proteins with cortical actin (Fig. 1.4).

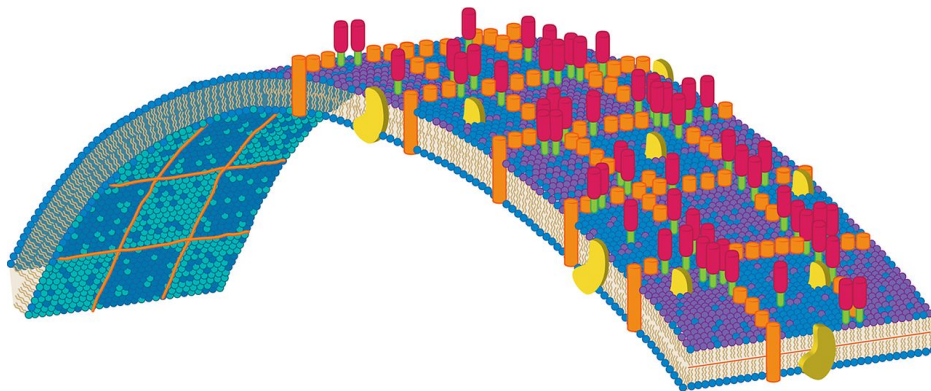


Figure 1.4.: Hypothetical model for plasma membrane compartmentalization. Transmembrane proteins (orange) interact with underlying cytoskeleton and limit the free diffusion of GPI-anchored proteins (red), transmembrane (yellow) proteins and lipids. In this hypothetical model, the underlying cytoskeleton arrange proteins and other components that results in the formation of lateral domains. [43]

1.2. Lipid bilayer models

Despite the complex structure of cell membranes containing many different lipid species and proteins with an asymmetric lipid distribution in the

1. Introduction

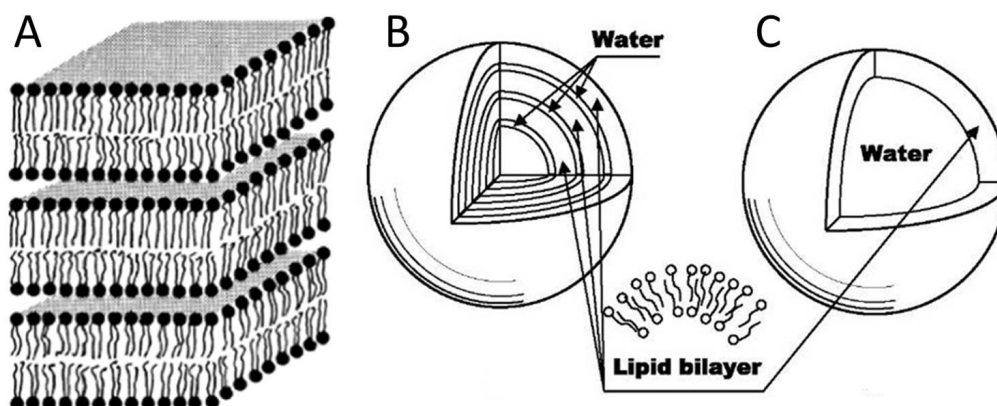


Figure 1.5.: Schematic illustration of supported bilayers and liposomes. (A) Stacks of supported flat lipid bilayers that are separated by a water layer. (B) Onion like structure of bilayer stacks in a multilamellar vesicle that are separated by water layers. (C) Circular shaped unilamellar vesicle with one single bilayer and a watercore. [44]

inner and outer leaflet as well as a cytoskeleton, which is important for the cell's shape and cell division, the membrane can be modeled as lipid only systems [45]. These model membranes consist of one or more different lipid species and can be prepared as flat bilayer stacks on a support (ranging from one up to several thousands of bilayers (Fig. 1.5 A) [46] or as a round shaped vesicles with one (unilamellar vesicles [ULVs], Fig. 1.5 C) or more bilayers (multilamellar vesicles [MLVs], Fig. 1.5 B), which are separated by water layers. The diameter of the vesicles can range from a few nanometers up to micrometers [4]. Depending on the temperature these fully hydrated lipid only systems show different lamellar phases ranging from liquid crystalline to gel phases such as L_{α} , P_{β}' , L_{β}' , L_{β} and L_c (Fig. 1.6 I). Further information about these lamellar phases and other structures that can be formed by these lipid/water dispersions, like hexagonal phases or cubic phases can be found in [47–50].

1.2.1. The effect of cholesterol on lipid bilayers

The simplest model system is a pure lipid/water dispersion with one lipid species only. It is getting more and more complex by adding other lipids

1.2. Lipid bilayer models

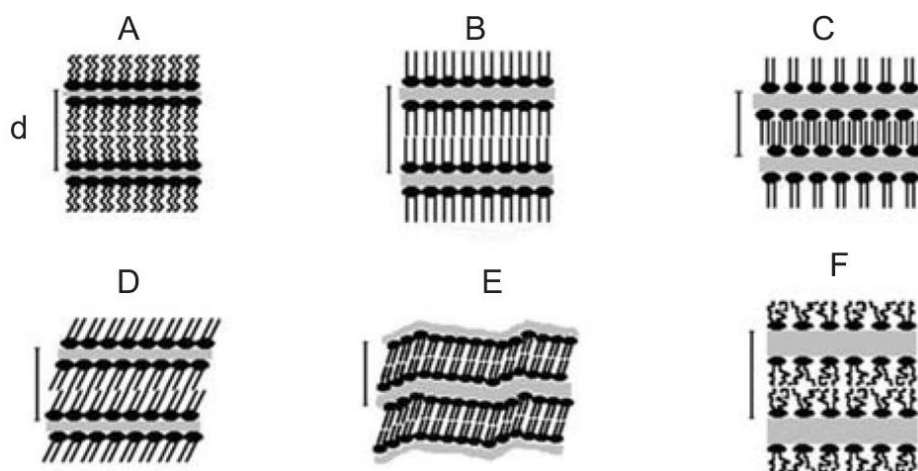


Figure 1.6.: Schematic representation of structures of lamellar lipid phases. (A) L_c (subgel), (B) L_β (gel), (C) L_β^{int} (interdigitated gel) (D) $L_{\beta'}$ (gel, tilted chains), (E) $P_{\beta'}$ (rippled gel), (F) L_α (liquid crystalline). [48]

and cholesterol that can strongly interact with lipids depending on saturation/unsaturation, chain length, headgroup and backbone structure [51]. It has been shown experimentally as well as by MD (molecular dynamic) simulations that the lipid cholesterol interactions are much higher for saturated lipids than for unsaturated ones [51, 52]. These interactions lead to the well known condensing effect on lipid bilayers [53–55]. Cholesterol increases the order of the hydrocarbon chains in the fluid bilayer and their rigidity that is associated with a thickening of the bilayer and a decrease in the area per lipid. Both effects have been studied and approved by many researchers in the past years and they found out that the bilayer thickness increase is not proportional to the cholesterol concentration but shows a nonlinear correlation [56–67].

There are also several models, which try to explain the interaction between lipids and cholesterol, such as the superlattice model [68], the condensed complex model [69, 70] and the most common one, the umbrella model [71, 72]. In the umbrella model the phospholipid headgroups are supposed to cover the hydrophobic cholesterol molecule to avoid exposure to water, which can be achieved by ordering the lipid chains to make space in the hydrocarbon region for cholesterol. This ordering affects also the mechani-

1. Introduction

cal properties of the bilayer and hence increases the bilayer's mechanical strength to reduce water permeability and decreases membrane fluidity [51]. As sphingomyelin (SM) and phosphatidylcholine (PC) are the major lipid species in the outer leaflet of the cell membrane, the interactions of them with cholesterol are of high interest, also with regard to the raft hypothesis [73]. The main difference between SM and PC is in the backbone region that has an influence in the interaction with cholesterol. SM has hydroxyl and amide groups, which act as hydrogen bonding donors, whereas the carbonyl and glycerol groups in PC act as acceptors, when they interact with cholesterol via hydrogen bonds (H-bonds) [51]. Rog et al. showed that the number of H-bonds of SM/cholesterol mixtures is higher than for PC/cholesterol mixtures. Together with the fact that the SM headgroup is more flexible and the level of unsaturation is lower than for PCs, the interaction of cholesterol with SM is stronger than with PC [51].

1.2.2. Binary lipid mixtures

The interaction of cholesterol and lipids can induce phase separation in the bilayer into coexisting liquid ordered (L_o) and solid ordered (L'_β) gel phases at temperatures below the melting temperature of the lipid hydrocarbon chains (see Fig. 1.7 B). This phase coexistence has been approved by many researchers, whereas direct evidence for the coexistence of fluid–fluid liquid ordered and liquid disordered (L_d or L_α) domains in binary mixtures is rare [74]. The L_o phase is still a liquid phase containing cholesterol that increases the hydrocarbon chain order as it is shown in Fig. 1.7 B. Nevertheless, the liquid–liquid phase coexistence that is the most likely model for domain coexistence in plasma membranes, has been visualized indirectly by EPR measurements of mixtures with single lipids and cholesterol (CHOL). Two component EPR and ^2H -NMR spectra have been observed for binary mixtures containing either DPPC (1,2-dipalmitoyl-*sn*-glycero-3-phosphocholine) or N-palmitoyl SM (N-palmitoyl-D-*erythro*-sphingosylphosphorylcholine) at temperatures above the chain melting temperature as evidence for coexisting liquid–liquid domains [75–77]. Binary phospholipid mixtures containing a high and a low melting lipid

1.2. Lipid bilayer models

can also show phase separation into gel and fluid domains (Fig. 1.7 A), whereas L_o/L_d phase coexistence could not be observed [78, 79]. Compared to L_o/L_d phase separation these gel and fluid domains are easy to access with experimental techniques such as fluorescence spectroscopy and FRET [79]. Because of that and the supposition that gel domains may play a role in cell membranes, they have attracted more attention again in the past years [78–80].

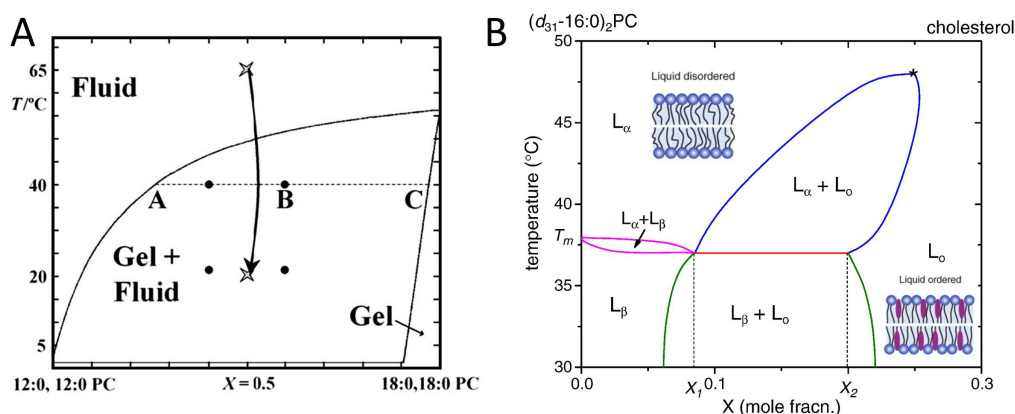


Figure 1.7.: Generic phase diagrams for two component lipid mixtures with and without cholesterol. (A) Binary phase diagram for a high and a low chain melting lipid mixture of 12:0,12:0/18:0,18:0 PC vesicles, where the abscissa represents the mole fraction of both lipids. Depending on lipid composition and temperature the bilayer can be in a fluid, gel or a coexisting gel/fluid phase. The horizontal dashed line \overline{AC} is the tieline at 40 °C. (B) Binary phase diagram of a high melting lipid (16:0,16:0 PC) and cholesterol. Depending on lipid composition and temperature the bilayer exhibits either homogeneous single phases or coexisting phases that are indicated by colored lines terminating phase coexistence regions in the phase diagram. [74, 79]

The phase behavior of these binary lipid mixtures can be described by a binary phase diagram and they can also be extended to tertiary or quaternary phase diagrams containing three or four different lipid species. Two binary phase diagrams for lipid bilayers containing either a high and a low melting lipid or one lipid species and cholesterol are shown in Fig. 1.7 and have been briefly discussed in the previous paragraph. Depending on the temperature and the ratio of the two lipid species the bilayer can be either in a gel phase, a fluid phase or can show gel/fluid phase coexistence (1.7A) [79]. By crossing a phase boundary that separates two

1. Introduction

different stable phases in the phase diagram, the bilayer undergoes a phase transition like it is indicated with the arrow in Fig. 1.7 A. Another important line is the tieline (dashed line), which is a horizontal line connecting any point in the two phase region with the phase boundaries on both sides. These intersections describe the lipid composition of the coexisting phases in equilibrium respectively.

The phase diagram in Fig. 1.7 B shows a more complex phase behavior, which is due to cholesterol. Depending on temperature and cholesterol concentration the bilayer exhibits a pure L_β (gel), L_d (liquid disordered) and L_o (liquid ordered) phase as well as three coexisting phases L_d/L_β , L_β/L_o and L_d/L_o . In addition to phase boundaries separating stable phases in binary mixtures with cholesterol there is a three phase line at a temperature close to the chain melting temperature of the lipid (orange line in Fig. 1.7 B). Compositions along this orange line at a constant temperature may show three coexisting phases ($L_d/L_\beta/L_o$). The asterisk at the top of the L_d/L_o two phase region in Fig. 1.7 B determines the critical point, where the coexisting phases show identical lipid compositions. There the system reveals also some interesting phenomena such as spinodal decomposition [81] or critical coalescence [82] due to large compositional fluctuations [83]. A detailed description and comparison of numerous binary phase diagrams containing different lipid species and cholesterol can be found in [74], where the difficulties of phase boundary determination and their uncertainties are also discussed.

1.2.3. Ternary lipid mixtures

To get a more realistic model for the lipid composition in the plasma membrane you can add another lipid species resulting in a three component mixture. These mixtures usually consist of a high melting lipid, a low melting lipid as well as cholesterol and show a complex phase behavior depending on composition and temperature similar to binary mixtures. The investigation of these phase behaviors helps understanding the phase behavior of plasma membranes. Figure 1.8 shows an illustrative ternary phase diagram composed of a low and a high melting lipid and cholesterol, where the regions for single phases as well as coexisting phases at a

1.2. Lipid bilayer models

certain temperature are described. The main feature of the ternary system is the formation of large coexisting liquid domains (L_o/L_d) that are stable at different temperatures and over a wide range of lipid compositions [83, 84]. These coexisting liquid phases, are used as lipid raft mimics.

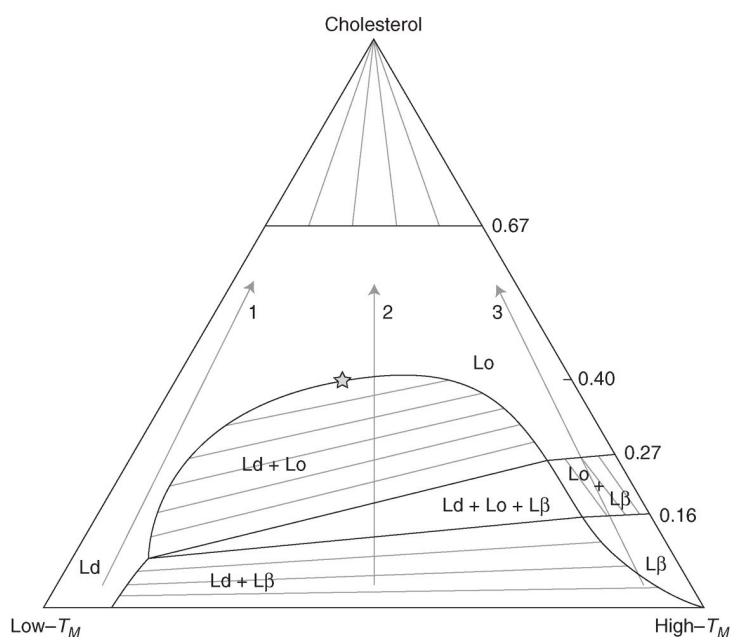


Figure 1.8.: Ternary phase diagram of a low, a high melting temperature lipid and cholesterol. Depending on the composition the diagram depicts homogeneous single phase regions and phase coexistence regions of two or three phases. Tielines within the phase coexistence regions are represented as straight lines and the star on top of the L_d/L_o region indicates the critical point. [13]

The ternary phase diagram is represented as a so called Gibbs triangle where the axes describe the mole fraction of the two lipid species and cholesterol. The exact composition of a sample is defined by the triangular coordinates (see Fig. 1.8) [85]. The straight lines within the two phase regions are called tielines and their inclination and the intersection with the phase boundaries define the lipid composition of the coexisting phases within this region. The star on top of the L_d/L_o region defines the critical point similarly to the critical point in the binary phase diagram. Over the years ternary phase diagrams for several different lipid mixtures has been published with the aim to find a better model system that mimics

1. Introduction

the plasma membrane and their liquid domains best. Almeida et al. [86] reported the first ternary phase diagram containing sphingomyelin as the high melting lipid that is a major component in natural plasma membranes and especially in rafts that consist mainly of sphingolipids. They could not observe liquid–liquid phase coexistence directly, but the phase boundaries were determined indirectly by spectroscopy experiments of fluorescently labeled lipid probes. Two years later Veatch et al. [87] published two more phase diagrams for PSM/POPC/CHOL and PSM/DOPC/CHOL at different temperatures based on fluorescence microscopy experiments of GUVs (giant unilamellar vesicles) where they could directly observe coexisting liquid domains. Although Almeida et al. and Veatch et al. reported phase diagrams for the same lipid mixture (PSM/POPC/CHOL) the phase boundaries do not match and hence shows the difficulties in determining correct phase boundaries. The different experimental techniques that were used to determine phase boundaries could be the reason for these big discrepancies. Pokorny et al. [88] published another phase diagram containing pBSM/POPC/CHOL showing again different boundaries. Whereas all reported phase diagrams containing sphingomyelin show the same common phase coexisting regions of L_o/L_d , L_d/L_β and L_o/L_β as well as three phase triangular region of $L_o/L_d/L_\beta$, whereby the existence of three coexisting phases has not been demonstrated directly [85].

There are also a number of ternary phase diagrams consisting of cholesterol and phosphatidylcholine (PC) lipids only. Fully saturated phospholipids with a high chain melting temperature can be used as a surrogate for SM and such mixtures exhibit also similar phase behavior like SM mixtures with all the same phase coexistence regions [77, 89, 89–96]. Depending on the lipid species that is used as the high and the low melting lipid, the size of the domains in the coexisting L_d/L_o region, the position of the phase boundaries as well as the transition temperature to a homogeneous phase is different [84, 87]. These PC containing three component mixtures show in general micron scale liquid domains within their L_d/L_o region that make them accessible for many different experimental techniques and especially for fluorescence microscopy techniques with which the coexistence of domains can be shown directly. Some mixtures do not show any micron scale fluid domains such as POPC/DPPC/CHOL and

1.2. Lipid bilayer models

DLPC/DPPC/CHOL [84, 94], but although such small nanodomains are difficult to access with experimental techniques these systems can also be a model for lipid rafts, which are supposed to be also small and highly dynamic. A compendium of ternary phase diagrams and more detailed information can be found in [83, 85].

1.2.4. Phase behavior of multicomponent lipid membranes

Multicomponent Mixtures, such as binary, ternary and even more complex mixtures exhibit different phases depending on composition and temperature as it was discussed in the previous paragraph. The phases are divided into homogeneous phases, where the bilayer exhibits only one homogeneous phase (L_d , L_o , L_β), and inhomogeneous phases, which show heterogeneities in the lateral area of the bilayer, like the coexistence of two or three phases (L_d/L_o , L_d/L_β , L_o/L_β , $L_d/L_o/L_\beta$) (see Fig.1.8) [13]. Homogeneous phases like the L_d and L_β phase consist mainly of one lipid species with a small amount of cholesterol, whereby the low melting lipid is the main component in the L_d phase and L_β contains mainly the high melting lipid. The lipid composition in the L_o phase is similar to L_β but with a higher cholesterol concentration that decreases the tilt angle of the hydrocarbon chains in the gel phase and leads to a "softening" of the bilayer (L_o) [97]. At cholesterol concentration between $\sim 15\text{--}30\%$ in the L_β phase, CHOL reaches its maximum solubility and phase separate into L_β and L_o phase (see arrow 3 in Fig. 1.8). At compositions of low and high melting lipids without cholesterol the distribution is heterogeneous and the membrane phase separates into L_d/L_β . By increasing the CHOL concentration firstly a small three phase regime of $L_d/L_o/L_\beta$ can be observed and then the large L_d/L_o regime appears (see arrow 2 in Fig. 1.8) [13]. As long as the lipid compositions in the phase diagram are far away from the critical point, all these pure as well as coexisting phases are stable regarding domain size, lifetime and morphology at a constant temperature that is between the hydrocarbon melting temperature of the low and the high melting lipid.

1. Introduction

1.2.5. On domain size, critical fluctuations and microemulsion of complex lipid mixtures

The coexisting domains in the two and three phase regions can be classified as TypeI and TypeII mixtures regarding their domain size [98]. Depending mainly on the low melting lipid type the domains in the L_d/L_o region can be macroscopic ranging from $\sim 1-10 \mu\text{m}$ (TypeII) or nanoscopic with a diameter of $\sim 2-10 \text{ nm}$ (TypeI). TypeII phase diagrams have been firmly established with different experimental techniques, because of the large domains that can be visualized by many microscopical techniques. Although TypeI mixtures exhibit very small domains with a phase coexistence region that appears uniform under the microscope, various experiments (FRET, ESR), which are sensitive to the nanometer regime, confirmed the coexistence of L_d/L_o domains indirectly [96]. Macroscopic domains appear mainly as circular clusters embedded in an environment of the other phase that can be either a L_o domain in a L_d matrix or vice versa, depending on the composition. This large and stable circular domains can be theoretically explained by line tension which is thought to be the main driving force [13]. However, Keller and coworkers showed recently that the stability and shape is highly influenced by the lipid composition and not only by the height mismatch between L_o and L_d domains that drives line tension [99]. While L_o domains consist mainly of saturated chains and cholesterol, which form a highly ordered and hence thicker bilayer, the main components in L_d domains are unsaturated or even di-unsaturated lipids with a small amount of cholesterol. Hence the L_d phase shows higher disorder and a thinner bilayer [100]. But recently Bleecker et al. [101] have discovered a special composition that show coexisting phases with thick L_d domains and thinner L_o domains.

Another feature of macroscopic domains is their columnar alignment in MLVs or supported bilayer stacks on a substrate [102]. Figure 1.9 shows a schematic picture of the stacking of L_o domains (green) and the L_d surrounding (red). Domain stacking is a crucial property for small angle x-rays scattering (SAXS) analysis of MLVs with coexisting L_o/L_d domains and will be discussed in chapter 2. Tayebi et al. [103] observed that the domains can form a columnar alignment across 150 to 1200 bilayers that leads to a thickness of several micrometers of supported bilayers.

1.2. Lipid bilayer models

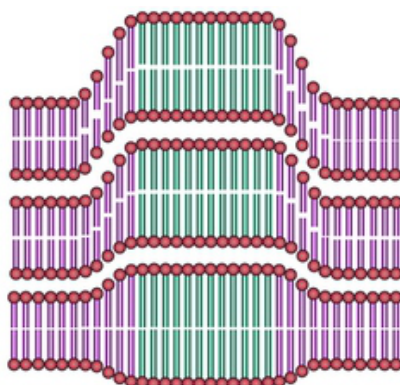


Figure 1.9.: Schematic representation of lipid domain alignment. In multicomponent lipid mixtures the membrane can form coexisting liquid domains (indicated in green and red) that show alignment across many lipid bilayers. [102]

Although the mechanism and forces that drive this alignment are still unknown, Tayebi and coworkers further showed that the domain size increases as a function of bilayer stacks. Also little is known about the domain boundaries between the L_d and L_o domains that might play an important role in the lateral coupling of domains as well as in the domain stacking where the bilayer bending should not favor this energetically unfavorable arrangement [104].

Macroscopic domains in TypeII mixtures have been studied extensively in the past years regarding their physical and chemical properties, as it was mentioned before. However TypeI mixtures, exhibiting nanoscopic domains, are challenging to study, they are of great interest because of their importance in biological membranes [10]. Although experiments have shown the thermodynamic stability of these small nanodomains [1, 85, 96, 98, 105], the mechanism that stabilizes nanoscopic domains is still unknown. Considering line tension only in the domain interactions, this would result in coalescence of domains and therefore lead to an unlimited domain growth [96, 98]. But this has not been observed and therefore it is more likely that short range attractive interactions are competing with long range repulsive interactions, which counteract each other in the equilibrium state resulting in stable nanoscopic domains [106]. Repulsive interactions can be either electrostatic or due to the

1. Introduction

highly curved domain boundaries, which can form a barrier to domain coalescence [107, 108]. For uncharged bilayers that are studied in this work, such repulsive forces have not been observed. Therefore a reason for stable nanodomains could be an equilibrium state between low line tension and entropy, which favors small domains to have more ways to form a phase [109]. Frolov et al. [109] also suggested that there could be a critical line tension at which nanodomains coalesce to macroscopic phases. Nevertheless the exact mechanism for the stability of nanoscopic domains and their coalescence to larger macroscopic domains is still unknown.

Nanoscope domains can be also explained by alternative interpretations, like that these domains are critical fluctuations, which can emerge at compositions and temperatures even far away from the critical point [30, 110, 111], or that nanodomains are a microemulsion, which is a fluid phase containing fluctuating structures of a characteristic size and length [112–116]. Critical fluctuations are small clusters that change in composition and size over time and are not stable. The line tension is rather small for this fluctuating structures and therefore clusters can appear and disappear dynamically [111]. The emergence of microemulsions can be attributed to several mechanisms. One mechanism is that so called line active agents, like hybrid lipids with one saturated and one unsaturated hydrocarbon chain, are located at the interface between separated regions within the bilayer and reduce the energy to avoid real domain formation [114, 117]. Another explanation for microemulsions are fluctuations in curvature that lead to separation of lipids into regions of positive and negative curvature by decreasing the energy per unit area in this regions [118, 119]. Schick [112] pointed out that the coupling of height fluctuations and lipid composition could be the main reason for microemulsions in plasma membranes. As phosphatidylethanolamine (PE) and phosphatidylserine (PS) have very different spontaneous curvatures and are major components in plasma membranes, they seem to couple to membrane height fluctuations and therefore lead to microemulsions in plasma membranes [115].

The previous paragraph described critical fluctuations at compositions and temperatures far away from the critical point, but mainly these fluctuations occur close to the critical point, where the compositions of coexisting domains are identical, as it can be seen in Fig. 1.8, and the "osmotic compressibility" diverges [30]. This divergence reduces the energy at the

1.2. Lipid bilayer models

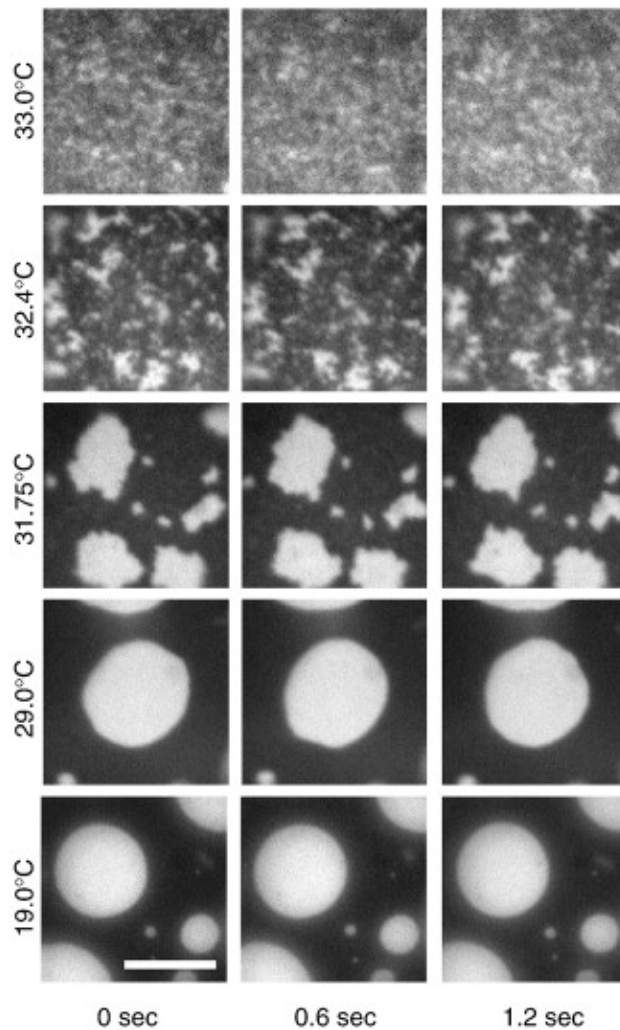


Figure 1.10.: Domain formation in giant unilamellar vesicles (GUVs) across the critical temperature T_C . Fluorescence microscopy pictures of GUVs composed of diphatynoyl-PC/DPPC/CHOL 25:20:55 mol% and 0.8 mol% of Texas Red DPPE through time at a series of temperatures is shown, with a scale bar of $20\ \mu\text{m}$. Above $T_C \sim 31.9^\circ\text{C}$ the membrane shows compositional fluctuations, whereby it remains homogeneous on average. Below T_C stable domains are formed and due to the increase in line tension domain edges become smooth and circular shaped. [111]

interface between adjacent phases and the thermal energy leads to deformation of domain boundaries, as it is shown in Fig. 1.10, where domains

1. Introduction

are deformed close to the critical temperature ($T_c = 31.9^\circ\text{C}$). Above T_c compositional fluctuations can be observed as they appear and disappear [30, 111, 120]. In this case T_c is also a mixing temperature, meaning that below T_c the bilayer is phase separated into L_o/L_d domains and above T_c only one homogeneous phase is present. As critical behavior is an universal property for diverse experimental systems it can be described by a common model, the 2D Ising model, that takes into account nearest neighbor interactions. It has been used to describe critical behavior of liquid crystals [121], spin magnets [122], multicomponent mixtures [82] as well as lipid mixtures containing cholesterol [30, 90, 123]. Most experiments confirmed a 2D Ising model behavior for multicomponent lipid mixtures, especially fluorescence microscopy measurements [30, 123, 124], but recent atomic force measurements (AFM) on L_o/L_d height mismatch [125] and first momenta of NMR spectra [126] favored the 3D Ising model. This issue whether multicomponent lipid mixtures behave like a 2D or a 3D Ising model will be also addressed in this work.

1.2.6. L_o/L_d domain size as a function of lipid composition

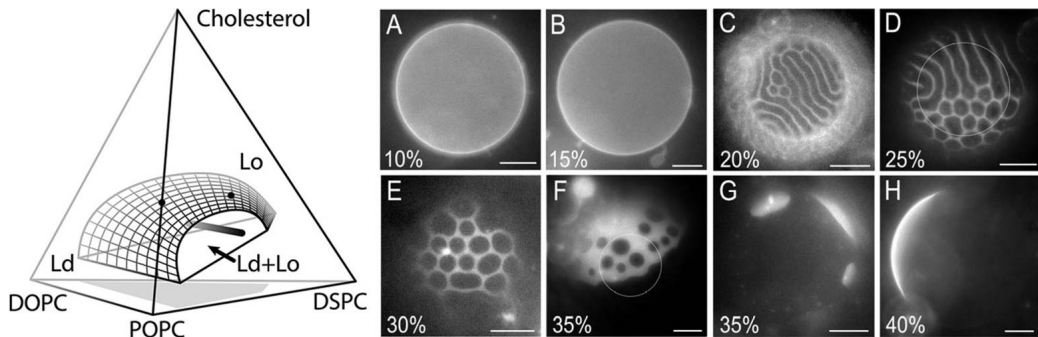


Figure 1.11.: Phase behavior of liquid domains in complex lipid mixtures. The left panel shows a four component phase diagram composed of POPC/DOPC/DSPC/CHOL with the L_o/L_d phase coexistence region indicated as grey shaded area. The right panel exhibits fluorescence microscopy pictures of GUV morphologies composed of (POPC+DOPC)/DSPC/CHOL 0.30/0.45/0.25 mol% along a ρ_{DOPC} trajectory (see Eq. 1.1). At low ρ_{DOPC} values GUVs appeared uniform, because of the non-visible nanoscopic domains. Between $\rho_{DOPC} = 20\%$ and 30% modulated phases can be observed and after the modulated phase window the GUVs exhibit macroscopic round domains. [127]

1.2. Lipid bilayer models

The four component lipid mixture DOPC/POPC/DSPC/CHOL can be used to tune domain size of coexisting liquid domains (L_o/L_d). POPC/DSPC/CHOL mixtures exhibit nanoscopic domains, whereas lipid mixtures of DOPC/DSPC/CHOL show macroscopic phase separation. Feigenson and coworkers [1, 105, 127] implemented this four component mixture of DOPC/POPC/DSPC/CHOL that exhibits a transition of liquid domains from nanoscopic to macroscopic in the L_o/L_d region as POPC is replaced by DOPC. The POPC/DOPC exchange is defined by the replacement ratio ρ_{DOPC} :

$$\rho_{DOPC} = \frac{\chi_{DOPC}}{\chi_{DOPC} + \chi_{POPC}} [\%] \quad (1.1)$$

where χ_{DOPC} and χ_{POPC} describe mole fractions of DOPC and POPC respectively [127]. Figure 1.11 (left panel) shows a quaternary phase diagram of POPC/DOPC/DSPC/CHOL, where the shaded area describes the L_o/L_d phase coexistence region. Fluorescence microscopy pictures of GUVs with fixed concentrations of (DOPC+POPC)/DSPC/CHOL (0.30/0.45/0.25 mol%) with increasing ρ_{DOPC} from 10 % to 40 % are shown at the right panel. By traveling in composition space along a certain ρ_{DOPC} trajectory starting from a pure POPC/DSPC/CHOL composition, the GUVs exhibit different phases. At low ρ_{DOPC} values (10 %, 15 %) GUVs reveal nanodomains that appear uniform under the fluorescence microscope (Fig. 1.11). Between $\rho_{DOPC} = 20\%$ and 30% the GUVs display modulated phases, such as stripe like or honeycomb patterns. This range is also called the modulated phase window and after that window ($\rho_{DOPC} > 30\%$) the elongated patterns start to coarsen and form round macroscopic L_d domains within a L_o surrounding.

The range and the exact values for ρ_{DOPC} of this modulated phase window are dependent on cholesterol concentration but also on the temperature [127]. Increasing CHOL concentration shifts the window to higher ρ_{DOPC} values and also the compositions of the coexisting phases converge. Goh and coworkers [127] further observed that the appearance and disappearance of modulated phases as well as their morphology is influenced by the amount of each phase area fraction of L_o or L_d . The existence of stable modulated phases can be explained by a combination of low line tension values and a significant difference in bending moduli between the two phases that was observed in Monte Carlo simulations [128].

1. Introduction

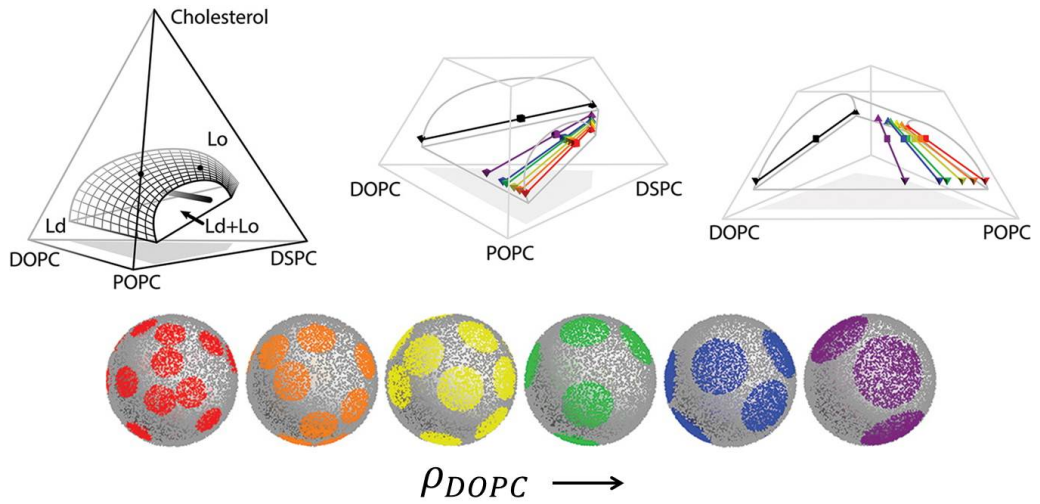


Figure 1.12.: DOPC/POPC exchange rate ρ_{DOPC} controls domain size. Upper panel shows different views of the four component phase diagram composed of POPC/DOPC/DSPC/CHOL. Tielines at different ρ_{DOPC} values ranging from $\rho_{DOPC} = 0\%$ (red line) up to 100% (black line) are shown within the L_0/L_d phase coexistence region. Tieline endpoints are labeled as pyramids and midpoints as cubes. The lower panel shows Monte Carlo simulations of ULVs exhibiting coexisting L_0 (grey surrounding) and L_d (colored round domains) phases according to tielines in the upper panel. [1]

To determine domain size of nano and macro domains quantitatively, Heberle and coworkers performed neutron scattering experiments on ULVs at lipid compositions along a ρ_{DOPC} trajectory in the L_0/L_d phase coexistence region [1]. The DOPC/POPC/DSPC/CHOL phase diagram with tielines along this trajectory as well as the corresponding simulated vesicles (Monte Carlo) with their circular L_d domains are represented in Fig. 1.12. The red color indicates the smallest domains at $\rho_{DOPC} = 0\%$ with a radius r of ~ 7 nm and purple represents the largest simulated domains at $\rho_{DOPC} = 35\%$ with $r = 16$ nm. The largest domains in general appear at $\rho_{DOPC} = 100\%$ with $r > 22$ nm. As you can see from the simulated vesicles not only the domain size changes but also the number of domains, which decreases as a function of ρ_{DOPC} . Heberle et al. obtained the domain size and number of domains by Monte Carlo fits of their simulated vesicles to the small angle neutron scattering (SANS) data. SANS experiments were performed on 60 nm diameter ULVs where the L_0 surrounding

1.2. Lipid bilayer models

was contrast matched with the liquid solution and so scattering from L_d domains only could be detected and analyzed. Although some of the samples have compositions within the modulated phase window ($15 < \rho_{DOPC} < 25\%$), the SANS data didn't reveal any modulated phase patterns but could be perfectly described by circular domains. Further on, the domains at $\rho_{DOPC} > 30\%$ didn't show complete coalescence to one or two domains as it was observed in GUVs [105, 127]. It is still unclear whether this is a result due to the limit in size of 60 nm vesicles compared to GUVs or due to differences in curvature between ULVs and GUVs [1].

Beside domain size of coexisting phases also bilayer thickness d_B of the corresponding tieline endpoint samples, exhibiting a pure L_o or L_d phase, were measured [1]. The bilayer thickness of the pure L_o phase stays constant as a function of ρ_{DOPC} whereas the L_d phase gets thinner as the POPC is exchanged by DOPC, resulting in a linear increase in height mismatch between the L_o and L_d endpoint samples. The height mismatch Δd_B between domains and the surrounding is directly related to the line tension γ between two phases ($\gamma \propto \Delta d_B^2$) [129]. So they showed that the increase in height mismatch, which is directly connected to an increase in line tension, could be a plausible driving force for domain coalescence [1].

1.2.7. Protein partitioning and function in L_o/L_d phases

Despite the unresolved question about the general existence of lipid rafts in cell membranes, transmembrane proteins appear to be associated either with the sphingolipid and cholesterol rich raft phase, such as GPI-anchored proteins [130, 131] or the less ordered surrounding containing unsaturated phospholipids [132]. There are mainly two features of a bilayer that may be crucial for protein sorting and activity in the plasma membrane. One feature is the difference in mechanical properties between different phases such as bending rigidity and area compressibility modulus [133–138]. Structural properties such as bilayer thickness or hydrocarbon core length in the bilayer are the second feature that can influence protein partitioning [133, 139–142].

1. Introduction

The difference in bilayer thickness between several phases are thought to have a large influence on protein sorting as different transmembrane proteins also have different sizes regarding their hydrophobic region. This structural feature is thought to play a major role in protein sorting and trafficking within the Golgi apparatus [143]. Bretscher and Munro [143] postulated that proteins with a longer hydrophobic transmembrane region partition into the sphingolipid and cholesterol enriched thicker raft phase, whereas proteins with shorter hydrophobic regions are localized in the thinner surroundings that is called hydrophobic matching. Supporting this concept numerous experiments on lipid only systems and peptides have shown that different lipid environments with various bilayer thickness influence peptide partitioning into the bilayer as well as the orientation and conformation of the peptide [100, 141, 142, 144]. McIntosh et al. [135] performed experiments using detergent soluble (DSM) and detergent resistant membranes (DRM) to measure the partitioning of peptides with a hydrophobic length that match the bilayer thickness of DSM and DRM. They found a significant enrichment of the longer peptide in the thicker DRM at physiological temperatures, whereas at 4 °C the peptides were equally distributed showing that peptide sorting depend on hydrophobic matching and temperature.

The different lipid compositions in raft and non-raft phases or L_o and L_d domains do not only influence the structure of the bilayer but also the mechanical properties, which is the second important feature in protein sorting. SM and cholesterol rich domains for example are more rigid than their surrounding of unsaturated PC lipids and also have larger compressibility moduli resulting in a higher energy cost to separate adjacent lipids [145]. Gandhavadi et al. [100] supported this theory by experiments showing that hydrophobic peptides favor the less ordered surrounding. Another important parameter for protein partitioning is the geometry of the protein. Grunner [146] and Cantor [147, 147] proposed a theory combining mechanical bilayer properties and protein geometry to calculate protein partitioning and function. The theory uses the pressure profile of a bilayer, which is related to elastic properties such as spontaneous curvature, bending rigidity, Gaussian modulus and the lateral area expansion of a bilayer as well as the lateral expansion of a protein along the bilayer normal to calculate the energy cost for proteins to partition

1.3. Experimental methods to examine lipid domains

into a certain phase [133]. Therefore it is crucial to accurately know the structural and mechanical properties of domains to gain more insight into the mechanism of protein sorting by lipid rafts.

1.3. Experimental methods to examine lipid domains

While a lot of work has been done on lipid rafts, there is still much left to learn about. One crucial parameter is domain size and the mechanism that governs it [1, 148], whereas in this thesis the focus will be more on structural and elastic parameters of coexisting liquid disordered and liquid ordered domains. Numerous theoretical and experimental techniques have been applied to examine the structural and mechanical properties of L_o/L_d phases in lipid only systems (see e.g. [100, 126, 129, 135, 137, 149–158]). A crucial thing to know is the lipid composition in the coexisting L_d and L_o phase, which is determined by the inclination of the tieline and the phase boundaries of the two phase region within the phase diagram. However the determination turned out to be a considerable challenge [91, 159], as it was briefly discussed in the previous section.

Historically, fluorescence microscopy was the first technique used to show phase coexistence in lipid model membranes [160] and is therefore still one of the main techniques for studying L_d/L_o phase separation. To determine domain size and in general coexistence, this is an appropriate and direct technique, but for the investigation of physical and structural properties of domains other techniques such as electron spin resonance, atomic force microscopy and small angle x-ray or neutron scattering are more suitable [152–156]. The different techniques have their advantages and disadvantages. Fluorescence microscopy for example is a direct method to visualize large domains and to determine their size, but this technique requires domains with a minimum diameter of 300–500 nm and additional fluorophores, that can induce artifacts [87, 89, 161, 162]. Further fluorescence techniques including quantum yield, lifetime, anisotropy, spin label quenching, Förster resonance energy transfer measurements as well as electron spin resonance spectroscopy experiments indeed can

1. Introduction

resolve very small domains at the order of a few nanometers in diameter [89, 94, 163–166]. Two more promising techniques to resolve small heterogeneities in lipid membranes are superresolution imaging and STED microscopy, where fluorescently labeled lipids are used to map transient sphingomyelin clusters at the size of 20 nm and a timescale of 15 msec [167]. These techniques require again extrinsic probes that can potentially perturb and affect domain formation, size and other parameters [76, 91, 96, 152, 168]. Recently Wallace and coworkers [169] have implemented a new label free technique called interferometric scattering microscopy (iSCAT) to observe nanoscopic domains.

During the last decades probe free scattering techniques such as small angle neutron and x-ray scattering (SANS and SAXS) have been used to determine mainly structural but also elastic properties of lipid model membranes [152–156]. An important structural parameter is the bilayer thickness d_B that is crucial for studying hydrophobic mismatch between proteins and the membrane and therefore d_B should be accurately determined. Gandhavadi et al. [100] determined bilayer thicknesses of detergent resistant membranes (DRMs) and detergent soluble membranes (DSMs) by SAXS and showed that DRMs are $\sim 9 \text{ \AA}$ thicker than DSMs. Chen and coworkers [156] also did SAXS experiments on MLVs consisting of DOPC/DPPC/CHOL showing phase separation into L_d/L_o phases. They determined bilayer thicknesses of the coexisting domains and calculated a difference between L_d and L_o of $\sim 6 \text{ \AA}$. In both studies a Fourier reconstruction of the relative electron density profile of the bilayer was used to calculate bilayer thicknesses [170, 171]. This method is suitable for oriented multilayer samples with more than four orders of Bragg reflections, but has its limits analyzing diffraction patterns of fully hydrated multilamellar vesicles especially when the membrane is in the liquid phase, where the diffraction pattern exhibit only three or even less Bragg peaks. Based on the global analysis program GAP of Pabst et al. [172] for fully hydrated MLVs and the SDP analysis of Kučerka et al. [173] we developed a novel high resolution analysis technique to obtain structural and elastic bilayer information regardless the number of Bragg reflections. This high resolution analysis technique further improved the precise determination of two important parameters, the bilayer thickness and lipid area of fully hydrated as well as label and stress free lipid bilayers. Moreover, this

1.3. Experimental methods to examine lipid domains

technique was improved further to analyze diffraction pattern of MLVs with coexisting L_o/L_d domains. Both methods are described in detail in chapter 2.

2. Methods

2.1. Scattering techniques

Scattering techniques are widely used methods to obtain quantitative information about size, shape and structure of colloidal particles, proteins, liposomes etc. The resolution depends on the incident wavelength, which is on the order of a few Angstrom ($\lambda = 0.5\text{--}2.3 \text{ \AA}$) for x-rays as well as for neutrons ($\lambda = 0.1\text{--}30 \text{ \AA}$). Therefore x-ray and neutron scattering are appropriate methods to examine structural properties of materials on a length scale of $\sim 0.1\text{--}100 \text{ nm}$ like lipid bilayers. In the case of biological samples such as liposomes or proteins the two dimension scattering profile is isotropic, because of the random orientation of the particles in solutions and can be reduced to a one dimensional scattering pattern. Moreover, x-rays and neutrons can scatter either elastically, where they collide with a particle without losing energy but changing the direction, or inelastically, meaning that the x-ray photon or the neutron lose energy within the interaction process with matter. In this work only elastic scattering of x-rays and neutrons is used and described in the next paragraphs.

2.1.1. Small angle x-ray scattering (SAXS)

X-rays are electromagnetic waves that can be produced either with a lab source x-ray generator or at a synchrotron by accelerating electrons, which emit photons of a certain wavelengths and energies, that can be described by De Broglie's equation:

$$E = \frac{hc}{\lambda} \quad (2.1)$$

2. Methods

where E describes the energy of the photon, h is the Planck constant, c is the speed of light and λ is the wavelength. At the synchrotron Elettra in Trieste, where all the measurements for this work were done, 8 keV photons were used.

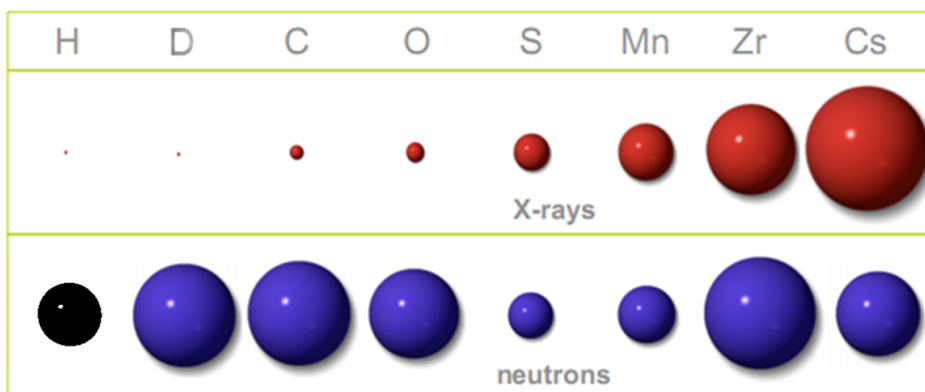


Figure 2.1.: X-ray and neutron scattering cross sections. The x-ray cross section increases with the size of atoms, whereas there is no correlation between size of atoms and neutron scattering cross section. While the x-ray scattering cross section for hydrogen (H) is the same as for deuterium (D), the neutron scattering cross section for D is positive like for the other presented atoms (blue circles), whereas H exhibits a negative one (black circle). This makes neutron scattering a powerful technique for contrast variations in biological samples by exchanging hydrogen with deuterium. [174]

Small angle x-ray scattering (SAXS) is sensitive to inhomogeneities in the electron density of a material because of the interaction with the outer shell electrons of atoms. Figure 2.1 shows a qualitative comparison of scattering cross sections between different atoms for x-rays in the upper panel. The cross section increases as a function of the size of atoms and hence electron density. Furthermore, a net electron density $\Delta\rho(\vec{r})$, which is defined as the electron density distribution of your sample $\rho(\vec{r})$ subtracted by the electron density of the surrounding or solvent ρ_s , can be determined:

$$\Delta\rho(\vec{r}) = \rho(\vec{r}) - \rho_s \quad (2.2)$$

The net electron density gives rise to the so called contrast of your sample that is usually low for biological samples containing a lot of light molecules, like hydrocarbons in the lipid chain, whereas for the electron rich headgroup of a lipid the contrast is much higher as it is shown in the upper right corner in Fig. 2.2.

2.1. Scattering techniques

Due to interactions between incident x-ray photons and matter the scattered intensity can be detected as a function of the scattering angle 2θ . The scattering vector q describes the momentum transfer as a function of the incident wavelength and the scattering angle:

$$q = \frac{4\pi \sin \theta}{\lambda}. \quad (2.3)$$

Another important feature in SAXS are Bragg reflections, which occur at angles (q -values) where Bragg's law is fulfilled:

$$n\lambda = 2d \sin \theta, \quad (2.4)$$

where n is the order of Bragg reflection and d is the lattice parameter. In the special case of MLVs or supported bilayer stacks d describes the lamellar repeat distance of bilayers. A schematic representation of a SAXS experiment on MLVs is shown in Fig. 2.2. The dispersion of MLVs and water are exposed to an x-ray beam and due to the equidistant structure of the bilayers within the MLVs, the Bragg condition is fulfilled resulting in Bragg reflections in the scattering pattern (equidistant Bragg peaks in scattering profile within Fig. 2.2).

2.1.2. Small angle neutron scattering (SANS)

Neutrons for small angle neutron scattering (SANS) are produced in neutron reactors or spallation sources and can be described similarly like x-rays regarding wavelength, energy and Bragg reflections. The main difference is the interaction with matter. While x-rays interact with the electron cloud, neutrons interact with the nucleus of an atom and therefore the cross section is completely different compared to x-rays. Figure 2.1 compares cross sections of atoms for x-rays and neutrons. While for x-rays the cross section increases with atomic mass, there is no obvious correlation between different atoms and their neutron scattering cross sections.

The contrast in neutron scattering can be defined by a net neutron scattering length density $\Delta\text{NSLD}(\vec{r})$, which is defined in a similar way as the net

2. Methods

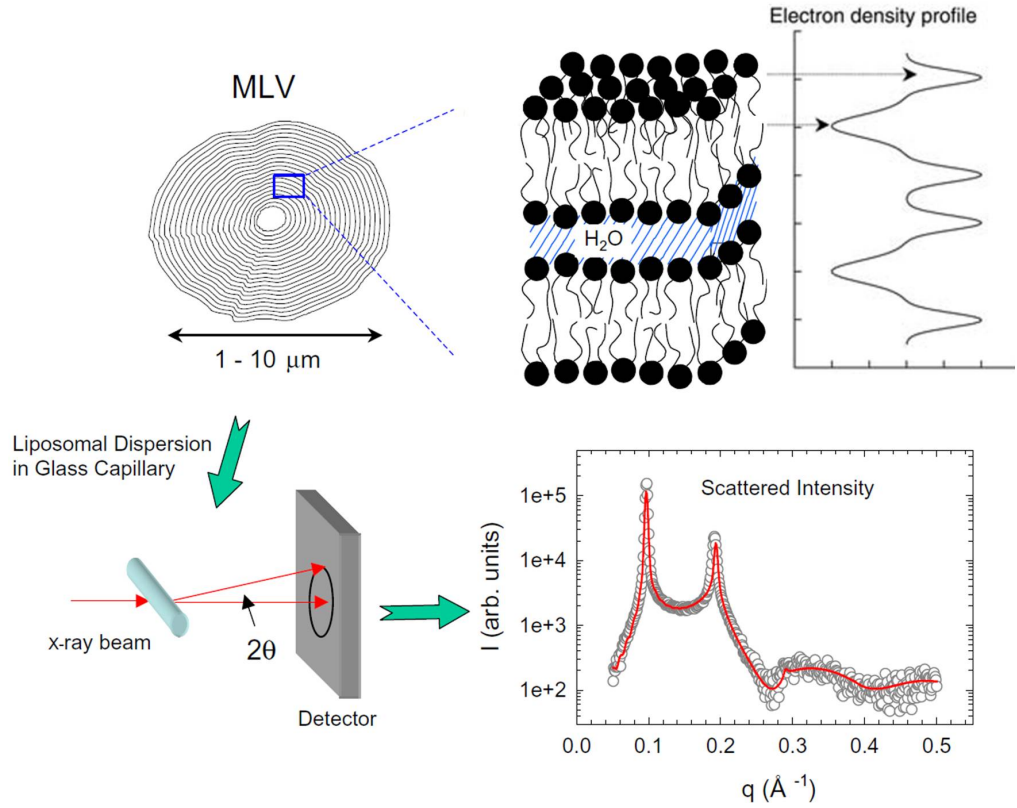


Figure 2.2.: Schematic representation of a SAXS experiment. A dispersion of MLVs with a diameter of $1-10 \mu\text{m}$ and H_2O is filled in glass capillaries and exposed to an x-ray beam. The scattered intensity is detected and analyzed by a full q -range model that reveals information about the electron density profile of a lipid bilayer. [175]

electron density for x-rays:

$$\Delta\text{NSLD}(\vec{r}) = \text{NSLD}(\vec{r}) - \text{NSLD}_s, \quad (2.5)$$

where $\text{NSLD}(\vec{r})$ is the neutron scattering length density distribution of the sample and NSLD_s is that of the solution. The NSLD for a molecule can be calculated as following:

$$\text{NSLD} = \frac{\sum_{i=1}^n b_i}{v_m}, \quad (2.6)$$

where b_i is the coherent scattering length of the i th atom in a molecule and v_m is the molecular volume. The big difference in NSLD between H_2O and

2.1. Scattering density profile model

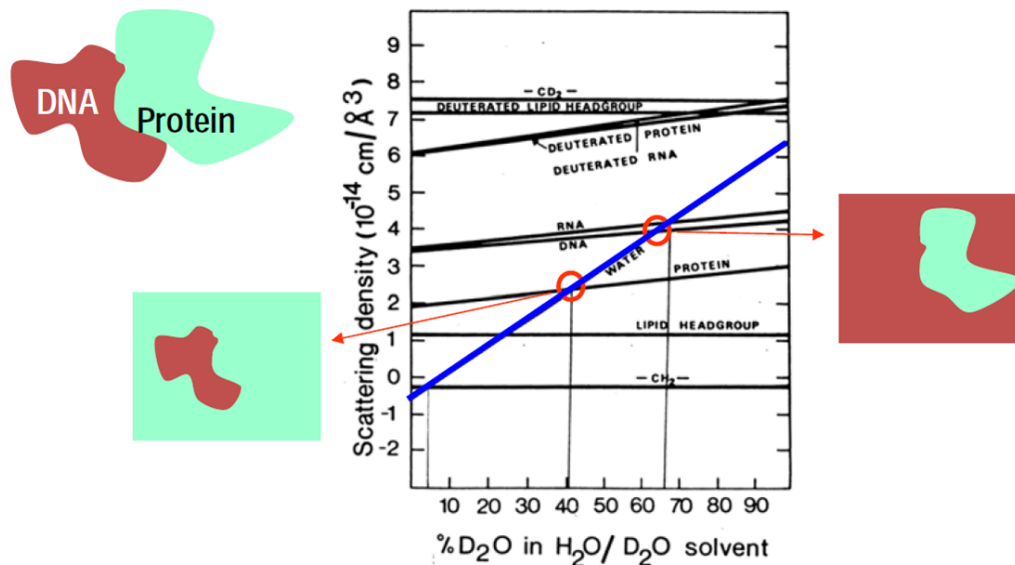


Figure 2.3.: Contrast matching in neutron scattering experiments. Adapting the $\text{H}_2\text{O}/\text{D}_2\text{O}$ concentration, changes the scattering length density of the solvent (blue line). The scattering density can be adjusted to match the scattering density of special parts within your sample, as it is shown for a DNA/protein complex, where firstly the DNA is highlighted and then the protein is highlighted, whereby the scattering density of the solvent is contrast matched with the DNA scattering density.

D_2O can be used for contrast variation as it is shown in Fig. 2.3. Depending on the $\text{H}_2\text{O}/\text{D}_2\text{O}$ ratio either the protein can be contrast matched, so that only the DNA is highlighted or vice versa. Furthermore, parts of a lipid, such as the hydrocarbon chain, can be deuterated to increase the SLD and contrast match it with the solvent. There are many possibilities to play around with contrast in SANS making it a powerful tool.

2.2. Scattering density profile model (SDP–analysis for MLVs)

Based on the GAP (global analysis program) model of Pabst et al. [172, 176] and the SDP (scattering density profile) model of Kučerka et al. [173] we

2. Methods

implemented a novel high resolution global analysis technique for the scattering profile of MLVs, termed herein SDP–GAP analysis. The model describes the scattering intensity $I(q)$ through the whole q –range in terms of a structure factor $S(q)$ describing the interbilayer structure and a form factor $F(q)$ modeling the bilayer structure:

$$I(q) = \frac{1}{q^2} \left[|F(q)|^2 S(q) (1 - N_{diff}) + |F(q)|^2 N_{diff} \right], \quad (2.7)$$

where N_{diff} is the diffuse scattering from positionally uncorrelated bilayers and unilamellar vesicles [172]. According to Debye [177] $S(q)$ and $F(q)$ can be treated separately, because of the independence of intrabilayer fluctuations and interbilayer lattice fluctuations. This model was applied to scattering profiles of fluid phase MLVs containing one lipid species only and MLVs of binary lipid mixtures containing cholesterol. In the next chapter 2.3 the enhancement of this model to multicomponent mixtures and phase separated lipid mixtures will be described.

2.2.1. Parsing scheme for phosphatidylcholine lipids

The form factor within the SDP–GAP model describes the structure of the bilayer along the bilayer normal in terms of differences in electron densities (ED) or neutron scattering length densities (NSLD) between various components of the lipid molecule. In the following only $\Delta\rho$ and ρ as definition for electron densities are used whereby formulas are also valid for ΔNSLD and NSLD defining neutron scattering densities. The form factor is further on the Fourier transform of the electron density or neutron scattering length density profile:

$$F(q) = 2 \int_0^D \Delta\rho(z) \exp[-iqz] dz, \quad (2.8)$$

where $\Delta\rho(z)$ is the water subtracted net electron or neutron scattering length density profile as a function of the coordinate z (normal to the bilayer) and the integration proceeds from $z = 0$ at the bilayer center to D , where $\Delta\rho(z) = 0$. Integration limits and the factor 2 in Eq. 2.8 are due to bilayer symmetry. The model should then carefully represent the total

2.2. Scattering density profile model

scattering density profile $\Delta\rho(z)$ of a bilayer. Therefore Kučerka et al.[173] have implemented a model, where they describe the bilayer in terms of volume probability distributions for various lipid components. Further on $\Delta\rho(z)$ could be calculated by the multiplication with the appropriate ED or NSLD:

$$\Delta\rho(z) = \sum(\rho_i - \rho_W)P_i(z), \quad (2.9)$$

where ρ_W is the ED/NSLD of water ($\rho_W = 0.33 \text{ e}^- \text{ \AA}^{-3} / -5.6 \text{ e}^- \text{ \AA}^{-2}$), ρ_i is the ED/NSLD of the i^{th} molecular lipid fragment and $P_i(z)$ represents the volume probability distribution of the molecular fragments as a function of z ($i = \text{CholCH}_3, \text{PCN}, \text{CG}, \text{CH}_2, \text{CH}_3$; see explanation next paragraph). The appropriate parsing of the lipid molecule into various component groups is an essential feature of the SDP model. The parsing scheme is based on distinct features of the scattering density profile for x-rays and neutrons. The grouping of atoms to component groups is therefore guided by the scattering contrast of different fragments for both x-rays and neutrons to have one model with the highest contrast for both scattering profiles. This joint analysis of SAXS and SANS will be discussed in section 2.2.7.

To obtain the best parsing scheme for PC lipids, Kučerka et al.[173] performed MD-simulations of a DOPC bilayer and calculated the ED/NSLD of individual lipid moieties (choline, phosphate, glycerol, carbonyl, CH, CH₂, CH₃) that are shown at the left side of Fig. 2.4. Due to this distribution of the single moieties they combined several components to simplify the model and reduce the number of parameters needed for the description of a bilayer as it is shown at the right side: CholCH₃ (three CH₃ choline groups), PCN (phosphate+CH₂CH₂N), CG (carbonyl+glycerol). As the headgroup is the same for all PC lipids and they only differ in their hydrocarbon chain length and the number of unsaturation, this model can be used for all PCs. In the case of x-rays the ED of CH and CH₂ group is nearly the same and so the model was further simplified by describing the CH groups as part of the whole hydrocarbon chain (CH₂), also because mostly SAXS experiments were performed in this work. This leads to the final parsing scheme, which was implemented for single lipid systems and that is shown in Fig. 2.5 for DPPC.

The bottom panel of Fig. 2.5 represents the volume probability (VP) distribution of the molecular fragments of DPPC that are described by Gaussian

2. Methods

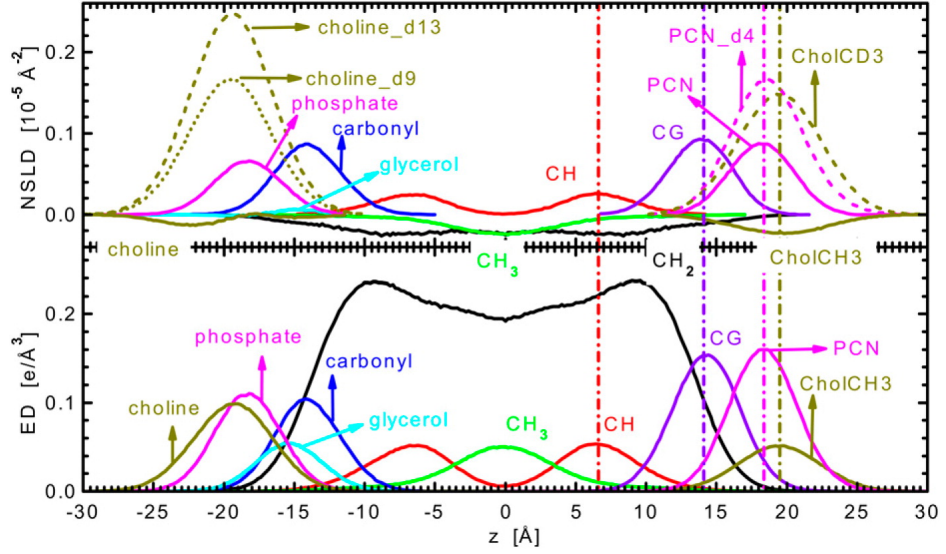


Figure 2.4.: ED/NSLD profile of a DOPC bilayer from MD-simulations. The abscissa represents the distance along the bilayer. The left panel shows single lipid moieties and the right panel shows the combined components and hence the final parsing scheme for PC lipids. Dashed vertical colored lines define the position of each component along the bilayer normal and dashed lines in the upper panel depict deuterated headgroup fragments. [173]

or error functions and because of symmetry only one leaflet of the bilayer is shown. The Gaussians representing the VP distributions of CholCH₃, PCN, CG and CH₃ are defined as follows:

$$P_i(z) = \frac{c_i}{\sqrt{2\pi}} \left(\exp \left[-\frac{(z + z_i)^2}{2\sigma_i^2} \right] + \exp \left[-\frac{(z - z_i)^2}{2\sigma_i^2} \right] \right), \quad (2.10)$$

where the two expressions describe the symmetric bilayer leaflets, z_i defines the position of the i^{th} molecular fragment along the bilayer normal and c_i constrains the height of the Gaussians as follows:

$$c_i = \frac{n_i V_i}{A' \sigma_i}. \quad (2.11)$$

n_i accounts for the number of each molecular fragment within the lipid, V_i is the molecular volume, σ_i is the standard deviation in the Gaussian

2.2. Scattering density profile model

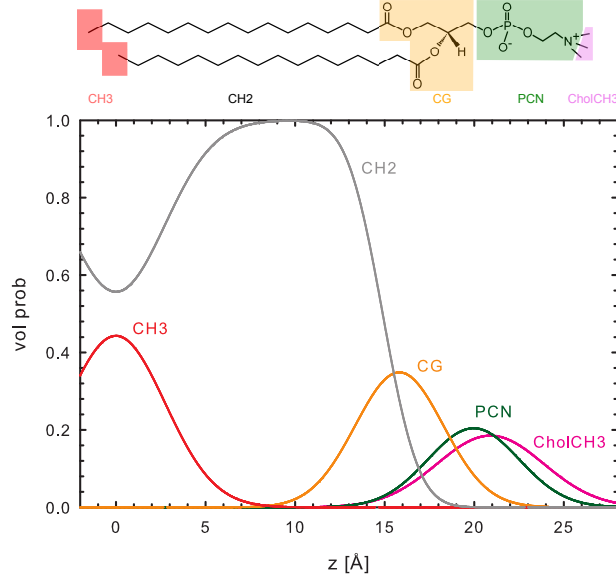


Figure 2.5.: Generic parsing scheme (upper panel) and volume probability distribution (lower panel) for DPPC. [178]

function representing the width of the Gaussian and A' is a free parameter describing the area per lipid but is used as a scaling factor. The lateral area per lipid for a bilayer is then calculated differently as described in section 2.2.5.

The hydrocarbon chains (HC) are described by error functions:

$$P_{HC}(z) = \frac{1}{2} [\text{erf}(z, -z_{HC}, \sigma_{HC}) - \text{erf}(z, z_{HC}, \sigma_{HC})], \quad (2.12)$$

where z_{HC} and σ_{HC} are the position and the width of the step in the error function:

$$\text{erf}(z, z_i, \sigma_i) = \frac{2}{\sqrt{\pi}} \int_0^{\frac{z-z_i}{\sqrt{2}\sigma_i}} \exp[-x^2] dx. \quad (2.13)$$

The VP distribution for CH_2 groups is then described by:

$$P_{\text{CH}_2}(z) = P_{HC}(z) - P_{\text{CH}_3}(z), \quad (2.14)$$

satisfying the spatial conservation in the hydrocarbon chain region of the bilayer, where the total VP is one. Due to the spatial conservation

2. Methods

argument, the VP distribution of water can be calculated as follows:

$$P_W(z) = 1 - P_{CholCH_3}(z) - P_{PCN}(z) - P_{CG}(z) - P_{CH_2}(z) - P_{CH_3}(z). \quad (2.15)$$

2.2.2. Incorporation of cholesterol in the SDP model

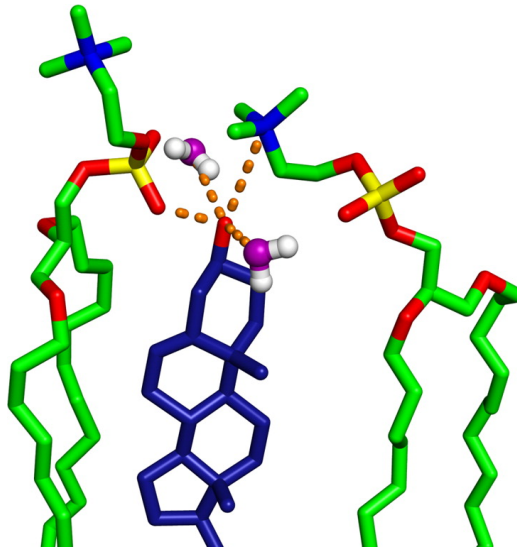


Figure 2.6.: Cholesterol–lipid interactions shown by MD–simulations. The orange dashed lines represent possible hydrogen bonds between cholesterol’s (blue) OH group (red), lipids (green) and water molecules (purple). [67]

In our model for lipid mixtures containing cholesterol, the cholesterol molecule was incorporated into the volume probability distribution of the bilayer. In this work two different models for cholesterol were applied. The first one merges cholesterol’s VP distribution with that of CH_2 due to its localization within the hydrocarbon chain region [67]. The localization of cholesterol can be explained by the strong hydrophobic interaction with the lipid chains and the interaction of the hydroxy group with the lipid’s headgroup, where they tend to form H–bonds (see chapter 1.2.1 and Fig. 2.6) [51, 67]. Figure 2.6 also shows molecular differences between cholesterol and the hydrocarbon chains, where cholesterol exhibits a ring structure right after the hydroxy group. This difference can be also seen in

2.2. Scattering density profile model

the electron density, which is higher for cholesterol and hence ρ_{CH_2} is also higher for binary mixtures and has to be considered in the analysis. This is realized by a variable value for the electron density of CH_2 group:

$$\rho_{CH_2} = \frac{N_{CH_2}^{e^-}}{V_{CH_2}}, \quad (2.16)$$

where N_{e^-} accounts for the number of electrons in the CH_2 group and the volume of the methylene group V_{CH_2} is introduced as a free parameter adjusting ρ_{CH_2} .

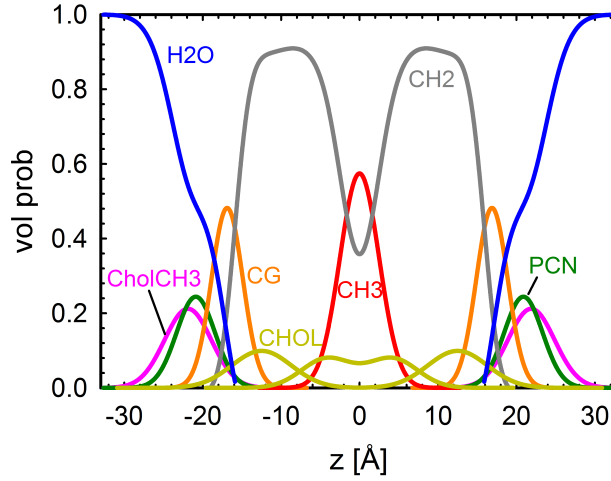


Figure 2.7.: Volume probability distribution of a PC bilayer containing cholesterol. Cholesterol is modeled by two Gaussian functions, one for the headgroup and one for the tail that is towards the bilayer center (yellow lines).

The second model describes the cholesterol molecule as two additional individual Gaussians as it is shown in Fig. 2.7 (yellow lines). One Gaussian for the ringstructure including the hydroxy group (headgroup) and one for the hydrocarbon tail. This is justified by MD-simulations and SAXS experiments where Kučerka and Pan [67, 179] showed that there are differences in the ED profile of cholesterol and therefore cholesterol can be represented by these two Gaussians. Although it will add six new fit parameters to the model, there are some constraints due to MD-simulations that can be applied. The width of the head and tail Gaussians are $\sigma_{chol-H} = 3.8 \text{ \AA}$ and $\sigma_{chol-T} = 3.2 \text{ \AA}$. The head to tail distance is set to $z_{chol-H} - z_{chol-T} =$

2. Methods

8.3 Å, the volume ratio between head and tail is 0.6 and the total cholesterol volume is taken to be $V_{chol} = 630 \text{ \AA}^3$ [180]. Values were provided by Jianjun Pan as a result of MD-simulations and experiments.

Calculating the ED and NSLD of cholesterol's head and tail bears a big difference between head and tail as a further justification for the parsing of cholesterol. $\rho_{chol-H} = 0.40 \text{ e}^{-\text{\AA}^{-3}}$, $\rho_{chol-T} = 0.26 \text{ e}^{-\text{\AA}^{-3}}$, $\text{NSLD}_{chol-H} = 6.3 \text{ e}^{-7} \text{ \AA}^{-2}$ and $\text{NSLD}_{chol-T} = -4.1 \text{ e}^{-7} \text{ \AA}^{-2}$. The cholesterol's Gaussians are mathematically treated in the same way as the other functions for the molecular fragments of the lipid, while satisfying spatial conservation and therefore the VP distribution for the hydrocarbon chain is defined as:

$$P_{CH2}(z) = P_{HC}(z) - P_{CH3}(z) - P_{chol-H}(z) - P_{chol-T}(z), \quad (2.17)$$

where $P_{chol-H}(z)$ and $P_{chol-T}(z)$ are the volume probability functions of the cholesterol's head and tail respectively and are defined as in Eq. 2.10. The amount of cholesterol in the bilayer is considered by a scaling factor for both Gaussians, which can be also used as a fitting parameter.

2.2.3. SDP analysis for MLVs

As described in Eq. 2.7 the full q -range model contains a form factor characterizing the bilayer ED profile and an independent structure factor accounting for the quasicrystalline behavior of the bilayer stacks in multilamellar vesicles. Due to the sphericity of MLVs, the bilayer stacks can be treated as a one dimensional lattice with a lattice constant d , defining the lamellar repeat distance of the bilayers (see Figs. 1.5,1.6). The Bragg reflections, resulting from positionally correlated bilayers, do not appear as an infinitely sharp Bragg peak, but are smeared out and disappear at higher orders due to bilayer undulations and the number of positionally correlated bilayers [172, 176]. This behavior of the structure factor $S(q)$ for fluid lipid bilayers can be described by the Caillé theory [181], where bilayer bending fluctuations are considered. In a modified version of the Caillé theory (MCT) $S(q)$ is defined as following [172, 176, 182]:

$$S(q) = N + 2 \sum_{k=1}^{N-1} (N-k) \cos(kqd) e^{-(d/2\pi)^2 q^2 \eta \gamma} (\pi k)^{-(d/2\pi)^2 q^2 \eta}, \quad (2.18)$$

2.2. Scattering density profile model

where N denotes the number of coherent scattering bilayers, d is the lattice constant, γ is Euler's constant ($\gamma = 0.5772$) and η describes the Caillé parameter:

$$\eta = \frac{\pi k_B T}{2d^2 \sqrt{K_c B}} \quad (2.19)$$

where $k_B T$ is the thermal energy, B is the bulk modulus of compression and K_c determines the bilayer bending rigidity. The MCT structure factor accounts for bending fluctuations of fluid membranes that are caused by undulations as it is shown schematically at the left panel in Fig. 2.8. The right panel exhibits a calculated $S(q)$ where the smearing of Bragg peaks and the fast disappearance of Bragg reflections at higher orders can be seen. The Caillé parameter can be therefore understood as a measure of the bilayer flexibility and Petrache et al. [183] showed by hydration studies that the B and K_c can be even decoupled and determined experimentally.

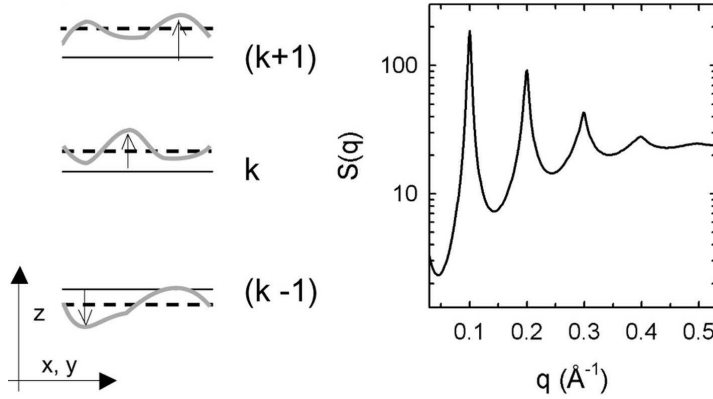


Figure 2.8.: Schematic representation of bilayer undulations. Bending fluctuation disorder due to bilayer undulations can be described by the modified Caillé theory (MCT) resulting in a structure factor for Bragg reflections as shown at the right panel. This kind of disorder describes best the L_α phase. [176]

Figure 2.9 represents the influence of the mean number of coherently scattering bilayers (N) on $S(q)$ in the MCT. As N increases, the peaks get narrower and higher. Another feature appears in the low q -regime for a small and fixed value of N , which is represented by the solid line. It shows oscillations that could not be found experimentally and which can be attributed to artifacts due to monodispersity in the number of bilayer

2. Methods

stacks [184]. Therefore Fröhlich et al. [184] implemented a polydisperse structure factor by calculating a series of $S(q)$ with various numbers of bilayers N . According to Fröhlich et al. [184] a polydisperse structure factor was implemented in this analysis. A Gaussian distribution is used for the structure factor series, which is approximated by a discrete series with n_{SF} sampling points:

$$n_{SF} = \text{int}[30 / \log(N)] \quad (2.20)$$

and truncated to the next odd number. The standard deviation for the Gaussian distribution is:

$$\sigma = \begin{cases} \sqrt{N} & \text{for } N \geq 5 \\ 0.5(N - 1) & \text{for } N < 5 \end{cases} \quad (2.21)$$

with the condition $N \geq 2$. The calculated n_{SF} structure factors in the interval $N \pm 2\sigma$ are then weighted by:

$$x_i = \frac{1}{\sigma\sqrt{2\pi}} \exp\left[-\frac{(N_i - N)^2}{2\sigma^2}\right], \quad (2.22)$$

where N_i accounts for one of the n_{SF} bilayer numbers N .

2.2.4. Constraining the free parameter space

The model exhibits a huge number of free parameters (e.g. 21) including position and width of Gaussians describing VP distribution, partial volumes of molecular lipid fragments, parameters for the structure factor calculation such as lattice constant, number of coherent scattering bilayers N , N_{diff} , Caillé parameter η , a constant background for diffuse scattering and a scaling factor to rescale the model intensity against the experimentally measured intensity. To avoid nonphysical results, some of these parameters are constrained to fixed values or "soft constrained" to a physical meaningful interval.

According to Klaua et al. [185] and Kučerka et al. [173] following constraints were implemented. As the model describes a symmetric bilayer

2.2. Scattering density profile model

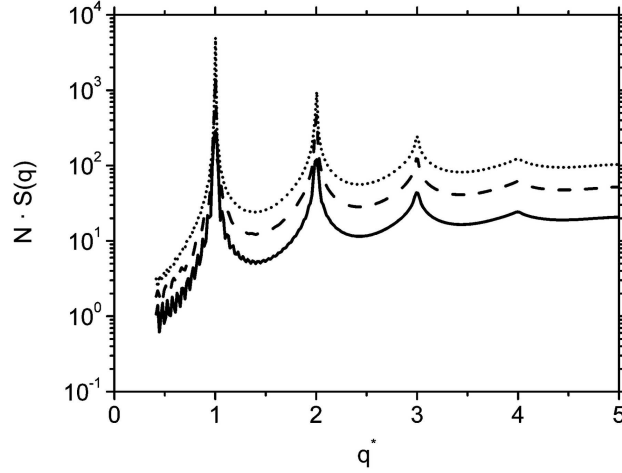


Figure 2.9.: Various Structure factors for different numbers of bilayer stacks N . $S(q)$ was calculated for a fixed value of $\eta = 0.1$ and $N = 20$ (solid line), $N = 50$ (dashed line), $N = 100$ (dotted line). An increase of N is associated with a narrowing of Bragg peaks and a reduction of undulations in the low q -regime. [184]

(see Fig. 2.7) the position of the central methyl group z_{CH3} is set to zero and the amplitude of the error function, representing the hydrocarbon chain region, is constrained to one, because of spatial conservation. Due to MD-simulations and experiments Klauda et al. [185] suggested to constrain the width of the hydrocarbon chain describing error function σ_{HC} within limits of 2.4–2.6 Å and the width of the choline methyl groups $\sigma_{CholCH3}$ is set to 2.98 Å [173].

In addition to those constraints, we implemented two more physically reasonable constraints to aid the data analysis for x-rays only. Firstly, the volumes of parsed molecular groups that are necessary for the calculation of scattering densities and that affect the amplitude c_i of the Gaussian functions, are taken from previous reports [173, 180, 185–187] and are soft constrained to vary by $\pm 20\%$. Although a change in these volumes affects the amplitude of the electron density profile slightly, the positions z_i remain mainly unaffected and vary only within stated uncertainties. Secondly, due to spatial proximity between the hydrocarbon chain interface (z_{HC}) and the backbone (z_{CG}), and the PCN (z_{PCN}) group and the choline methyl group ($z_{CholCH3}$), which is covalently bonded to PCN,

2. Methods

the distances between them are not allowed to exceed 2 \AA . This spatial constraint is also justified by scattering experiments, MD-simulations and NMR measurements [173, 185, 187, 188].

2.2.5. Determination of bilayer structural parameters

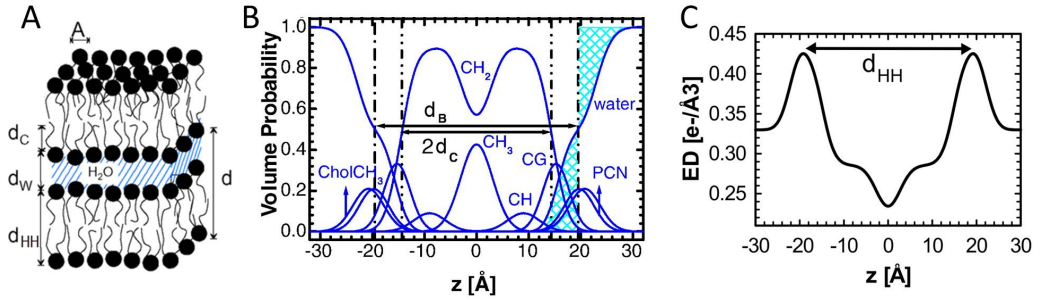


Figure 2.10.: Illustration of bilayer structural properties. Panel (A) shows the lamellar repeat distance d of bilayers, the headgroup to headgroup distance d_{HH} , the hydrocarbon chain length d_C , the water layer thickness d_W between bilayers and the lateral area per lipid A . (B) Bilayer thickness d_B is defined by the volume probability function of water and d_C is the position of the error function for the hydrocarbon chain. (C) The distance between the maxima in the electron density profile determines d_{HH} . (adapted from [187])

Based on the results for the VP distributions and ED profiles, which can be obtained from the analysis, structural properties of a lipid only membrane can be calculated. Figure 2.10 shows a schematic representation of structural parameters that are defined as follows. The hydrocarbon chain length d_C (Fig. 2.10A,B) is defined as the position of the chain representing error function z_{HC} . Also in Fig. 2.10B the bilayer thickness d_B defined as the Luzzati thickness [189] is shown and can be calculated by the integration of the water probability distribution, where the integrated water probabilities and integrated deficient water probabilities to the left and the right side of the Luzzati surface are compared (indicated in cyan at the right water function) [173]:

$$d_B = d - \int_0^{d/2} P'_W(z) dz. \quad (2.23)$$

2.2. Scattering density profile model

To increase the robustness of the determination of d_B in the x-ray standalone analysis, $P_W(z)$, as defined in Eq. 2.15 and obtained from the analysis, is fitted with an error function ($P'_W(z)$) by giving more weight to the headgroup region, where the scattering contrast is higher than in the hydrocarbon chain region. Also the structural results regarding the headgroup region are more robust. During the process of development we implemented $P'_W(z)$ as a model function in the SDP analysis, but the results were not adequate whereas by using Eq. 2.23 bilayer thicknesses of single lipid systems compared well with previous reported results [173, 187].

The calculation of the lateral area per lipid A as well as the water layer thickness d_W (Fig. 2.10) are both based on the bilayer thickness:

$$A = 2V_L/d_B, \quad (2.24)$$

where V_L is the total lipid volume [173]. V_L was either measured separately by dilatometry measurements [190] using the density sound analyzer DSA5000 (Anton Paar, Graz, Austria) or taken from previously published volumetric data [180, 191–194]. The water layer thickness d_W between adjacent bilayers (Fig. 2.10A) is then defined as:

$$d_W = d - d_B. \quad (2.25)$$

Previously defined structural parameters are all based on the volume probability distribution of molecular lipid fragments within a bilayer, whereas the headgroup to headgroup distance d_{HH} is defined as the distance between the two maxima of the total electron density profile representing the headgroup region (see Fig. 2.10).

2.2.6. Optimization routine based on the genetic algorithm

The model intensity described in Eq. 2.7 is based on the form factor and structure factor of the sample, but does not contain any information about

2. Methods

instrumental influence. The finite instrumental resolution is taken into account by a vertical beam profile $v(q)$ and following convolution:

$$I_{abs}(q) = \beta \int_{-\infty}^{+\infty} I(q')v(q - q')dq' + \kappa, \quad (2.26)$$

where β is an instrumental scaling constant and κ accounts for a constant offset. The vertical profile of the primary beam can be recorded and modeled with a Gaussian profile for the instrumental resolution function:

$$v(q) = \exp \left[-\frac{q^2}{2\sigma_v^2} \right], \quad (2.27)$$

where σ_v^2 is the standard deviation of the Gaussian profile.

The final intensity $I_{abs}(q)$ (Eq. 2.26) with a large number of adjustable parameters (21) has to be optimized against the experimental SAXS (and SANS) data. Due to the large number of fitting parameters a genetic algorithm (GA) is used in the optimization routine to obtain the best fit. Compared to common gradient descent methods or other optimization routines like Levenberg–Marquardt, the GA based fitting procedure does not get stuck in local minima so easily [195]. The GA is an optimization tool that generates solutions using the mechanism of natural evolution or selection such as mutation, crossover and inheritance. Starting with a random set of individuals or free fitting parameters called a population that are within predefined limits, the goodness of fit for each individual parameter set is tested. The fitness is determined by the reduced chi squared value χ^2 , which is defined as the sum of squared residuals divided by the degrees of freedom [196]:

$$\chi^2 = \frac{1}{n - p} \sum_{k=1}^n \frac{1}{\sigma_k^2} [I_{exp}(q_k) - I_{abs}(q_k)]^2, \quad (2.28)$$

where p is the number of free parameters, n accounts for the number of data points, and $I_{exp}(q_k)$ and σ_k^2 are the measured scattering intensities and their standard deviation. A proportion of the best individuals is then selected to breed new individuals (termed children) by genetic methods such as crossover or recombination and mutation. Individuals with a bad

2.2. Scattering density profile model

fitness are replaced by new random individuals (parameter sets) or are used for crossovers to preserve genetic diversity. Thus a new generation of population is created with a generally higher fitness than the former generation but it exhibits similar characteristics as the former one. This simplified procedure takes place in every iteration (also called generation) until a defined termination condition is fulfilled.

For this work all analysis routines were implemented in IDL (Interactive Data Language) using the IDL optimization routine *SOLBER* including a GA based optimization [197]. Within the optimization procedure for one data set populations of ~ 2000 – 5000 individuals within hundreds of generations are tested for their fitness. If the fitness does not increase after 100 generations or iterations, the termination condition is reached and the optimization has converged. The individuals (parameter sets) with the highest fitness (lowest χ^2 values) are then compared regarding differences in their parameters and an uncertainty for all parameters of $\pm 2\%$ is assumed. By calculating the standard deviation of the distribution for each parameter the error can be even further quantified and small variations in uncertainties could be observed depending on the robustness of a parameter. For example z_{PCN} has smaller uncertainties than z_{HC} due to the higher scattering contrast in the electron rich headgroup region. As the computational costs for a GA are higher than for common optimization routines, parallel processing techniques are used to decrease the runtime for one data set by a factor of ~ 4 . Typical running times are between 2 and 5 hours on a six core machine (Intel Xeon 2.67 GHz).

2.2.7. Joint refinement of small angle x-ray and neutron scattering

The SDP analysis is based on volume probability distributions of the bilayer's molecular fragments and therefore either x-ray data or neutron data or even both can be analyzed separately or simultaneously by scaling the VP distribution functions $P_i(z)$ with the appropriate scattering length densities ρ_i (ED or NSLD) as it is shown in Eq. 2.9. Compared to x-rays in neutron scattering experiments the scattering contrast can be varied by changing the NSLD of the solution (D_2O/H_2O ratio) and by changing

2. Methods

the NSLD of certain parts of the lipid. A common tool therefore is the deuteration of hydrocarbon chains where the protons are chemically replaced by deuteriums, but the same can be also done for the headgroup region [198, 199]. The deuterium in the chain region shifts the NSLD from negative to positive values and hence the net NSLD, relative to the NSLD of the solution, is changed significantly for the hydrocarbon region.

The analysis and optimization procedure for a single SANS data set is the same as for a SAXS data set but replacing the electron densities by neutron scattering length densities in Eq. 2.9. Due to the mutual VP distribution both data sets (SAXS and SANS) can be also analyzed simultaneously or even more scattering profiles at different contrasts can be used for a joint analysis adapting only the scattering length densities for each sample. The parameters for the instrumental influence, such as β and κ in Eq. 2.26, also have to be adapted and in addition to the smearing effect due to the instrumental resolution the effect of wavelength smearing has to be taken into account. This is considered by the convolution (see Eq. 2.26) with a Gaussian resolution function $p(q)$ [200]:

$$p(q) = \left(\frac{1}{2\pi\sigma_p^2} \right)^{1/2} \exp \left[-\frac{q^2}{2\sigma_p^2} \right], \quad (2.29)$$

where σ_p is the SANS resolution variance (instrumental resolution and wavelength smearing) that is determined by the instrument for every q -value. The fitness (χ^2) of each scattering pattern is then calculated and weighted after any iteration to obtain a total fitness for all data sets used within one analysis. The weighting of data sets can be adjusted depending on the quality and the significance of the data.

In this work ULVs ($r = 50$ nm) and MLVs of POPC (Fig. 2.11A) and POPC-d₃₁ (one deuterated hydrocarbon chain, Fig. 2.11B) in pure D₂O were used for SANS experiments at the Oak Ridge National Laboratory (for further information see [178]). To reduce the incoherent background scattering originating from the large incoherent cross section of hydrogen compared to deuterium [201], all samples were measured in pure D₂O. Regarding the analysis, firstly each SANS data set was jointly analyzed with the corresponding SAXS scattering profile of POPC. Secondly all scattering patterns (SAXS and SANS) at various contrasts were analyzed

2.3. SDP–GAP analysis for phase separated bilayer mixtures

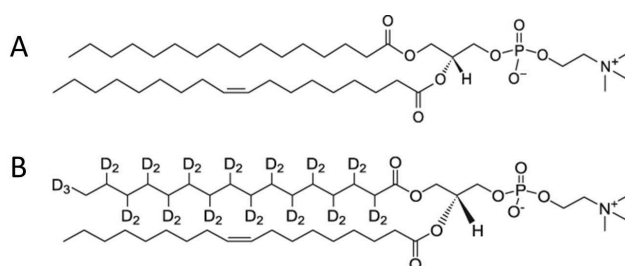


Figure 2.11.: Chemical representation of POPC (A) and POPC-d₃₁ (B).

simultaneously to see whether or not the extra information obtained from SANS profiles alters the results.

2.3. SDP–GAP analysis for phase separated bilayer mixtures

The analysis described in the previous sections is applicable for homogeneous lipid mixtures containing one lipid species or even more complex mixtures with cholesterol as long as the bilayer is homogeneous and the MLVs exhibit only one lattice with one lattice constant d resulting in a single Bragg reflection (Fig. 2.2). Inhomogeneous bilayer mixtures on the other hand can exhibit phase separation into L_o/L_d domains with different bilayer thicknesses (Fig. 2.12). Moreover these domains can align on top of each other resulting in two distinct lattice constants describing two different lattices within MLVs. Figure 2.12 shows schematically this alignment and the two Bragg reflections that are indicated with an "O" for the L_o phase and with an "X" for the L_d phase. This allows us to distinguish between the two phases by applying a new model with two distinct form factors and structure factors describing the L_o and L_d phases separately. As the q -resolution for SANS is not as high as for SAXS, such two distinct Bragg reflections are hardly to detect. Therefore this analysis is implemented for standalone SAXS data although it can be enhanced to a joint analysis of SAXS/SANS data exhibiting phase separation. The inset in the scattering pattern shows the ED profiles of the coexisting L_o and L_d

2. Methods

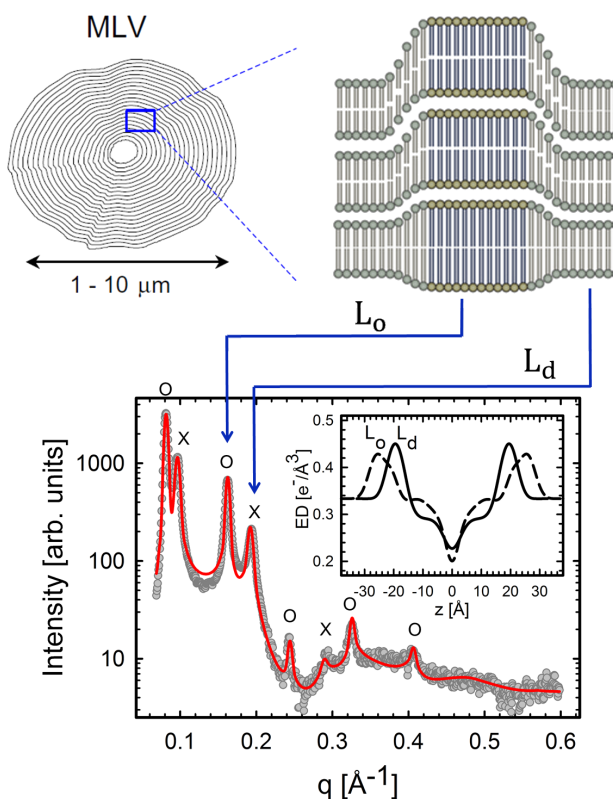


Figure 2.12.: Schematic representation of a SAXS experiment for L_o/L_d phase coexistence. L_o/L_d domains can align across many bilayers within MLVs resulting in a lattice with two different lattice constants (lamellar repeat distances). Therefore two Bragg reflections from aligned L_o (O) and L_d (X) domains are observed in the x-ray scattering pattern. The inset within the scattering profile shows the calculated electron density profiles of the L_o and L_d phase. (adapted from [102, 175])

phase as a result of this new analysis technique for coexisting phases that will be explained in more detail in the next sections.

2.3.1. Parsing scheme for lipid mixtures

To calculate form factors for the L_o and L_d phase that contain different amounts of three or even four different lipids, primarily an effective lipid molecule with an appropriate parsing scheme has to be defined. As only

2.3. SDP-GAP analysis for phase separated bilayer mixtures

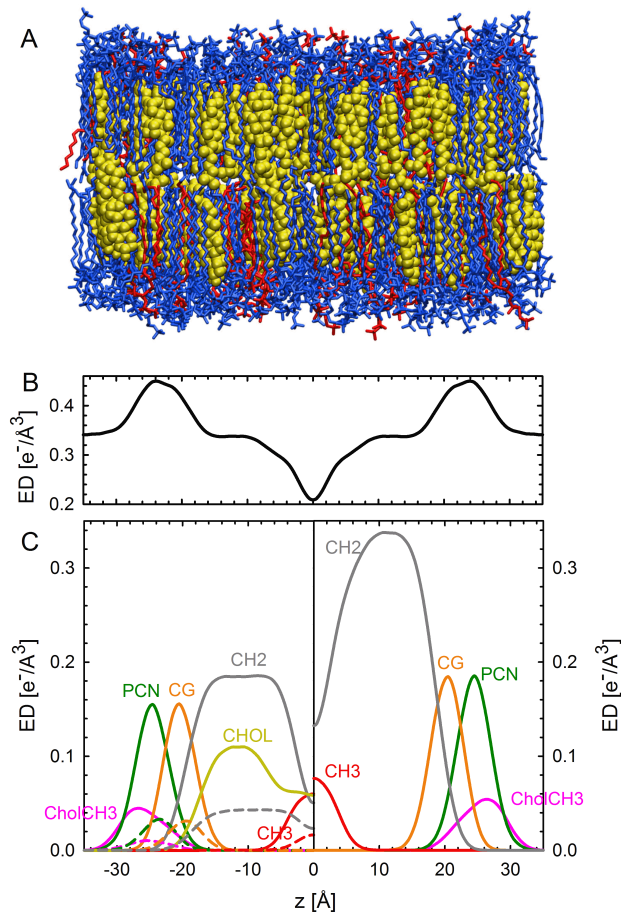


Figure 2.13.: Parsing scheme of the DOPC/DPPC/CHOL (0.12/0.58/0.30) lipid mixture (L_o phase) based in MD-simulations. (A) Snapshot of the simulated bilayer, where DOPC is labeled in red, DPPC in blue and CHOL in yellow. (B) electron density profile of the bilayer. (C) Left panel shows the ED profile of molecular fragments of DPPC (solid lines), DOPC (dashed lines) and CHOL (yellow line). The right panel represents the parsing scheme of the lipid mixture, where contributions of single molecules are merged due to their positional correlation. [202]

PC lipids are used, the molecular headgroup structure is the same for all lipids. Hence the contributions of saturated and unsaturated lipids can be merged to one common lipid chain and an effective PC lipid molecule can be defined. Further on cholesterol was added to the model either by merging their contribution with the hydrocarbon chain region or by using

2. Methods

two distinct Gaussian functions representing cholesterol's head and tail respectively as described in section 2.2.2.

The previously defined parsing scheme (see section 2.2.1) is also used for the effective lipid molecule. Saturated and unsaturated lipids differ with respect to their number of CH and CH₂ groups but due to the low x-ray scattering contrast between methylene and methine groups, they are merged in the same way as discussed previously (section 2.2.1). The merging of saturated and unsaturated lipids, although they have a different number of CH₂ groups, is justified by previously reported MD-simulations data [158] of DOPC/DPPC/CHOL mixtures. Figure 2.13A shows a snapshot where the positional correlation of saturated (blue) and unsaturated (red) lipids is qualitatively shown. This was further quantified by the calculation of ED profiles for both lipid species (Fig. 2.13C) showing the positional overlap of the molecular fragments of both lipids (solid and dashed lines in left panel) justifying the parsing scheme for an effective lipid molecule (right panel). The total ED profile of the DOPC/DPPC/CHOL bilayer is shown in Fig. 2.13B.

2.3.2. Analysis of aligned L_o/L_d domains

As it is shown in Fig. 2.12 the scattering pattern exhibits two distinct Bragg reflections and consists of two form factors, one for the L_o and one for the L_d phase. To describe a scattering profile of coexisting phases the model intensity of Eq. 2.7 has to be extended. Therefore a linear combination of individual L_o/L_d scattering intensities ($I_{L_o}(q)$ and $I_{L_d}(q)$) was implemented while not considering potential L_o/L_d cross correlations:

$$I(q) = \frac{1}{q^2} [c_{L_d} I_{L_d}(q) + (1 - c_{L_d}) I_{L_o}(q)], \quad (2.30)$$

where c_{L_d} accounts for the L_d phase fraction. Scattering intensities from L_o/L_d domains are defined as follows:

$$I_{L_o}(q) = S_{L_o}(q) |F_{L_o}(q)|^2 (1 - N_{diff}^{L_o}) + |F_{L_o}(q)|^2 N_{diff}^{L_o}, \quad (2.31)$$

$$I_{L_d}(q) = S_{L_d}(q) |F_{L_d}(q)|^2 (1 - N_{diff}^{L_d}) + |F_{L_d}(q)|^2 N_{diff}^{L_d}. \quad (2.32)$$

2.3. SDP-GAP analysis for phase separated bilayer mixtures

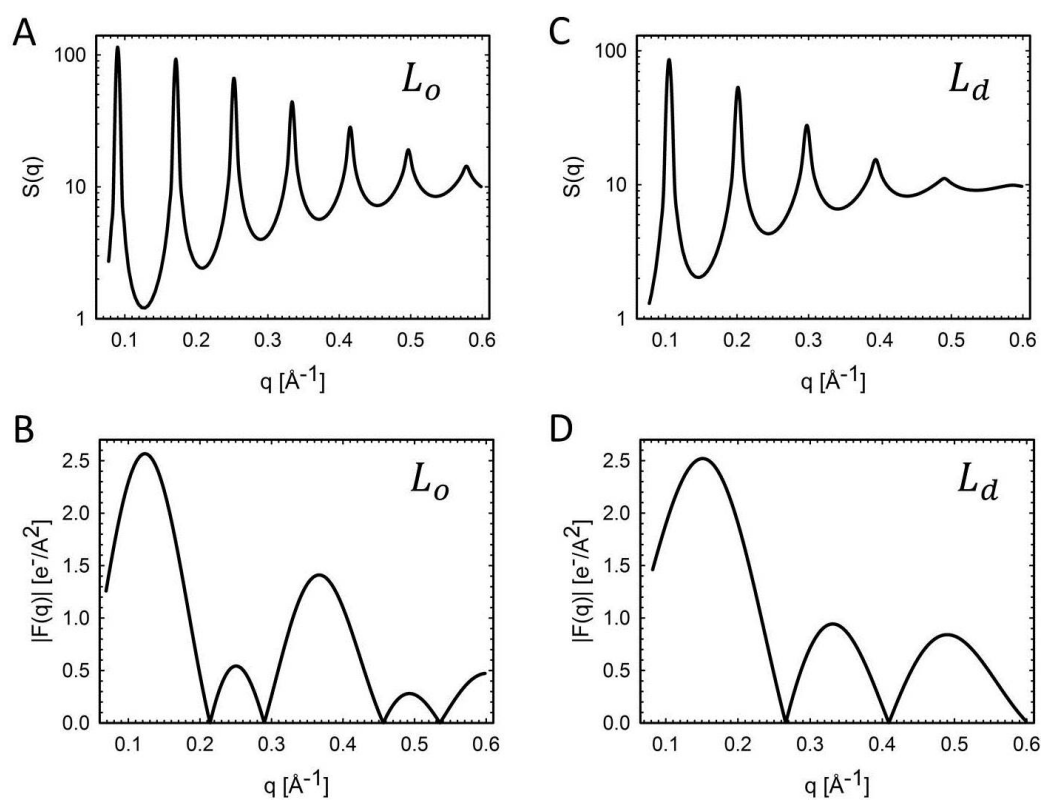


Figure 2.14.: Illustration of structure and form factors of L_o/L_d phases. The left panel shows structure (A) and form factor (B) of the coexisting L_o phase in a DOPC/DSPC/CHOL mixture and right panel shows the structure (C) and form factor (D) of the associated L_d phase.

The subscripts L_o and L_d indicate the L_o/L_d contributions to structure and form factors describing the coexisting L_o/L_d domains. Individual structure and form factors are determined in the same way as defined in Eqs. 2.18,2.8 for homogeneous samples. Figure 2.14 shows such SFs and FFs for L_o phases (left panel) and L_d phases (right panel) respectively. The structure factors differ in their number of Bragg peaks, which is higher for the L_o phase sample that also exhibits narrower Bragg peaks as the positional correlation of bilayers is more pronounced due to the more rigid bilayers. The difference in the form factors is even more obvious. While the shape of the L_d FF is typical for liquid crystalline phases, the behavior of the L_o FF with its smaller second lobe is characteristic for

2. Methods

bilayers with highly ordered hydrocarbon chains containing cholesterol.

Although the number of parameters describing the model increased significantly (nearly a factor of two), the same optimization routine as described before is used (see section 2.2.6). Nevertheless, to increase the robustness of the results, several additional constraints were introduced. Molecular volumes V_i ($i = \text{CholCH}_3, \text{PCN}, \text{CG}$) of the headgroup region are the same for L_o and L_d phase as the headgroup structure does not change between saturated and unsaturated lipids. Values for σ_i ($i = \text{PCN}, \text{CG}, \text{CH}_3, \text{CH}_2$) are constrained to values obtained from the analysis of corresponding tieline endpoint samples describing the coexisting L_o/L_d phases that is justified by the similar composition of endpoint samples and midpoint coexisting phases. Also the distance between hydrocarbon chain interface (z_{HC}) and the position of the CG group (z_{CG}) is constrained to a value obtained from endpoint analysis due to the same reason. Optionally furthermore the distance between phosphate (z_{PCN}) and the CG group (z_{CG}) can also be constrained depending on the quality and resolution of the data.

2.3.3. Analysis of non-aligned coexisting L_o/L_d domains

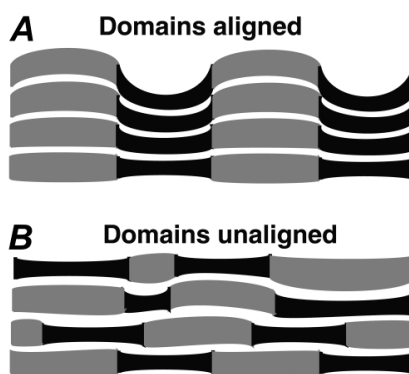


Figure 2.15.: Cartoon of aligned (A) and unaligned (B) L_o (grey) and L_d (black) domains. The white spaces between the bilayers represents interbilayer water layers. [155]

Figure 2.15 shows a cartoon comparing the interbilayer alignment of domains (A) and randomly localized domains (B). The analysis of aligned

2.3. SDP–GAP analysis for phase separated bilayer mixtures

domains has been already discussed but going a step further in our analysis leads to a model that can describe phase coexistence without domain alignment. Due to the loss of domain stacking such a sample exhibits one mean lamellar repeat distance only, which is between that of a pure L_d and a pure L_o phase. But there is still scattering from both domains that contribute to the detected intensity. This can be modeled by two independent form factors describing L_o and L_d domains and a joint structure factor ($S(q)$) describing the mean interbilayer structure:

$$I(q) = \frac{1}{q^2} [S(q)(1 - N_{diff})F_{L_o/L_d}(q) + N_{diff}F_{L_o/L_d}(q)], \quad (2.33)$$

where $F_{L_o/L_d}(q)$ represents the combined L_o/L_d form factor:

$$F_{L_o/L_d}(q) = c_{L_d}|F_{L_d}(q)|^2 + (1 - c_{L_d})|F_{L_o}(q)|^2. \quad (2.34)$$

The scattering profile of such a sample with unaligned domains exhibits distinct Bragg peaks at the first two orders but higher order Bragg reflections disappear abruptly. As such a profile cannot be described by an adequate global structure factor, in Eq. 2.33 $S(q)$ consists of two different structure factors, one describing the low q -regime including the first two orders of Bragg reflections and another one for the high q -regime. To obtain robust results, the same constraints as discussed in section 2.3.2 are applied, including a constraint for the distance between the position of the PCN and CG group.

2.3.4. Determination of area per lipid for complex lipid mixtures

For complex lipid mixtures the area per lipid A can be calculated by Eq. 2.24, whereby the mean total lipid volume V_L of an effective lipid molecule has to be determined. Therefore lipid volumes of each component are determined and a mean volume V_L is calculated by giving weight to the single components with respect to their molar ratios:

$$V_L(T) = \sum_i x_i(T)V_i(T), \quad (2.35)$$

2. Methods

where subscript i denotes the components in lipid mixtures and $x_i(T)$ and $V_i(T)$ are the lipid molar ratios and the total lipid volumes of each component as a function of temperature. For homogeneous mixtures exhibiting one single phase molar ratios are known. In the case of inhomogeneous mixtures showing phase separation, x_i for coexisting L_o/L_d domains at a given temperature are defined by tieline endpoint compositions. $x_i(T)$ cannot be determined exactly but it is estimated using the lever rule and experimentally measured L_o/L_d phase fractions (c_{Ld}). Therefore tieline endpoints as a function of temperature were calculated by determining the distance between tieline midpoints and endpoints ($\bar{L}_d(T), \bar{L}_o(T)$), assuming that tieline inclination remains constant with temperature:

$$\bar{L}_o(T) = c_{Ld}(T)\bar{t}l(T), \quad (2.36)$$

$$\bar{L}_d(T) = c_{Lo}(T)\bar{t}l(T) = (1 - c_{Ld}(T))\bar{t}l(T), \quad (2.37)$$

where $\bar{t}l(T)$ accounts for the overall tieline length as a function of temperature. The behavior of $\bar{t}l(T)$ is estimated to be proportional to the L_o phase fraction and therefore $c_{Lo}(T)$ is fitted by arbitrary functions, which are used to describe the decrease of the total tieline length $\bar{t}l$ as a function of temperature. This analysis is able to reproduce the asymmetric behavior of phase boundaries as the mixing temperature is approached [203] that is due to the increase of c_{Ld} . Figure 2.16 shows these estimated tieline endpoints as a function of temperature for DOPC/DSPC/CHOL and DOPC/DPPC/CHOL.

Temperature dependent lipid volumes $V_i(T)$ for phosphatidylcholines in the liquid crystalline phase are calculated according to Koenig and Gawrisch [193]:

$$V_L(T) = V_H + n_{CH}V_{CH}(0)\alpha_{CH}T + n_{CH2}V_{CH2}(0)\alpha_{CH2}T + n_{CH3}V_{CH3}(T), \quad (2.38)$$

where $V_H = 319 \text{ \AA}^3$ is the constant lipid headgroup volume, $V_{CH}(0) = 21.65 \text{ \AA}^3$ and $V_{CH2}(0) = 27.03 \text{ \AA}^3$ are the fragmental volumes at 0°C of the methin and methylene group respectively, $\alpha_{CH} = 0.022 \text{ \AA}^3\text{deg}^{-1}$ and $\alpha_{CH2} = 0.028 \text{ \AA}^3\text{deg}^{-1}$ are the corresponding temperature coefficients, n_{CH} , n_{CH2} and n_{CH3} account for the number of methin, methylene and methyl groups within the lipid. The temperature dependent volume of the

2.3. SDP-GAP analysis for phase separated bilayer mixtures

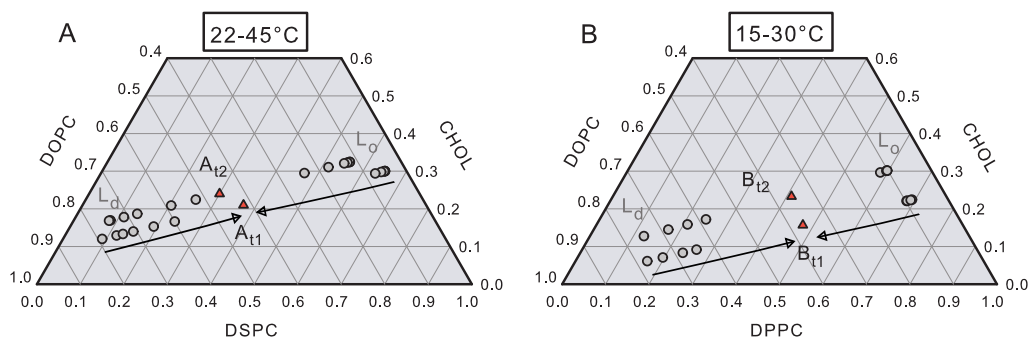


Figure 2.16.: Estimated tieline endpoint behavior as a function of temperature for DOPC/DSPC/CHOL (A) and DOPC/DPPC/CHOL (B). Circles represent tieline endpoints, which move towards midpoints (red triangle) with increasing temperature (5 °C steps) as indicated by the black arrows.

methyl group is defined as $V_{CH_3}(T) = 2V_{CH_2}(0)\alpha_{CH_2}T$ and cholesterol volume within the bilayer is taken to be 630 \AA^3 according to Greenwood et al. [180]. Calculated mean total volumes (2.35, 2.38) of homogeneous three component lipid mixtures are in good agreement with experimentally determined values by dilatometry measurements ($< 2\%$) [190]. As mean lipid volumes of lipid mixtures can only be measured for tieline endpoint samples, $V_L(T)$ for coexisting phases is calculated by the described method.

3. Results and Discussion

3.1. High resolution SAXS and SANS data analysis of homogeneous lipid mixtures containing cholesterol

3.1.1. SDP–GAP analysis for x–ray data only

The new SDP–GAP analysis for multilamellar vesicles was tested on SAXS data of single lipid MLVs consisting of either DPPC (50 °C), POPC (30 °C), SOPC (30 °C) or DOPC (30 °C) at temperatures where all lipid bilayers are in the L_α phase. The x–ray scattering pattern of SOPC bilayers (grey circles) as well as the best fit of the SDP–GAP model (solid black line) and the GAP model (dashed red line) of Pabst et al. [172] to the experimental data are shown in Fig. 3.1A. Experimental data and fits of all other samples can be found in [178]. The scattering profile exhibits three distinct orders of Bragg reflection, while the fourth and fifth order are very weak. This significant decrease in Bragg peak amplitude and the broadening of peaks is due to bending fluctuations that are typical for bilayers in the L_α phase. The SDP–GAP fit (black line) is in good agreement with experimental data ($\chi^2 = 0.78$) and also fits of remaining samples exhibited similar values for χ^2 (see [178]). An analysis without the constraints introduced in section 2.2.4 yielded to even lower χ^2 values but results in nonphysical results.

3. Results and Discussion

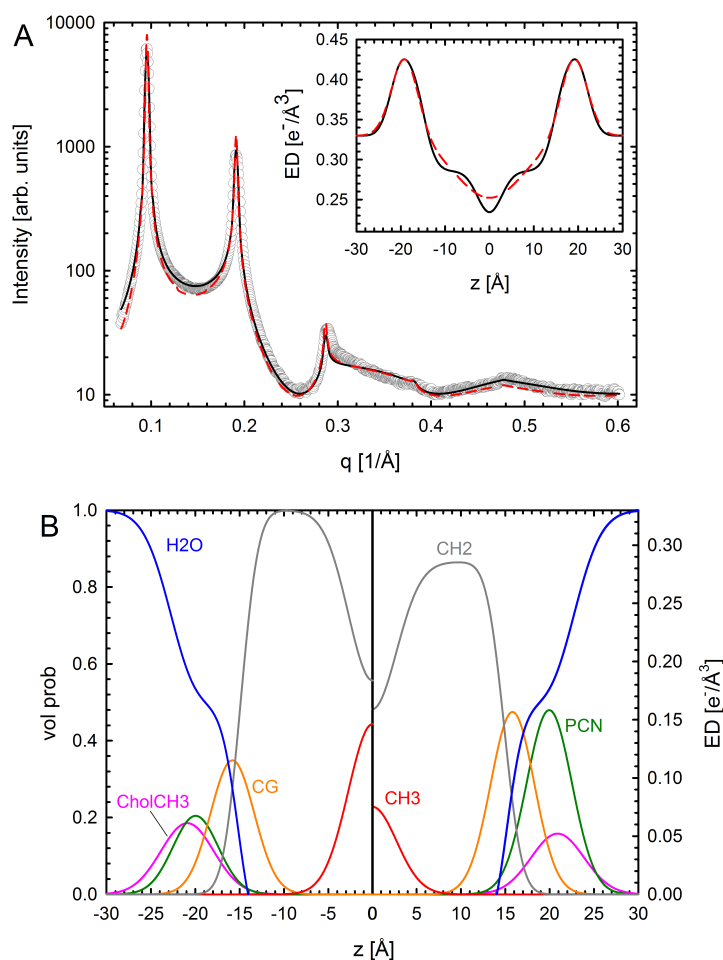


Figure 3.1.: SAXS data analysis of SOPC MLVs at 30 °C. (A) Comparison between best fits of the GAP (dashed red line) and the SDP-GAP model (black line) to the experimental scattering data (grey circles). Resulting electron density profiles of the corresponding models are compared in the inset. (B) Volume probability distribution (left panel) and electron density distribution (right panel) of molecular fragments of the SOPC bilayer. [178]

The best fit using the GAP model (dashed red line in Fig. 3.1A) shows poorer fit statistics ($\chi^2 = 4.78$) in comparison to the SDP-GAP fit (black line) but still describing the experimental data well. The main difference between these two models is the higher structural resolution of bilayer properties that can be obtained from SDP-GAP analysis as it is shown

3.1. SAXS/SANS data analysis of homogeneous lipid mixtures

in the inset of Fig. 3.1A. While the methyl trough and the hydrocarbon chain region are smeared out in the ED profile of the GAP model (dashed red line), these two parts are well resolved in the SDP–GAP model. The structural information about a bilayer that can be obtained from the new analysis is generally higher as shown in Fig. 3.1B where the position of single molecular lipid fragments can be resolved (left panel) and absolute electron density profiles of the bilayer (right panel) can be determined.

Results of the SDP–GAP analysis were compared to literature values from Kučerka and coworkers [173, 187] (SDP analysis for a joint analysis of SAXS/SANS data of ULVs) and to results of the GAP analysis (Tab. 1 in [178]). While structural parameters obtained from SDP–GAP analysis are in good agreement with literature values, the GAP analysis could not reproduce these values exactly. The deviation is mainly due to the simplified GAP model where the ED profile of the bilayer is described by three Gaussians only compared to nine Gaussian and error functions describing the ED profile in the SDP–GAP model. Differences in the Caillé parameter η between the models can be understood in terms of the poorer fit of Bragg peaks using the GAP model.

3.1.2. The effect of cholesterol on saturated and unsaturated PC lipids

Binary mixtures of the same lipid systems (DPPC, POPC, SOPC, DOPC), but containing 20 mol% cholesterol were measured to examine the effect of cholesterol on the bilayer and to test the model for these mixtures. The effect of cholesterol on lipid bilayers is well known and the interactions at the molecular level can be described by the umbrella model [71] that have been already discussed in the introduction (section 1.2.1). Cholesterol increases the bilayer thickness accompanied by a decrease in area per lipid and bilayer fluctuations due to the condensing effect of CHOL (e.g. [190]). Fits of the SDP–GAP model to x–ray scattering patterns of four lipid cholesterol mixtures are shown in [178] together with a table summarizing the results.

3. Results and Discussion

Our results could reproduce the condensing effect exhibiting larger bilayer thickness and smaller area per lipid for binary mixtures in good agreement with previously reported results [65–67, 179, 190]. The increase in d_B is mainly caused by a larger phosphate to phosphate distance but our results do not show a significant increase in hydrocarbon chain length that could be due to the lower scattering contrast in this region. Comparing the effect of cholesterol on different lipids with respect to their degree of unsaturation, a stronger interaction with saturated lipids, like DPPC, was observed. The bilayer thickness increase for example is higher for DPPC/CHOL than for DOPC/CHOL whereby the strongest effect can be seen in the behavior of the bending fluctuations. The addition of cholesterol to DPPC (saturated) reduces the Caillé parameter by a factor of four, for SOPC and POPC (monounsaturated) this effect is smaller exhibiting only a slight decrease in η of $\sim 20\%$ and for DOPC with two monounsaturated chains this effect is absent (see [178]) [66, 204, 205].

3.1.3. Joint analysis of SAXS and SANS data

As already discussed in section 2.2.7, we also obtained SANS data from POPC and POPC- d_{31} MLVs and ULVs, and used it for a simultaneous analysis of SAXS and SANS data to test if the results can be significantly improved with additional information. Figure 3.2A shows neutron scattering profiles of POPC (circles) and POPC- d_{31} (triangles) MLVs with one to two orders of Bragg reflections. The black line represents the best fit of the SDP-GAP model to the SANS data. Compared to the x-ray diffraction pattern shown in the inset, only one poorly resolved Bragg peak is visible in the SANS profile and therefore standalone SANS data is not practical for Bragg peak analysis. Neutron scattering profiles of POPC (circles) and POPC- d_{31} (triangles) ULVs are shown in Fig. 3.2B where the SANS data contains information about the bilayer only because of the absent interbilayer structure in ULVs. The inset represents the NSLD profile of a the POPC bilayer (left panel) and the POPC- d_{31} bilayer (right panel) where the NSLD of the hydrocarbon chains is shifted from negative to positive values. This change in contrast effects the scattering profile of MLVs exhibiting a second Bragg peak (see Fig. 3.2A) and the scattering

3.1. SAXS/SANS data analysis of homogeneous lipid mixtures

profile of ULVs where the first minimum of the intensity is shifted towards lower q -values compared to its protonated equivalent.

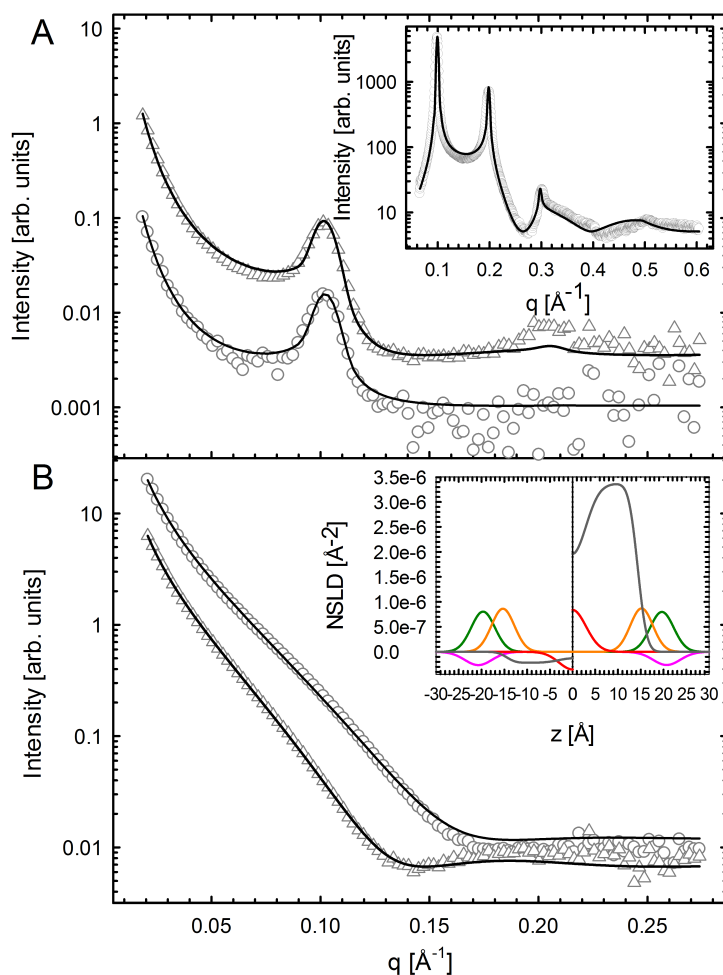


Figure 3.2.: Joint analysis of SAXS and SANS data from POPC uni- and multilamellar vesicles at 30 °C. Experimental SANS data of POPC (grey circles) and POPC-d₃₁ (grey triangles) MLVs and the best fit of the SDP-GAP model (black line) to the experimental data are shown in panel (A). The corresponding SAXS data for the joint analysis are shown in the inset. Panel (B) shows SANS data of corresponding POPC (grey circles) and POPC-d₃₁ (grey triangles) ULVs. NSLD profiles of POPC (left) and POPC-d₃₁ (right) are shown in the inset. [178]

The joint analysis of x-ray and neutron data was applied to several combi-

3. Results and Discussion

nations of SAXS data with one or more SANS data sets: (i) POPC MLVs (ii) POPC-d₃₁ MLVs (iii) POPC and POPC-d₃₁ MLVs (iv) POPC and POPC-d₃₁ ULVs (v) all SANS data sets. Results of the analysis for all combinations are summarized in [178]. Including a single SANS data set in the joint analysis, results in a deviation of structural parameters compared to standalone x-ray analysis and compared to previously reported values [187]. By adding more SANS data, either all MLV data sets, or all ULV data sets, or even all four data sets, the agreement with results of the standalone SAXS data analysis and with literature values could be improved. Results of the latter case showed a slightly better agreement of the hydrocarbon chain and backbone position with literature data whereas the values for bilayer thickness and area per lipid were hardly affected. This can be explained by the higher neutron scattering contrast in the backbone region and therefore the joint analysis is mainly an improvement for the position of the backbone and the hydrocarbon chain length.

3.2. Structural and elastic properties of coexisting L_o/L_d domains in three component lipid mixtures

The second part of this chapter is about the application of our novel global analysis technique for inhomogeneous lipid mixtures exhibiting liquid-liquid phase separation (see section 2.3), thereby using the simplified cholesterol model explained in Eq. 2.16. We studied the ternary mixtures DSPC/DOPC/CHOL and DPPC/DOPC/CHOL at two different cholesterol concentrations and as a function of temperature. An overview of all sample compositions (black circles) is illustrated in Fig. 3.3, where A_{t1} and A_{t2} define the samples containing DSPC with low and high cholesterol concentration respectively. B_{t1} and B_{t2} are defined in the same way for the DPPC/DOPC/CHOL system (exact lipid composition in [202]). Phase diagrams are taken from previous reports from Heberle et al. [96] and Uppamoochikkal et al. [95]

3.2. Properties of coexisting L_o/L_d domains

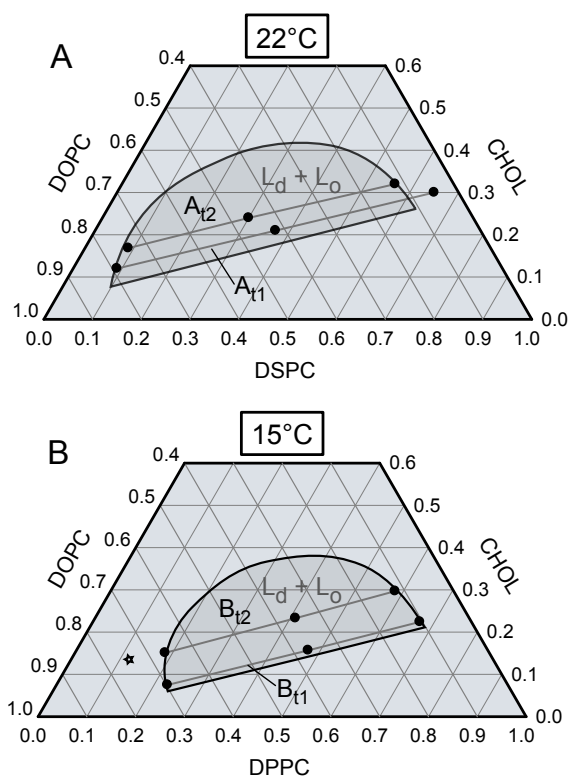


Figure 3.3.: Overview of lipid compositions examined in this work (black circles). Phase diagrams are taken from [96] (DOPC/DSPC/CHOL, (A)) and [95] (DOPC/DPPC/CHOL, (B)). L_d/L_o phase coexistence regions are represented as dark shaded areas with their tielines along which the demixing into L_o/L_d phases occur. Two tielines at a low (A_{11} , B_{11}) and a high (A_{12} , B_{12}) cholesterol concentration including mid- and endpoints were studied. The star in panel (B) accounts for a new tie-line endpoint composition due to SAXS experiments performed in this work. [202]

3.2.1. Global SAXS data analysis for coexisting fluid membrane domains in MLVs

As shown in Fig. 3.3, samples with lipid compositions at tieline midpoints, exhibiting phase separation, as well as their corresponding tieline endpoint samples, exhibiting a single homogeneous phase, were studied. Boundaries for the two phase region are fraught with uncertainty and therefore some of the endpoint samples showed a residual L_o or L_d phase in the L_d

3. Results and Discussion

or L_o endpoint samples. The amount of additional L_o phase that is visible as a second Bragg reflection in the scattering profile, could be subtracted by a fraction the pure L_o phase, because of the same lamellar repeat distance, revealing a correct tieline orientation and sample preparation. The subtraction procedure is explained in more detail in the supplementary material in [202].

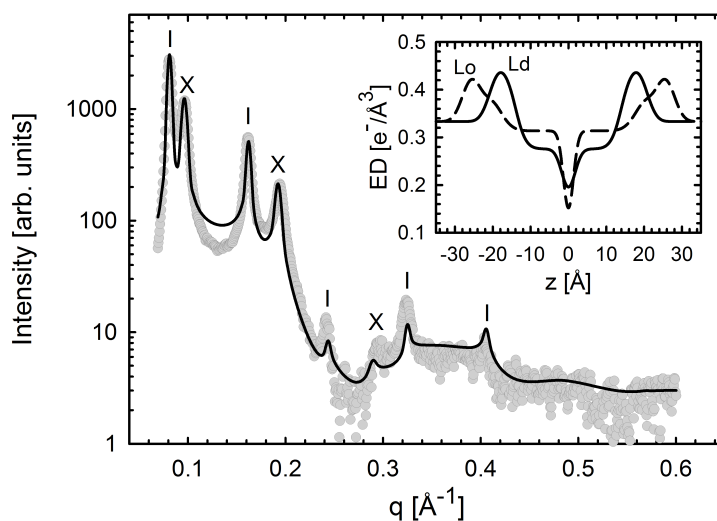


Figure 3.4.: [Global SAXS data analysis for coexisting L_o/L_d domains of tieline midpoint sample A_{t1} at 22 °C. Bragg reflections from aligned L_o (dashes) and L_d (crosses) domains are labelled within the experimental data (grey circles) and the black line shows the best fit of the two phase SDP-GAP model. The inset compares ED profiles of coexisting L_o and L_d phases. [202]

SAXS data of midpoint as well as of endpoint samples were analyzed and we showed that our model is able to capture both scattering patterns of single and coexisting phases. A representative fit (black line) to the experimental data (grey circles) of A_{t1} midpoint sample is shown in Fig. 3.4, and the analysis and fits of all other samples including endpoint data are presented in the supplementary information in [202]. The inset in Fig. 3.4 shows the ED profile of coexisting L_o/L_d phases for A_{t1} where a larger headgroup to headgroup distance for L_o bilayers can be observed as well as an increased absolute ED in the hydrocarbon chain region because of the enriched cholesterol (sterol rings) in the L_o phase.

3.2. Properties of coexisting L_o/L_d domains

Structural and elastic parameters obtained from the analysis of endpoint as well as of midpoint data are summarized in Tables in [202]. The results reveal a good agreement of parameters between coexisting phases and their corresponding single phase endpoints. The differences in bilayer thickness d_B for example are within 1 Å. d_B for the L_d and L_o phase of A_{t1} tieline endpoints is 37.5 Å and 49.7 Å, which is in good agreement with 38.1 Å and 48.6 Å for d_B of coexisting L_d and L_o domains. Although, structural parameters of endpoints and midpoints do not match exactly, because of potentially incorrect phase boundaries and tieline inclinations, possible lateral interactions between domains, or also because of uncertainties in the analysis. Nevertheless, the agreement of endpoint and midpoint results supports the validity of our two phase SDP-GAP analysis. Furthermore, the height difference $\Delta d_B = 10$ Å between coexisting domains could be determined, which is in the same range as previously reported values for DSMs and DRMs [100].

We were also able to monitor the bilayer thinning of L_o domains by exchanging DSPC with DPPC for the $t1$ as well as for the $t2$ tieline, as a further test for our two phase analysis. As DSPC and DPPC are located mainly in the L_o phase, a decrease of $d_B \sim 2-3$ Å of the coexisting L_o domains was found whereas the DOPC rich L_d domains were hardly affected and only a minor decrease of $d_B \sim 0.2-0.6$ Å could be observed. The thickness difference of $\sim 2-3$ Å is in good agreement with those reported for pure DSPC and DPPC bilayers from Kučerka et al. [187] and can be understood in terms of the less number of CH_2 groups in the hydrocarbon chains of DPPC. The bilayer thickness of DOPC enriched L_d domains is also found to be similar to those of pure liquid DOPC bilayers [173].

Another two important parameters are the area per lipid A and bending fluctuations that are represented as the Caillé parameter η . Compared to the L_d phase, L_o domains are more rigid and laterally compressed due to the condensing effect of cholesterol. Previous reports studied this effect for several PC/CHOL mixtures [67, 190, 204, 206], and within this work this effect was also shown for coexisting L_o/L_d domains. Our analysis revealed ~ 20 Å² smaller values for A of L_o domains than for L_d domains ($A \sim 60-65$ Å²), which are similar to previously reported area per lipids

3. Results and Discussion

of single lipid fluid bilayers [173, 187]. The ordering effect also results in a considerable decrease of η from ~ 0.08 for the L_d phase to ~ 0.03 for L_o .

These results show that our two-phase analysis is able to simultaneously analyze structural and elastic properties of coexisting fluid domains in situ at high resolution. L_o/L_d domains can now be studied as a function of composition and temperature to gain insight into the physics of raft like domains and how they are influenced by various cholesterol concentrations as well as temperature.

3.2.2. Cholesterol affects intra- and interbilayer structure of L_o/L_d membrane domains

Structural properties of $t2$ tieline midpoint samples (higher cholesterol concentration) were compared to properties of $t1$ midpoints to examine the influence of cholesterol on the bilayer. The lamellar repeat distance d increased slightly for system A_t and B_t ($\Delta d \sim 0.75 \text{ \AA}$), whereas both systems exhibited a significantly smaller d value ($\Delta d \sim 2 \text{ \AA}$) for L_o domains at higher cholesterol concentrations (see [202]). The increase of d for the L_d phase is mainly caused by bilayer thickening that can be explained by the ordering effect of cholesterol. However, the decrease of d_B for the L_o phase accounts only for one third of the total decrease of d and hence the decrease of the interbilayer water layer thickness ($\Delta d_W \sim 0.8\text{--}1.8$) is the main contribution to Δd . A decrease in d_B of L_o domains upon the addition of cholesterol seem counterintuitive because of the cholesterol's condensing effect but a change in lipid composition (reduction of high melting lipids) may overcompensate this effect. Another parameter, the bilayer fluctuations are hardly influenced by higher cholesterol concentrations and stay rather constant. Hence the decrease in d_W for the L_o phase cannot be induced by raised bending rigidities but is maybe caused by reduced hydration forces and/or increased van der Waals forces.

The results further on show that while the area per lipid for $t2$ L_d domains is smaller due to the condensing effect of cholesterol, A for L_o domains show only insignificant changes within experimental uncertainties ($< 2\%$) for all samples. As the area per lipid of L_o phases is hardly influenced

3.2. Properties of coexisting L_o/L_d domains

by various cholesterol concentrations and lipid compositions, $A \sim 43.6 \text{ \AA}$ may represent the tightest packing of lipid molecules in the liquid ordered phase.

3.2.3. The influence of temperature on coexisting L_o/L_d domains

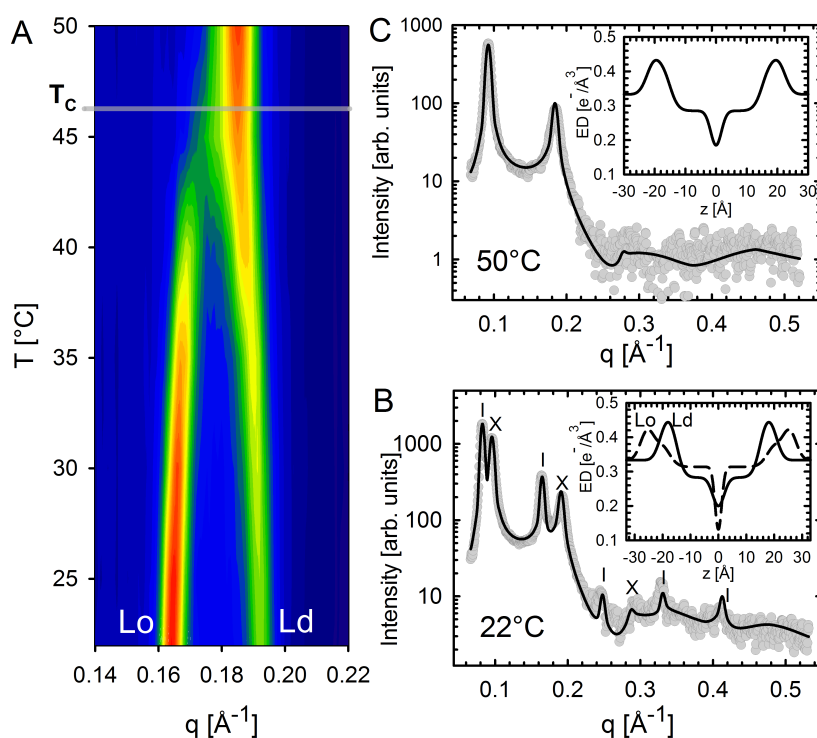


Figure 3.5.: Temperature behavior of A_{t2} midpoint sample. Panel (A) shows a contour plot of the second order Bragg reflections from L_o and L_d domains with a critical temperature T_C between 45°C and 50°C . Temperature frames were taken every 5°C and the smooth appearance of data is due to interpolation. Panel (A) and (B) show experimental SAXS data (grey circles) and best fits (black line) to the data at 22°C and 50°C respectively. Resulting ED profiles for coexisting L_o/L_d phases and the homogeneous liquid phase are depicted in the insets. [202]

Midpoint samples were also measured as a function of temperature in steps of 5°C upon the transition to the homogeneous phase. Figure 3.5A

3. Results and Discussion

shows the second order Bragg reflection of L_o and L_d phase for A_{t2} and the transition at the critical temperature T_C to a homogeneous L_d phase exhibiting only one Bragg reflection. Because of the low temperature resolution, T_C could not be determined accurately, but for DSPC/DOPC/CHOL T_C was found to be between 45 and 50 °C and for DPPC/DOPC/CHOL between 30 and 35 °C. Scattering intensities for phase separated L_o/L_d domains and for the homogeneous L_d phase are represented in Fig. 3.5B and C.

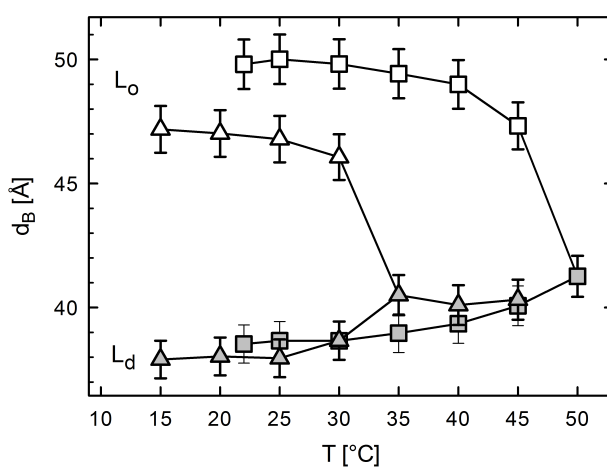


Figure 3.6.: Bilayer thickness d_B as a function of temperature for tieline midpoint samples A_{t1} (squares) and B_{t1} (triangles). L_o and L_d phases are represented with open and solid symbols respectively. [202]

The bilayer thickness d_B of coexisting L_o/L_d domains of A_{t1} and B_{t1} are compared in Fig. 3.6. As the behavior of $t1$ and $t2$ tieline samples is similar, the discussion is limited to $t1$ tielines only. Below T_C a monotonic increase in d_B of L_d domains can be observed and d_B of L_o domains decrease monotonously in the range of 1–2 Å. In the vicinity of T_C the bilayer thickness of L_o domains decreases abruptly, whereas d_B of L_d domains exhibits similar values just below and above T_C , indicating rather stable L_o domains through a wide range of temperatures with an abrupt melting close to T_C . Interestingly, both mixtures show similar bilayer thicknesses of ~ 41 Å in the homogeneous L_d phase (mainly DOPC), despite the difference in lipid chain length of DPPC and DSPC.

3.2. Properties of coexisting L_o/L_d domains

An interesting feature in Fig. 3.6 is the increase in d_B of L_d domains with temperature that is in contradiction to the behavior of single lipid fluid bilayers, which show a decrease of d_B with increasing temperature [187, 207, 208]. This can be understood by a potential diffusion of cholesterol from L_o to L_d domains, which is supported by recently published NMR data of Davis and Schmidt [126], where they suggest a decrease of cholesterol fraction in L_o domains. This would consequently lead to an enrichment of cholesterol in L_d domains and hence to an increase in bilayer thickness due to the ordering effect of cholesterol.

Another parameter that describes the melting of L_o domains is c_{Ld} , which increases as T_C is approached resulting in a decrease of L_o phase fraction ($1 - c_{Ld}$) (see [178]). The increase of L_d phase fraction defined as c_{Ld} also indicates an asymmetric behavior of phase boundaries as a function of temperature, where the L_d endpoints approach the corresponding midpoints faster than the L_o endpoints that is shown in Fig. 2.16. This is in agreement with previously reported temperature dependent phase diagrams from Buboltz et al. [203]. The increase of c_{Ld} with temperature was quantified and for DOPC/DSPC/CHOL $\Delta c_{Ld} = 16\%$ for $t1$ tieline and for $t2$ $\Delta c_{Ld} = 25\%$. This effect is less pronounced for DOPC/DPPC/CHOL, with $\Delta c_{Ld} = 9\%$ for the $t1$ and $\Delta c_{Ld} = 16\%$ for the $t2$ tieline. The results show a stronger increase in L_d phase fraction at higher cholesterol concentrations for both lipid mixtures indicating that cholesterol may promote melting of L_o domains. This effect can be explained by taking into account line tension γ that facilitates domain melting by lowering the value of γ . As $\gamma \propto \Delta d_B^2$ [209] domain melting can be also understood in terms of domain height mismatch. Our results show a decrease of Δd_B with higher cholesterol concentrations for both mixtures and hence a decrease of line tension between the domains that facilitates domain melting.

The parameter $\Delta d_B(T)$ can also be used for an analysis in terms of the Ising model where any order parameter such as $\Delta d_B(T)$ can be described by $(T_C - T)^\beta$. β is the critical exponent defining the behavior of a system whether following a two dimensional ($\beta = 0.125$) or a three dimensional ($\beta = 0.325$) Ising model. While fluorescence microscopy experiments [30, 123, 124] support a two dimensional Ising model behavior of L_o/L_d domains, recent atomic force microscopy measurements of Δd_B [125] and first momenta of NMR spectra [126] suggest a three dimensional

3. Results and Discussion

Ising model behavior. We analyzed Δd_B as a function of temperature and determined critical exponents for all systems. The results favor a two dimensional Ising model (see supplementary information in [202]), but due to the low temperature resolution and the high uncertainty in T_C we cannot make a firm statement. Nevertheless our label free analysis for coexisting liquid domains should be an appropriate method to address the issue whether L_o/L_d domains behave like a two- or a three dimensional Ising model.

3.3. Influence of domain size on coexisting L_o/L_d domains in complex lipid mixtures

3.3.1. Lipid composition and x-ray scattering profiles

Adding another lipid component to the system leads to the four component mixture POPC/DOPC/DSPC/CHOL that is described in detail in section 1.2.6. The exchange of POPC by DOPC that is quantified by the parameter ρ_{DOPC} (Eq. 1.1) results in an increase of L_d domain size within a L_o matrix. In this work six different lipid compositions along a ρ_{DOPC} trajectory were studied including midpoint and endpoint samples for each ρ_{DOPC} -value. Exact lipid composition of all samples are listed in Tab. 3.1 and are taken from Heberle et al. [1]. Deviations in composition from reported values in [1] are due to new L_o endpoint data from Heberle and coworkers.

Samples are classified into nano and macro domains with respect to their domain size and ρ_{DOPC} -values. Samples at $\rho_{DOPC} = 0\%$, 10% and 20% belong to the nano domain regime where no stacking of L_o/L_d domains was observed. Whereas samples at $\rho_{DOPC} = 35\%$, 66% and 100% belong to the macro domain regime, showing an alignment of domains across bilayers in MLVs. X-ray scattering patterns from MLVs exhibiting phase separation and domain stacking were analyzed using the model for phase coexistence described in section 2.3.2 and samples

3.3. Influence of domain size on L_o/L_d domains

Table 3.1.: Overview of lipid compositions (molar fractions) studied in this work according to the published compositional phase diagram DOPC/POPC/DSPC/CHOL [1]. L_o/L_d midpoint compositions as well as corresponding L_o, L_d endpoints for each ρ_{DOPC} value were studied.

ρ		DSPC	POPC	DOPC	CHOL
0 %	L_d	0.09	0.79	0.0	0.12
	L_o	0.55	0.18	0.0	0.27
	L_d/L_o	0.32	0.49	0.0	0.20
10 %	L_d	0.09	0.71	0.08	0.12
	L_o	0.58	0.13	0.01	0.28
	L_d/L_o	0.34	0.42	0.05	0.20
20 %	L_d	0.09	0.63	0.16	0.12
	L_o	0.60	0.09	0.02	0.28
	L_d/L_o	0.35	0.36	0.09	0.20
35 %	L_d	0.09	0.51	0.28	0.12
	L_o	0.62	0.06	0.03	0.29
	L_d/L_o	0.36	0.29	0.16	0.21
66 %	L_d	0.09	0.27	0.52	0.12
	L_o	0.64	0.02	0.04	0.3
	L_d/L_o	0.37	0.15	0.28	0.21
100 %	L_d	0.09	0.0	0.79	0.12
	L_o	0.65	0.0	0.05	0.3
	L_d/L_o	0.37	0.0	0.42	0.21

exhibiting phase separated nano domains, which do not align across bilayers, were analyzed using the model described in section 2.3.3.

Figure 3.7 shows scattering profiles of samples at $\rho_{DOPC} = 0\%$ (panel A) and $\rho_{DOPC} = 35\%$ (panel B), exhibiting L_o/L_d phase coexistence and the best fit of the model intensity (black line) to the experimental data (grey circles). At $\rho_{DOPC} = 0\%$ the domains are too small to align on top of each other and hence only one Bragg reflection, resulting from the lamellarity of predominantly L_o phase bilayers with small L_d domain impurities, could be observed. The abrupt drop in Bragg peak amplitude at the fourth order and the extensive broad lobe between $q = 0.32$ and 0.45 \AA^{-1} , resulting from contributions of L_o and L_d FFs, are two main characteristics of x-ray

3. Results and Discussion

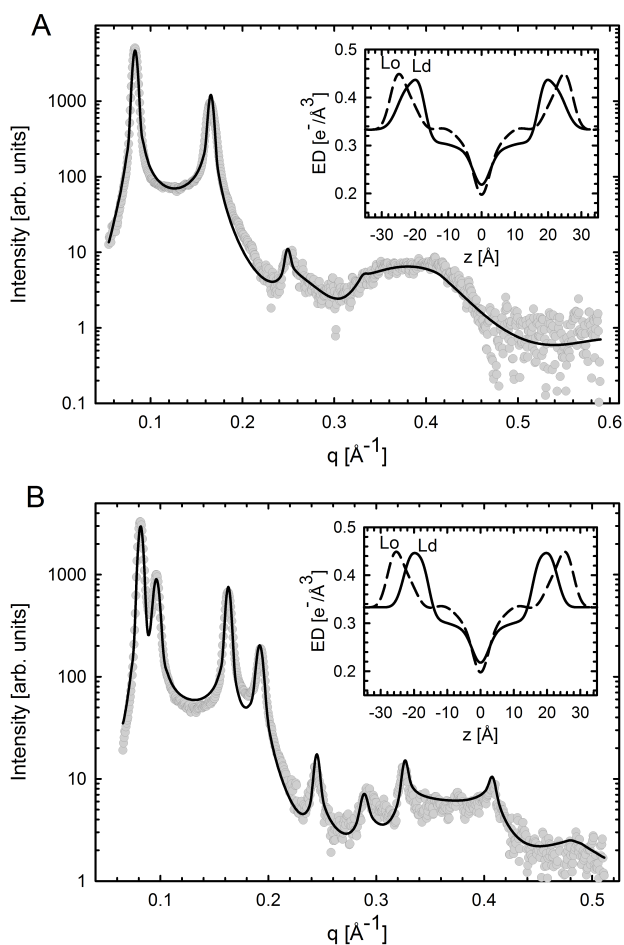


Figure 3.7.: Global SAXS data analysis of coexisting liquid nano (A) and macro (B) domains at 20 °C. Panel (A) and (B) show SAXS data (grey circles) of midpoint samples at $\rho_{DOPC} = 0\%$ and 35% respectively. Black lines represent the best model fit and the insets show the obtained ED profiles of the coexisting L_0/L_d phases.

scattering profiles of non-aligned nano domains that disappear upon the transition to a homogeneous phase, where domains melt (see section 3.3.6). Insets in Fig. 3.7 represent the ED profiles of coexisting L_0/L_d phases with their typical bilayer characteristics, the larger head group to head group distance for L_0 domains and the higher electron density in the hydrocarbon chain region of the cholesterol enriched L_0 phase. Larger domains at $\rho_{DOPC} = 35\%$ show an alignment of domains that can be

3.3. Influence of domain size on L_o/L_d domains

observed as two different Bragg reflections in the scattering profile in Fig. 3.7B. Also scattering profiles of L_o and L_d tieline endpoint samples were analyzed and compared to midpoint data. For the modeling of cholesterol Eq. 2.17 was used to describe cholesterol's head and tail by two distinct Gaussian functions, which is a further development of our model giving better fit statistics and results.

3.3.2. Coexisting liquid domains behave differently than their corresponding pure L_o and L_d phases

In this work tieline midpoint samples as well as their corresponding endpoint samples were studied and compared for consistency. Firstly we compared the lamellar repeat distance between end- and midpoints as a function of ρ_{DOPC} as shown in Fig. 3.8. In the nano domain regime only one d -spacing for the coexisting liquid phases was observed, because of the non-alignment of L_o/L_d domains. This d -value is similar to the lamellar repeat distance of the pure L_o phase due to the predominantly L_o phase in the bilayer of coexisting L_o/L_d domains. Further on, d of the midpoint samples decrease as the domains are getting larger ($\rho_{DOPC} = 0\%$, 10% , 20%) until the domains start aligning and split up into two different d -spacings. The lamellar repeat distances in the macro domain regime of endpoint and midpoint samples do not agree for the L_o phase, exhibiting a difference of $1\text{--}2 \text{ \AA}$, but are roughly in the same range for the L_d phase ($d \sim 64\text{--}66 \text{ \AA}$). Also the behavior as a function of ρ_{DOPC} is different between end- and midpoint samples. While d of the pure L_d phase decreases as a function of domain size, d of the coexisting L_d phase stays nearly constant. The variations in d between end- and midpoints cannot be completely attributed to differences in bilayer thickness (Fig. 3.9) but may be a combination of bilayer thickness variations and interbilayer interactions.

The differences between endpoint and midpoint samples could be due to uncertainties in tieline inclination and phase boundaries or due to uncertainties in the preparation of samples (lipid composition). L_d endpoint samples at $\rho_{DOPC} = 66\%$ and 100% for example showed a few percent of

3. Results and Discussion

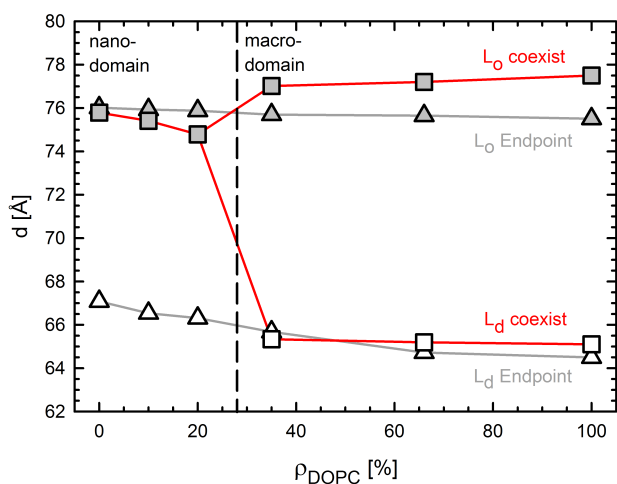


Figure 3.8.: Comparison of lamellar repeat distance d between endpoints (triangles) and midpoints (squares) as a function of ρ_{DOPC} . The L_d and L_o phase are represented by open and solid symbols respectively. Data points are connected with grey (endpoints) and red (midpoint) lines to guide the eye.

residual L_o phase, meaning that phase boundaries and/or lipid compositions are not correct. The subtraction of residual L_o phase is described in the supplementary information in [202]. Further on, the differences could be explained by lateral interactions between coexisting domains, or they are a result of a combination of all these issues. Therefore a comparison between end- and midpoints is possible and also meaningful but all mentioned aspects have to be taken into account in the interpretation of results.

To exclude possibly wrong results received from the analysis that could generate these differences, scattering data of midpoint samples were fitted based on fixed form factors that are obtained from the appropriate endpoint samples. χ^2 values were by a factor of 1.5–2.0 higher compared to fit results using the two phase analysis. Only the sample at $\rho_{DOPC} = 35\%$ showed similar χ^2 values and this agreement could be also seen in similar bilayer thicknesses of end- and midpoints (Fig. 3.9). Moreover, this L_d endpoint sample did not exhibit any residual L_o phase and hence endpoint lipid compositions of this tieline could be correct.

3.3.3. Structural bilayer properties as a function of domain size

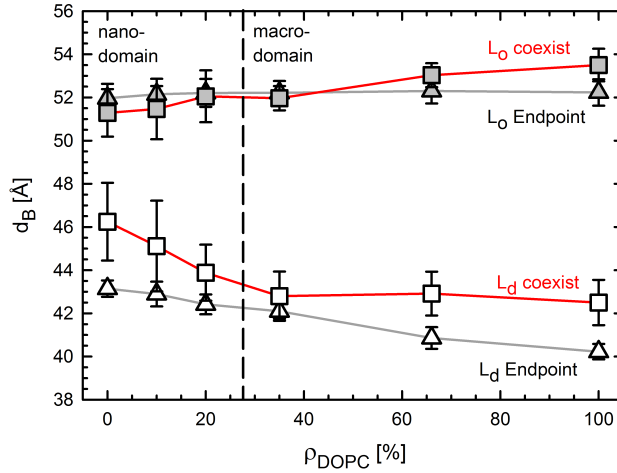


Figure 3.9.: Comparison of bilayer thickness d_B between endpoints (triangles) and midpoints (squares) as a function of ρ_{DOPC} . The L_d and L_o phase are represented by open and solid symbols respectively. Data points are connected with grey (endpoints) and red (midpoint) lines to guide the eye.

The bilayer thickness of endpoint and midpoint samples reveal differences in absolute values but also in the behavior of d_B as a function of ρ_{DOPC} (Fig. 3.9). The bilayer thickness of endpoints show the same trend as a function of domain radius like the bilayer thickness measured by Heberle et al. [1]. While d_B of the L_o endpoints stays constant, d_B of coexisting L_o domains is slightly increasing as the amount of L_o phase is decreasing (see Fig. 3.13 and [1]). Hence, not only the L_d domain size is increasing as a function of ρ_{DOPC} but also the overall L_d phase fraction. On the other hand d_B of L_d endpoints show a linear decrease, whereas the bilayer thickness of coexisting L_d domains show a steep linear decrease in the nano-domain regime but stay rather constant in the macro-domain regime. The differentiation in nano and macro domains is mainly with respect to the domain size but also structural parameters of coexisting L_o/L_d domains such as d_B show a different behavior between the two regimes.

The linear decrease of d_B for L_d endpoint samples cannot be explained by the simple exchange of POPC by DOPC because of their equal bilayer

3. Results and Discussion

thickness in the fluid phase ([178, 187]), but could be understood by taking into account the interaction with cholesterol. While the effect of cholesterol on the bilayer thickness of the double unsaturated chain lipid DOPC is negligible, the interaction of cholesterol with the mono unsaturated lipid POPC is stronger resulting in a significant bilayer thickening due to the condensing effect [178]. The bilayer thickness of coexisting L_d domains behaves differently and therefore we conclude that not only the exchange of POPC by DOPC affects d_B but also the domain size and the L_o environment may have a strong impact on d_B of coexisting domains.

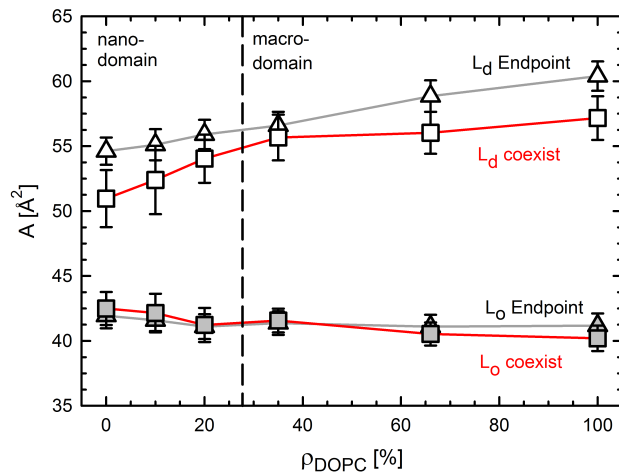


Figure 3.10.: Comparison of lateral area per lipid A between endpoints (triangles) and midpoints (squares) as a function of ρ_{DOPC} . The L_d and L_o phase are represented by open and solid symbols respectively. Data points are connected with grey (endpoints) and red (midpoint) lines to guide the eye.

The steep increase in d_B of coexisting L_d domains starting at $\rho_{DOPC} = 35\%$ to 0% could be understood as a "squeezing" effect. This means that when the domains get smaller the L_o surrounding squeezes the small domains resulting in a thickening of the bilayer (Fig. 3.9). Also the area per lipid A of nanoscopic L_d domains decrease strongly when domains get smaller, supporting this hypothesis (Fig. 3.10). This could also be the reason for the generally smaller values of A for coexisting L_d domains, because they are squeezed compared to their pure L_d phase endpoint samples. Another explanation for the nanoscopic domain thickening could be the contribution of potentially thicker L_d domain boundaries, which

3.3. Influence of domain size on L_o/L_d domains

are supposed to be highly curved in close vicinity to the L_o surrounding [210], to the x-ray diffraction pattern resulting in a mean value for d_B that is between that of the inner part of the domain and the thicker boundaries. To address these issues in more detail further experiments and maybe MD-simulations have to be done. In the macroscopic regime d_B stays nearly constant and also the area per lipid shows only a slight increase as a function of domain size (Figs. 3.9, 3.10). This could be due to the stability of large domains, meaning that the L_d domains are too large to be squeezed.

d_B of coexisting L_o domains show a slight increase as a function of ρ_{DOPC} . As an increase of ρ_{DOPC} is accompanied by a decrease in L_o phase fraction (Fig. 3.13), a similar explanation as for the L_d domains could be considered. The bilayer thickness of L_o domains increases and the area per lipid decreases when the L_o phase fraction decreases because of the before mentioned squeezing effect of the L_d phase on the L_o phase.

3.3.4. Correlation between domain size and domain height mismatch

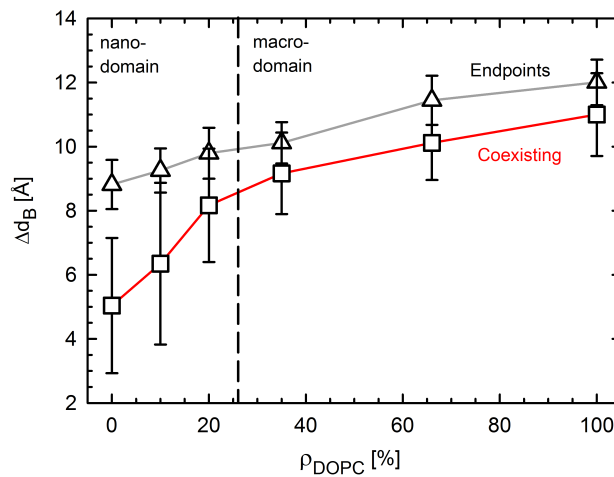


Figure 3.11.: Comparison of L_o/L_d domain height mismatch Δd_B between endpoints (triangles) and midpoints (squares) as a function of ρ_{DOPC} . Data points are connected with grey (endpoints) and red (midpoint) lines to guide the eye.

3. Results and Discussion

Figure 3.11 compares the height difference Δd_B of bilayer thicknesses between L_o - L_d endpoint samples and coexisting L_o/L_d domains. The bilayer thicknesses between macroscopic coexisting L_o/L_d domains are in the same range (~ 8 – 11 Å) as previously reported values for the height difference between L_o and L_d domains [100, 202, 211], whereas Δd_B for the nano domains is significantly smaller between 5 and 8 Å. While Δd_B between L_o - L_d endpoints show a linear correlation between height mismatch and ρ_{DOPC} as it is also reported in [1], the height mismatch between coexisting L_o/L_d domains behave differently. The relative increase in Δd_B for the coexisting domains in the macro regime is 0.028 ± 0.0014 Å/% and compares well with endpoint data, where the increase is 0.032 ± 0.0027 Å/%. In the nano domain regime the increase in Δd_B is also linear but about five times steeper (0.156 ± 0.0148 Å/%) than for the macro regime or for the endpoints. Again this difference between the nano and macro domain regime can also be observed for the height mismatch between L_o/L_d domains as it was already discussed in the previous paragraph.

Heberle et al.[1] reported that domain height mismatch plays also a role in domain coalescence, whereas domain coalescence in general has not been fully understood yet. There are still open questions like what is or are the driving forces for coalescence. One force could be line tension that increases as a function of ρ_{DOPC} thereby pushing domain coalescence to reduce boundary energy between L_o/L_d domains. The increase in line tension can be explained by the theoretically predicted quadratic dependence on the L_o/L_d domain height mismatch [209], which was measured in this work. But line tension cannot be the only driving force for domain coalescence, because then every system of coexisting L_o/L_d domains would exhibit one single round domain in the equilibrium state [209]. We showed that the domain height mismatch and hence line tension is very low for the nano domain regime because of the non-linear behavior of Δd_B supporting small domains. Nevertheless, there has to be a competing energetic term such as entropy [109], long-range repulsive interactions from lipid dipole moments [212] or curvature effects [213–216] that favors the breakup of domains.

3.3.5. Bending fluctuations and the increase in L_d phase fraction

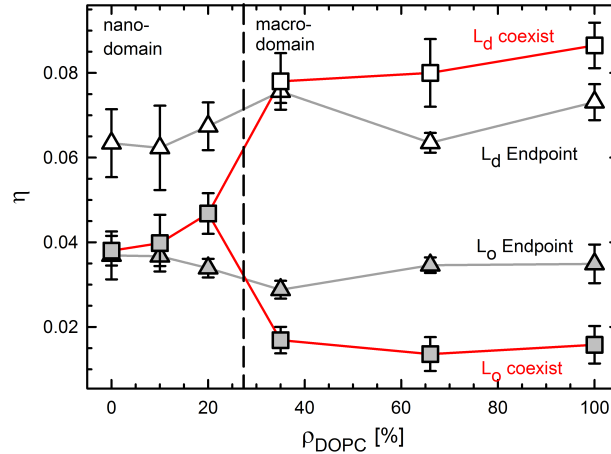


Figure 3.12.: Comparison of bending fluctuations η between endpoints (triangles) and midpoints (squares) as a function of ρ_{DOPC} . The L_d and L_o phase are represented by open and solid symbols respectively. Data points are connected with grey (endpoints) and red (midpoint) lines to guide the eye.

The Caillé parameter η of endpoint and midpoint samples that describes bending fluctuations of a bilayer is shown in Fig. 3.12. Due to less order in the L_d phase, the L_d endpoint samples show higher bending fluctuations ($\eta \sim 0.06-0.08$) than the more ordered L_o endpoints ($\eta \sim 0.03-0.04$). In the nano regime there is only one value for the coexisting sample, because of the non-alignment of domains resulting in a single Bragg reflection that is used for the analysis. $\eta = 0.038$ for the coexisting sample at $\rho_{DOPC} = 0\%$ that agrees with η of the corresponding L_o endpoint. This is due to the predominantly L_o phase in the L_d/L_o bilayer that contributes most to the bilayer fluctuations. The increase of the L_d domain size at $\rho_{DOPC} = 10$ and 20% causes an increase of L_d impurities (domains) in the L_o matrix that leads to an increase of η because of fluctuations of the less ordered L_d domains. Further, our analysis could resolve differences in bending fluctuations between L_o and L_d domains in the macro domain regime when domains are aligned. We determined fourfold higher fluctuations ($\eta \sim 0.08$) for L_d domains than for L_o domains ($\eta \sim 0.02$) as it is shown in

3. Results and Discussion

Fig. 3.12.

Another interesting finding are the significantly lower bending fluctuations of coexisting L_o domains ($\eta \sim 0.015\text{--}0.02$) compared to the pure L_o bilayer of endpoint samples ($\eta \sim 0.03\text{--}0.035$) in the macro regime (Fig. 3.12). This could be due to the smaller area of coexisting L_o phases compared to a pure L_o phase in a sample. While the pure L_o phase can oscillate freely, coexisting L_o phases are restricted to smaller areas by the boundaries to their adjacent L_d domains, where they cannot oscillate completely freely anymore. A similar effect could not be observed for the L_d phase (right upper part of Fig. 3.12). η of the L_d endpoints at $\rho_{DOPC} = 35\%$, 66% and 100% do not follow a certain trend but show even less fluctuations compared to the coexisting L_d domains that could be caused by interactions of the predominantly L_d phase with a residual L_o phase in the "theoretically" pure L_d endpoint samples. The increase of η for coexisting L_d domains in the macro regime is not significant and vary only within uncertainties, but nevertheless this increase can be a result of the exchange of POPC by DOPC, which shows higher fluctuations in pure lipid bilayers as well as in binary mixtures containing cholesterol [178].

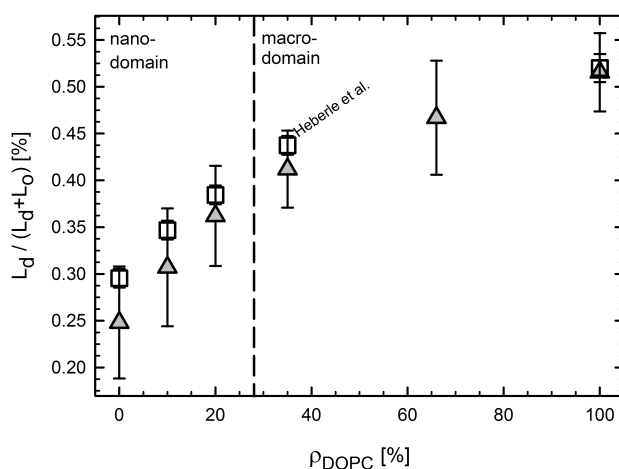


Figure 3.13.: L_d phase fraction of coexisting phases as a function of ρ_{DOPC} . L_d phase fractions obtained in this work (grey triangles) are compared to calculated L_d phase fractions from Heberle et al. [1] (open squares)

Figure 3.13 shows a comparison of L_d phase fractions between data of

3.3. Influence of domain size on L_o/L_d domains

Heberle et al. [1] (open squares) and data obtained in this work (grey triangles). Although L_d phase fractions are determined from different systems (ULVs and MLVs) and with different experimental methods (SAXS and SANS) they are in good agreement within uncertainties and show the same behavior as a function of domain size, whereby the exact lipid compositions are slightly different (compare Tab. 3.1 and [1]). This increase is mainly assigned to a shift of the tieline midpoint towards the L_d endpoint as a function of ρ_{DOPC} due to variations in lipid composition [1]. Whereas, within this work we tried to correct for this shift of midpoint compositions by choosing compositions that are in the middle of the tieline, but we could still observe this increase in L_d phase fraction (Fig. 3.13). Therefore we suggest that the exchange of POPC by DOPC and the domain height mismatch do not drive domain coalescence only but also increase the overall L_d phase fraction. To test and confirm these considerations further experiments have to be done.

3.3.6. Temperature dependent behavior of L_o/L_d domains and their influence on the critical temperature

Midpoint samples at $\rho_{DOPC} = 35\%$, 66% and 100% exhibiting domain alignment were also measured as a function of temperature between 20°C and 50°C upon the transition to a homogeneous phase with temperature steps of 5°C . As these steps are large, the transition temperature T_C could not be determined exactly but variations in T_C with respect to the domain size could be observed. For $\rho = 35\%$ T_C is between 30°C and 35°C , and for $\rho = 66\%$ and 100% T_C is between 45°C and 50°C as it is shown in Fig. 3.14, where the bilayer thickness of coexisting L_o/L_d domains as a function of temperature is plotted. In this work T_C was determined as the temperature, where domains do not show alignment anymore that is indicated by one single Bragg reflection in the scattering pattern (see Fig. 3.5). Therefore T_C does not necessarily represent the real transition temperature where all the domains melt and form one homogeneous phase but especially for larger domains at $\rho_{DOPC} = 66\%$ and 100% T_C should account for the domain melting temperature. This can be justified by comparing the scattering profiles of midpoint samples of $\rho_{DOPC} =$

3. Results and Discussion

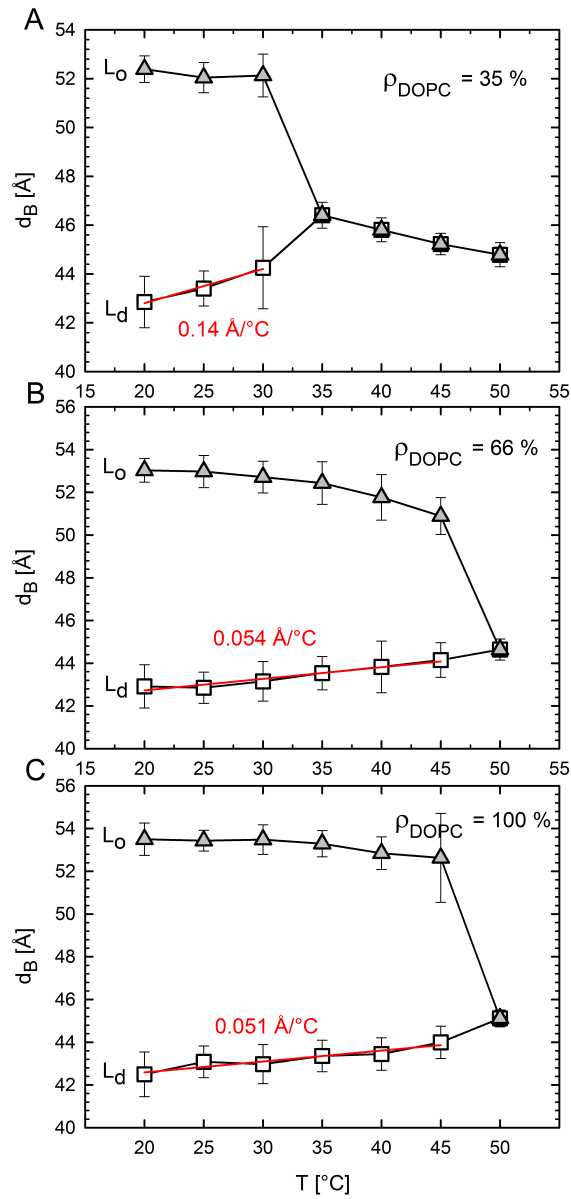


Figure 3.14.: Temperature dependent bilayer thickness d_B of coexisting L_o (grey triangles) and L_d (open squares) domains. d_B as a function of temperature upon the transition to a homogeneous phase is plotted for $\rho_{DOPC} = 35\%$ (A), 66% (B) and 100% (C). The red line represents a linear regression to the L_d bilayer thickness with its slope.

3.3. Influence of domain size on L_o/L_d domains

66 % and 100 % at 50 °C and of $\rho_{DOPC} = 35$ % at 35 °C. While the samples of $\rho_{DOPC} = 66$ % and 100 % show a typical homogeneous L_d phase like scattering pattern as shown in Fig. 3.5C, the sample of $\rho_{DOPC} = 35$ % exhibits a scattering pattern similar to that of non-aligned domains as shown in Fig. 3.7A, meaning that there could be still a contribution of non-melted domains. At 45–50 °C the scattering profile of $\rho_{DOPC} = 35$ % again looks like a homogeneous L_d phase pattern.

Figure 3.14 shows the bilayer thickness of coexisting L_o/L_d domains at $\rho = 35$ %, 66 % and 100 % as a function of temperature. d_B of L_o domains decrease monotonically with temperature of about 0.5–1.5 °C and show a sharp drop close to T_C . On the other hand d_B of L_d domains increases as a function of temperature that can be explained by the potential diffusion of cholesterol from the L_o to the L_d phase as it was already discussed in section 3.2.3 and [126]. In the homogeneous phase the bilayer thickness decreases further (Fig. 3.14A) as it is for single lipid systems [187]. The increase of d_B for L_d domains was further quantified by a linear regression to the bilayer thickness as a function of temperature (red line in Figs. 3.14A,B,C). For $\rho = 35$ % the increase is 0.14 ± 0.017 Å/°C, for $\rho = 66$ % it is 0.054 ± 0.007 Å/°C and for $\rho = 100$ % it is 0.051 ± 0.008 Å/°C. These results show that the increase of d_B declines with ρ_{DOPC} and hence the increase in domain size seems to stabilize the L_d domains.

The water layer thickness d_W between aligned L_o and L_d domains as a function of temperature was also calculated and the results are shown in Fig. 3.15. d_W is generally larger between L_o domains meaning that the net interaction forces between bilayers are more repulsive in the case of L_o bilayers than for L_d bilayers. Larger water layer thicknesses between L_o domains are counterintuitive, as the L_o bilayer is already thicker than the L_d bilayer and together with the thicker water layer between L_o domains the boundaries between adjacent L_o/L_d phases are even more stressed and hence energetic unfavorable. Close to T_C d_W of L_o domains drops abruptly of about 2–3 Å and becomes smaller than d_W of L_d domains. So the interaction forces between bilayers seem to change tremendously close to T_C . This effect cannot be assigned to an increase in bending rigidity, because the fluctuations (η) even increased twofold close to T_C (data not shown) but it may be attributed to an increase of van der Waals forces and/or a decrease of hydration forces.

3. Results and Discussion

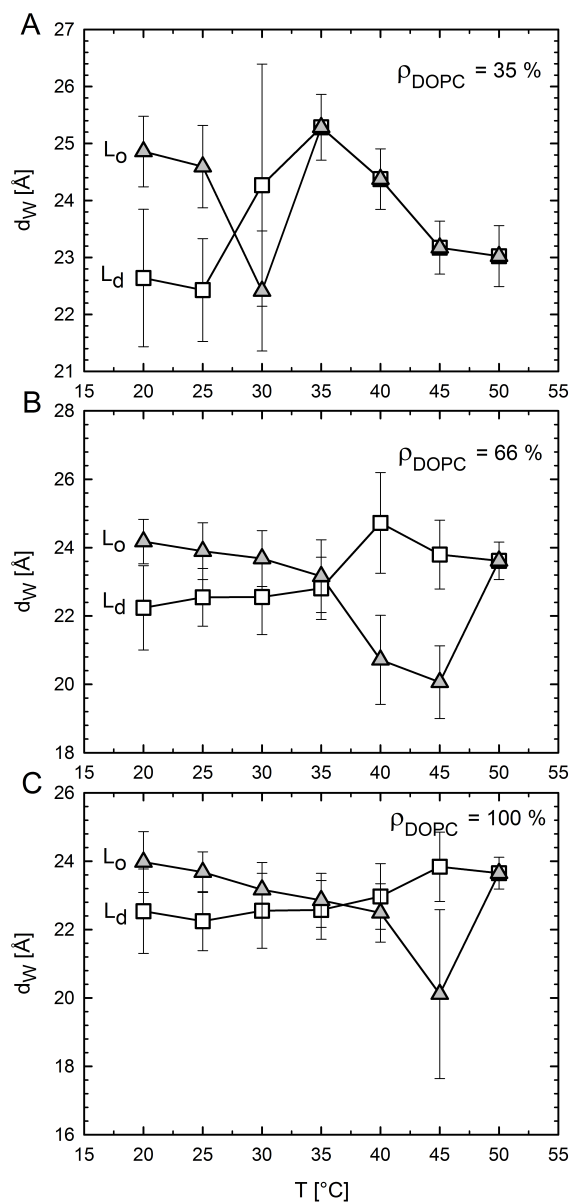


Figure 3.15.: Temperature dependent water layer thickness d_W between L_o (grey triangles) and L_d (open squares) domains. d_W as a function of temperature upon the transition to a homogeneous phase is plotted for $\rho_{DOPC} = 35\%$ (A), 66% (B) and 100% (C).

3.3. Influence of domain size on L_o/L_d domains

Table 3.2.: Dependence of the critical exponent β on T_C . To evaluate the influence of T_C on β , T_C was varied between the extremes of the experimental temperature interval.

Sample	T_C	β
$\rho = 66\%$	46.0	0.13
$\rho = 66\%$	47.5	0.18
$\rho = 66\%$	49.0	0.21
$\rho = 100\%$	46.0	0.08
$\rho = 100\%$	47.5	0.10
$\rho = 100\%$	49.0	0.11

Like in section 3.2.3, the height difference between L_o and L_d domains as a function of temperature for samples at $\rho = 66\%$ and 100% that show phase separation, were determined and analyzed with respect to the Ising model to obtain the critical exponent β describing either a 2D ($\beta = 0.125$) or a 3D ($\beta = 0.325$) Ising model [30, 123–126]. Despite the fact that the temperature steps of 5°C in our measurements are rough and hence T_C could not be determined precisely, our results for the critical exponent β suggest a 2D Ising model behavior. Table 3.2 shows results of β for each domain size and various values of T_C . To test the dependency of the critical exponent on T_C , β was determined for three different values of T_C . One value was chosen to be in the middle of the interval where we expected the transition temperature and another two values at the boundaries of the interval. The results for β in the middle of the interval are highlighted in bold and suggest a 2D Ising model behavior of the system. However, β depends strongly on T_C and therefore further experiments are required to measure the exact transition temperatures and to determine critical exponents more accurately by applying smaller temperature steps.

4. Conclusion

We have implemented a high resolution full q -range SAXS data analysis for homogeneous lipid mixtures, termed SDP-GAP [178], that combines advantages of the GAP [172] (analysis of structural and elastic properties of bilayers) and the SDP analysis [173] (high resolution representation of scattering density profiles and a joint analysis of SAXS and SANS data). The SDP-GAP analysis is capable of analyzing MLV as well as ULV SAXS and/or SANS data based on volume probability distributions of molecular lipid fragments. Thus, parameters such as bilayer thickness, area per lipid, hydrocarbon chain length as well as bending fluctuations can be determined very precisely and used for MD-simulations, where especially the area per lipid plays a key role in the validation of simulations [185].

A major advantage of this analysis is its ability to acquire high resolution structural properties from SAXS data only of MLVs. On the one hand MLVs are easy to prepare compared to ULVs and especially PC lipids hardly form ULVs, even after several extrusion procedures, and on the other hand the accessibility to SAXS experiments is much easier, because of the high number of synchrotrons compared to neutron facilities. A robust analysis could be achieved by the application of a genetic algorithm for the optimization routine to avoid stalling in local minima, due to the high number of free parameters. The SDP-GAP analysis was then tested using several PC lipids and binary mixtures with cholesterol. While values for bilayer thickness and area per lipid are in good agreement with previously reported results using the SDP model [173, 187], the hydrocarbon chain length and the position of the CG group (backbone) could be slightly improved by using also neutron data of POPC and POPC-d₃₁ MLVs and ULVs for a joint analysis.

The SDP-GAP model was further enhanced to a global SAXS data analysis technique for coexisting liquid membrane domains in MLVs [202]. The

4. Conclusion

analysis reveals high resolution structural information of coexisting L_o/L_d domains without knowing their exact tieline endpoints. Furthermore we could determine bending fluctuations of L_o/L_d domains by the analysis of the two distinct Bragg reflections of aligned L_o and L_d domains. We applied this technique to two ternary lipid mixtures consisting of DOPC/DSPC/CHOL and DOPC/DPPC/CHOL. For each mixture endpoint and midpoint data of two different tielines were analyzed as a function of cholesterol concentration and temperature. To test our new analysis, midpoint and endpoint data were compared with respect to bilayer properties, which are in good agreement (but do not match exactly) between coexisting domains and their corresponding pure L_o and L_d phases at the endpoints, corroborating our analysis. The analysis was also able to reproduce differences in bilayer thickness and hydrocarbon chain length of L_o domains between the DSPC and DPPC containing mixtures, due to the variation in chain length between DSPC and DPPC.

We further characterized the influence of additional cholesterol on bilayer properties of coexisting domains for both lipid mixtures (DOPC/DSPC/CHOL and DOPC/DPPC/CHOL). While L_o domains are hardly affected by the higher cholesterol concentrations, L_d domains showed an increase of bilayer thickness and chain length, and a decrease of area per lipid and bending fluctuations. The effect on L_d domains can be understood by the ordering effect of cholesterol, whereas L_o domains seem to be already saturated and therefore unaffected by cholesterol. Consequently also the height mismatch between L_o/L_d domains is reduced at higher cholesterol concentrations, leading to a decrease of line tension and hence to a destabilization of domains. The faster melting of L_o domains at higher cholesterol concentrations, compared to lower concentrations, is a result of this destabilization effect. The melting behavior as well as structural and elastic changes of L_o/L_d domains as a function of temperature suggest further on a diffusion of cholesterol from L_o to L_d domains that is also supported by recent NMR experiments of Davis et al. [126]. Moreover, the domain height mismatch as a function of temperature was analyzed to determine a critical exponent β , describing either a 2D ($\beta = 0.125$) or 3D ($\beta = 0.325$) Ising model behavior of the system. Our results favor a 2D Ising model behavior of the coexisting L_o/L_d phases, but the coarse temperature resolution in our experiments prevent us from any solid

statement.

The third system studied in this work was the four component lipid mixture POPC/DOPC/DSPC/CHOL exhibiting an increase of L_d domain size, ranging from the nano to the macro regime (domain diameter $\sim 14\text{--}50$ nm), by exchanging POPC by DOPC. Macro domains showed alignment across bilayer stacks and therefore our SDP-GAP analysis for coexisting domains could be applied. Whereas nano domains did not show stacking and therefore we enhanced the analysis further to obtain structural information about nano and macro domains as a function of domain size. Thereby a new model for cholesterol with higher resolution was implemented to improve the fit statistics and results for the cholesterol rich L_o phase.

We analyzed the pure L_o and L_d phase of endpoint samples as a function of ρ_{DOPC} , revealing a constant bilayer thickness for the L_o phase and a linear decrease of d_B for the L_d phase with ρ_{DOPC} , which is in good agreement with previously reported results from Heberle et al. [1]. Whereas analyzing the coexisting L_o/L_d domains as a function of domain size (ρ_{DOPC}) revealed differences in the lamellar repeat distance, bilayer thickness, area per lipid, in the behavior of d_B and the domain height mismatch Δd_B , between end- and midpoints. Interestingly, for coexisting domains, we found a five times steeper increase of Δd_B for the nano domain regime than for the macro domains. This effect is a result of the steep increase in d_B of nanoscopic L_d domains, when they are getting smaller and could be understood by the squeezing effect of the L_o surrounding on L_d domains. This effect was also observed for the area per lipid of nanoscopic L_d domains that decreases heavily when domains are getting smaller and are squeezed by the L_o surrounding.

A main unresolved question is still what forces stabilize these nanodomains. Line tension γ for example was found to be a major driving force for domain coalescence [209], but there have to be other competing energetic terms that favor domain break up, resulting in stable nanodomains. On the one hand we observed a monotonic increase in Δd_B accompanied by an increase in γ ($\gamma \propto \Delta d_B^2$) as a function of domain size that facilitates domain coalescence and reveals line tension as the main driving force for coalescence. On the other hand we could observe a five times steeper

4. Conclusion

decrease of Δd_B for the nanodomain regime than for the macro regime, resulting in very small γ values that do not favor domain coalescence when competing repulsive interactions such as entropy [109], dipole–dipole interactions [212], or curvature effects [213–216] are dominant. Δd_B of coexisting macrodomains was further analyzed as a function of temperature exhibiting a monotonic decrease, which was examined in terms of the Ising model behavior. The question whether liquid–liquid domains behave like a 2D or a 3D Ising model is still a controversial issue, whereby our results suggest a 2D Ising model behavior like many other results from microscopy experiments [30, 123, 124].

5. Outlook

The SDP–GAP analysis is an approved tool to obtain structural and elastic information of homogeneous phosphatidylcholine bilayers at high resolution. For future development, the model can be enhanced to analyze also other lipid species, such as phosphatidylethanolamine, phosphatidylserine or phosphatidylglycerol, by adapting the parsing scheme of the lipid headgroup [217]. As plasmamembranes are not symmetric, better model membranes exhibiting an asymmetric lipid distribution between inner and outer leaflet have been already designed and will be further developed in the future. Therefore also the SDP model could be further enhanced to an asymmetric model with different volume probability distributions in each leaflet [218] to jointly analyze SAXS and SANS data respectively. Such an analysis would help to gain deeper insight in the structural differences like hydrocarbon chain length or area per lipid between the two leaflets, which could further on be important for a better understanding of asymmetric plasmamembranes and the effect of cholesterol on bilayer properties.

Plasmamembranes are not only asymmetric, but they are thought to exhibit also compositional inhomogeneities in the form of sphingolipid (cholesterol) enriched platforms, so called lipid rafts. Especially nanoscopic L_o/L_d domains are used as lipid raft mimics and hence more physiologically relevant lipid mixtures such as sphingomyelin containing mixtures [83, 219, 220] that exhibit nanodomains, can be studied with the SDP–GAP model for coexisting domains. Moreover, the melting of domains at fine temperature steps for macro- and nanoscopic domains should be examined to address the controversial issue whether L_o/L_d domains behave like a 2D or a 3D Ising model and if nanoscopic domains show a different Ising model behavior than macroscopic domains.

The prediction of protein activity and partitioning into L_o or L_d domains is another application for our novel analysis [133]. In addition to the struc-

5. Outlook

tural information of L_o/L_d domains, elastic parameters such spontaneous curvatures [221] and bending elasticities [47, 158] have to be taken into account to calculate protein partitioning. Currently Sapp and Maibaum [222] are developing a new theory about membrane–protein interactions, which takes into account membrane properties that can be determined by our analysis. Hence, even more precise predictions about protein partitioning, activity and interactions should be possible.

Bibliography

- [1] Heberle, F. A., R. S. Petruzielo, J. Pan, P. Drazba, N. Kučerka, R. F. Standaert, G. W. Feigenson, and J. Katsaras, 2013. Bilayer thickness mismatch controls domain size in model membranes. *J. Am. Chem. Soc.* 135:6853–6859.
- [2] Escribá, P. V., J. M. González-Ros, F. M. Goñi, P. K. J. Kinnunen, L. Vigh, L. Sánchez-Magraner, A. M. Fernández, X. Busquets, I. Horváth, and G. Barceló-Coblijn, 2008. Membranes: a meeting point for lipids, proteins and therapies. *J. Cell. Mol. Med.* 12:829–875.
- [3] Alberts, B., A. Johnson, J. Lewis, D. Morgan, M. Raff, K. Roberts, and P. Walter, 2014. *Molecular Biology of the Cell*. Taylor & Francis.
- [4] Jianjun Pan, Norbert Kučerka, Mu-Ping Nieh, Frederick A Heberle, Paul Drazba, and John Katsaras, 2014. Lipid Diversity and Its Implications for Membrane Organization. *In Liposomes, Lipid Bilayers and Model Membranes*, CRC Press, 125–142.
- [5] Ikonen, E., 2008. Cellular cholesterol trafficking and compartmentalization. *Nat. Rev. Mol. Cell. Biol.* 9:125–138.
- [6] eHow Contributor. Cell Structure Definitions. http://www.ehow.com/about_5043056_cell-structure-definitions.html.
- [7] Nature Education, Learn Science at Scitable. Cell Membranes. <http://www.nature.com/scitable/topicpage/cell-membranes-14052567>.
- [8] Singer, S. J., and G. L. Nicolson, 1972. The fluid mosaic model of the structure of cell membranes. *Science* 175:720–731.

Bibliography

- [9] Marguet, D., P.-F. Lenne, H. Rigneault, and H.-T. He, 2006. Dynamics in the plasma membrane: how to combine fluidity and order. *EMBO J.* 25:3446–3457.
- [10] Lingwood, D., and K. Simons, 2010. Lipid Rafts As a Membrane-Organizing Principle. *Science* 327:46–50.
- [11] London, E., 2005. How principles of domain formation in model membranes may explain ambiguities concerning lipid raft formation in cells. *Biochim. Biophys. Acta.* 1746:203–220.
- [12] van Meer, G., D. R. Voelker, and G. W. Feigenson, 2008. Membrane lipids: Where they are and how they behave. *Nat. Rev. Mol. Cell Biol.* 9:112–124.
- [13] Heberle, F. A., and G. W. Feigenson, 2011. Phase separation in lipid membranes. *Cold Spring Harbor Perspect. Biol.* 3.
- [14] Manz, B. N., and J. T. Groves, 2010. Spatial organization and signal transduction at intercellular junctions. *Nat. Rev. Mol. Cell Biol.* 11:342–352.
- [15] Wikipedia, the free encyclopedia, 2015. Cell membrane. https://en.wikipedia.org/w/index.php?title=Cell_membrane&oldid=650355548, page Version ID: 650355548.
- [16] Brown, D. A., and J. K. Rose, 1992. Sorting of GPI-anchored proteins to glycolipid-enriched membrane subdomains during transport to the apical cell surface. *Cell* 68:533–544.
- [17] Song, K. S., S. Li, T. Okamoto, L. A. Quilliam, M. Sargiacomo, and M. P. Lisanti, 1996. Co-purification and Direct Interaction of Ras with Caveolin, an Integral Membrane Protein of Caveolae Microdomains. *J. Biol. Chem.* 271:9690–9697.
- [18] Lingwood, D., and K. Simons, 2007. Detergent resistance as a tool in membrane research. *Nat. Protoc.* 2:2159–2165.
- [19] Jacobson, K., O. G. Mouritsen, and R. G. W. Anderson, 2007. Lipid rafts: at a crossroad between cell biology and physics. *Nat. Cell. Biol.* 9:7–14.

- [20] Hancock, J. F., 2006. Lipid rafts: contentious only from simplistic standpoints. *Nat. Rev. Mol. Cell. Biol.* 7:456–462.
- [21] Friedrichson, T., and T. V. Kurzchalia, 1998. Microdomains of GPI-anchored proteins in living cells revealed by crosslinking. *Nature* 394:802–805.
- [22] Pralle, A., P. Keller, E.-L. Florin, K. Simons, and J. Hörber, 2000. Sphingolipid–Cholesterol Rafts Diffuse as Small Entities in the Plasma Membrane of Mammalian Cells. *J. Cell. Biol.* 148:997–1008.
- [23] van Zanten, T. S., A. Cambi, M. Koopman, B. Joosten, C. G. Figdor, and M. F. Garcia-Parajo, 2009. Hotspots of GPI-anchored proteins and integrin nanoclusters function as nucleation sites for cell adhesion. *Proc. Natl. Acad. Sci. U.S.A.* 106:18557–18562.
- [24] Suzuki, K. G., T. K. Fujiwara, F. Sanematsu, R. Iino, M. Edidin, and A. Kusumi, 2007. GPI-anchored receptor clusters transiently recruit Lyn and G α for temporary cluster immobilization and Lyn activation: single-molecule tracking study 1. *J. Cell. Biol.* 177:717–730.
- [25] Lenne, P.-F., L. Wawrezynieck, F. Conchonaud, O. Wurtz, A. Boned, X.-J. Guo, H. Rigneault, H.-T. He, and D. Marguet, 2006. Dynamic molecular confinement in the plasma membrane by microdomains and the cytoskeleton meshwork. *EMBO. J.* 25:3245–3256.
- [26] Lasserre, R., X.-J. Guo, F. Conchonaud, Y. Hamon, O. Hawchar, A.-M. Bernard, S. M. Soudja, P.-F. Lenne, H. Rigneault, D. Olive, G. Bismuth, J. A. Nunès, B. Payrastre, D. Marguet, and H.-T. He, 2008. Raft nanodomains contribute to Akt/PKB plasma membrane recruitment and activation. *Nat. Chem. Biol.* 4:538–547.
- [27] Hess, S. T., T. J. Gould, M. V. Gudheti, S. A. Maas, K. D. Mills, and J. Zimmerberg, 2007. Dynamic clustered distribution of hemagglutinin resolved at 40 nm in living cell membranes discriminates between raft theories. *Proc. Natl. Acad. Sci. U.S.A.* 104:17370–17375.
- [28] Eggeling, C., C. Ringemann, R. Medda, G. Schwarzmann, K. Sandhoff, S. Polyakova, V. N. Belov, B. Hein, C. von Middendorff,

Bibliography

- A. Schönle, and S. W. Hell, 2009. Direct observation of the nanoscale dynamics of membrane lipids in a living cell. *Nature* 457:1159–1162.
- [29] Swamy, M. J., L. Ciani, M. Ge, A. K. Smith, D. Holowka, B. Baird, and J. H. Freed, 2006. Coexisting Domains in the Plasma Membranes of Live Cells Characterized by Spin-Label ESR Spectroscopy. *Biophys. J.* 90:4452–4465.
- [30] Veatch, S. L., P. Cicuta, P. Sengupta, A. Honerkamp-Smith, D. Holowka, and B. Baird, 2008. Critical Fluctuations in Plasma Membrane Vesicles. *ACS Chem. Biol.* 3:287–293.
- [31] Goswami, D., K. Gowrishankar, S. Bilgrami, S. Ghosh, R. Raghupathy, R. Chadda, R. Vishwakarma, M. Rao, and S. Mayor, 2008. Nanoclusters of GPI-Anchored Proteins Are Formed by Cortical Actin-Driven Activity. *Cell* 135:1085–1097.
- [32] Umemura, Y. M., M. Vrljic, S. Y. Nishimura, T. K. Fujiwara, K. G. N. Suzuki, and A. Kusumi, 2008. Both MHC Class II and its GPI-Anchored Form Undergo Hop Diffusion as Observed by Single-Molecule Tracking. *Biophys. J.* 95:435–450.
- [33] Fujita, A., J. Cheng, and T. Fujimoto, 2009. Segregation of GM1 and GM3 clusters in the cell membrane depends on the intact actin cytoskeleton. *Biochim. Biophys. Acta.* 1791:388–396.
- [34] Gowrishankar, K., S. Ghosh, S. Saha, R. C., S. Mayor, and M. Rao, 2012. Active Remodeling of Cortical Actin Regulates Spatiotemporal Organization of Cell Surface Molecules. *Cell* 149:1353–1367.
- [35] Frisz, J. F., K. Lou, H. A. Klitzing, W. P. Hanafin, V. Lizunov, R. L. Wilson, K. J. Carpenter, R. Kim, I. D. Hutcheon, J. Zimmerberg, P. K. Weber, and M. L. Kraft, 2013. Direct chemical evidence for sphingolipid domains in the plasma membranes of fibroblasts. *Proc. Natl. Acad. Sci. U.S.A.* .
- [36] Frisz, J. F., H. A. Klitzing, K. Lou, I. D. Hutcheon, P. K. Weber, J. Zimmerberg, and M. L. Kraft, 2013. Sphingolipid domains in the plasma membranes of fibroblasts are not enriched with cholesterol. *J. Biol. Chem.* 288:16855–16861.

- [37] Mueller, V., C. Ringemann, A. Honigmann, G. Schwarzmann, R. Medda, M. Leutenegger, S. Polyakova, V. Belov, S. Hell, and C. Eggeling, 2011. STED Nanoscopy Reveals Molecular Details of Cholesterol- and Cytoskeleton-Modulated Lipid Interactions in Living Cells. *Biophys. J.* 101:1651–1660.
- [38] Fujita, A., J. Cheng, M. Hirakawa, K. Furukawa, S. Kusunoki, and T. Fujimoto, 2007. Gangliosides GM₁ and GM₃ in the Living Cell Membrane Form Clusters Susceptible to Cholesterol Depletion and Chilling. *Mol. Biol. Cell.* 18:2112–2122.
- [39] Janich, P., and D. Corbeil, 2007. GM₁ and GM₃ gangliosides highlight distinct lipid microdomains within the apical domain of epithelial cells. *FEBS Lett.* 581:1783–1787.
- [40] Chen, Y., J. Qin, and Z. W. Chen, 2008. Fluorescence-topographic NSOM directly visualizes peak-valley polarities of GM₁/GM₃ rafts in cell membrane fluctuations. *J. Lipid Res.* 49:2268–2275.
- [41] Tyteca, D., L. D’Auria, P. V. Der Smissen, T. Medts, S. Carpentier, J. C. Monbaliu, P. de Diesbach, and P. J. Courtoy, 2010. Three unrelated sphingomyelin analogs spontaneously cluster into plasma membrane micrometric domains. *Biochim. Biophys. Acta* 1798:909–927.
- [42] D’Auria, L., M. Fenaux, P. Aleksandrowicz, P. Van Der Smissen, C. Chantrain, C. Vermylen, M. Vikkula, P. J. Courtoy, and D. Tyteca, 2013. Micrometric segregation of fluorescent membrane lipids: relevance for endogenous lipids and biogenesis in erythrocytes. *J. Lipid Res.* 54:1066–1076.
- [43] Kraft, M. L., 2013. Plasma membrane organization and function: moving past lipid rafts. *Mol. Biol. Cell* 24:2765–2768.
- [44] what-when-how; In depth tutorials and information. Nanoencapsulation of Bioactive Substances (Nanotechnology). <http://what-when-how.com/nanoscience-and-nanotechnology/nanoencapsulation-of-bioactive-substances-part-1/nanotechnology/>.

Bibliography

- [45] Simons, K., and W. L. Vaz, 2004. Model Systems, Lipid Rafts, and Cell Membranes¹. *Annu. Rev. Biophys.* 33:269–295.
- [46] Salditt, T., 2005. Thermal fluctuations and stability of solid-supported lipid membranes. *J. Phys.: Condens. Matter* 17:R287–R314.
- [47] Pabst, G., N. Kučerka, M.-P. Nieh, M. Rheinstädter, and J. Katsaras, 2010. Applications of neutron and X-ray scattering to the study of biologically relevant model membranes. *Chem. Phys. Lipids* 163:460–479.
- [48] Koynova, R., and B. Tenchov, 2013. Transitions between lamellar and non-lamellar phases in membrane lipids and their physiological roles. *OA Biochemistry* 9.
- [49] Rappolt, M., 2006. Chapter 9 The Biologically Relevant Lipid Mesophases as “Seen” by X-Rays. In A. L. Liu, editor, *Advances in Planar Lipid Bilayers and Liposomes*, Academic Press, volume 5, 253–283.
- [50] Mouritsen, O. G., 2005. *Life - as a matter of fat: the emerging science of lipidomics*. Springer-Verlag, Berlin.
- [51] Róg, T., M. Pasenkiewicz-Gierula, I. Vattulainen, and M. Karttunen, 2009. Ordering effects of cholesterol and its analogues. *Biochim. Biophys. Acta* 1788:97–121.
- [52] Martinez-Seara, H., T. Róg, M. Pasenkiewicz-Gierula, I. Vattulainen, M. Karttunen, and R. Reigada, 2008. Interplay of Unsaturated Phospholipids and Cholesterol in Membranes: Effect of the Double-Bond Position. *Biophys. J.* 95:3295–3305.
- [53] Marsh, D., and I. C. P. Smith, 1973. An interacting spin label study of the fluidizing and condensing effects of cholesterol on lecithin bilayers. *Biochim. Biophys. Acta* 298:133–144.
- [54] Oldfield, E., M. Meadows, D. Rice, and R. Jacobs, 1978. Spectroscopic studies of specifically deuterium labeled membrane systems. Nuclear magnetic resonance investigation of the effects of cholesterol in model systems. *Biochemistry* 17:2727–2740.

Bibliography

- [55] Urbina, J. A., S. Pekerar, H.-b. Le, J. Patterson, B. Montez, and E. Oldfield, 1995. Molecular order and dynamics of phosphatidylcholine bilayer membranes in the presence of cholesterol, ergosterol and lanosterol: a comparative study using ^2H -, ^{13}C - and ^{31}P -NMR spectroscopy. *Biochim. Biophys. Acta* 1238:163–176.
- [56] Demel, R. A., L. L. M. Van Deenen, and B. A. Pethica, 1967. Monolayer interactions of phospholipids and cholesterol. *Biochim. Biophys. Acta* 135:11–19.
- [57] Stottrup, B. L., D. S. Stevens, and S. L. Keller, 2005. Miscibility of Ternary Mixtures of Phospholipids and Cholesterol in Monolayers, and Application to Bilayer Systems. *Biophys. J.* 88:269–276.
- [58] Levine, Y. K., and M. H. F. Wilkins, 1971. Structure of Oriented Lipid Bilayers. *Nature* 230:69–72.
- [59] McIntosh, T. J., 1978. The effect of cholesterol on the structure of phosphatidylcholine bilayers. *Biochim. Biophys. Acta.* 513:43–58.
- [60] Franks, N. P., 1976. Structural analysis of hydrated egg lecithin and cholesterol bilayers I. X-ray diffraction. *J. Mol. Biol.* 100:345–358.
- [61] Worcester, D. L., and N. P. Franks, 1976. Structural analysis of hydrated egg lecithin and cholesterol bilayers II. Neutron diffraction. *J. Mol. Biol.* 100:359–378.
- [62] Rappolt, M., F. Vidal, M. Kriechbaum, M. Steinhart, H. Amenitsch, S. Bernstorff, and P. Laggner, 2003. Structural, dynamic and mechanical properties of POPC at low cholesterol concentration studied in pressure/temperature space. *Eur. Biophys. J.* 31:575.
- [63] Gallová, J., D. Uhríková, N. Kučerka, J. Teixeira, and P. Balgavý, 2008. Hydrophobic thickness, lipid surface area and polar region hydration in monounsaturated diacylphosphatidylcholine bilayers: SANS study of effects of cholesterol and β -sitosterol in unilamellar vesicles. *Biochim. Biophys. Acta* 1778:2627–2632.

Bibliography

- [64] Pencer, J., M.-P. Nieh, T. A. Harroun, S. Krueger, C. Adams, and J. Katsaras, 2005. Bilayer thickness and thermal response of dimyristoylphosphatidylcholine unilamellar vesicles containing cholesterol, ergosterol and lanosterol: A small-angle neutron scattering study. *Biochim. Biophys. Acta* 1720:84–91.
- [65] Hung, W.-C., M.-T. Lee, F.-Y. Chen, and H. W. Huang, 2007. The condensing effect of cholesterol in lipid bilayers. *Biophys. J.* 92:3960–3967.
- [66] Pan, J., T. T. Mills, S. Tristram-Nagle, and J. F. Nagle, 2008. Cholesterol perturbs lipid bilayers nonuniversally. *Phys. Rev. Lett.* 100:198103.
- [67] Pan, J., X. Cheng, F. A. Heberle, B. Mostofian, N. Kučerka, P. Drazba, and J. Katsaras, 2012. Interactions between ether phospholipids and cholesterol as determined by scattering and molecular dynamics simulations. *J. Phys. Chem. B* 116:14829–14838.
- [68] Chong, P. L., 1994. Evidence for regular distribution of sterols in liquid crystalline phosphatidylcholine bilayers. *Proc. Natl. Acad. Sci. U.S.A.* 91:10069–10073.
- [69] Radhakrishnan, A., and H. M. McConnell, 1999. Condensed Complexes of Cholesterol and Phospholipids. *Biophys. J.* 77:1507–1517.
- [70] Radhakrishnan, A., T. G. Anderson, and H. M. McConnell, 2000. Condensed complexes, rafts, and the chemical activity of cholesterol in membranes. *Proc. Natl. Acad. Sci. U.S.A.* 97:12422–12427.
- [71] Huang, J., and G. W. Feigenson, 1999. A microscopic interaction model of maximum solubility of cholesterol in lipid bilayers. *Biophys. J.* 76:2142–2157.
- [72] Huang, J., 2002. Exploration of Molecular Interactions in Cholesterol Superlattices: Effect of Multibody Interactions. *Biophys. J.* 83:1014–1025.
- [73] Simons, K., and E. Ikonen, 1997. Functional rafts in cell membranes. *Nature* 387:569–572.

- [74] Marsh, D., 2010. Liquid-ordered phases induced by cholesterol: A compendium of binary phase diagrams. *Biochim. Biophys. Acta.* 1798:688–699.
- [75] Sankaram, M. B., and T. E. Thompson, 1991. Cholesterol-induced fluid-phase immiscibility in membranes. *Proc. Natl. Acad. Sci. U.S.A.* 88:8686–8690.
- [76] Collado, M. I., F. M. Goñi, A. Alonso, and D. Marsh, 2005. Domain formation in sphingomyelin/cholesterol mixed membranes studied by spin-label electron spin resonance spectroscopy†. *Biochemistry* 44:4911–4918.
- [77] Davis, J. H., J. J. Clair, and J. Juhasz, 2009. Phase Equilibria in DOPC/DPPC-d62/Cholesterol Mixtures. *Biophys. J.* 96:521–539.
- [78] Mabrey, S., and J. M. Sturtevant, 1976. Investigation of phase transitions of lipids and lipid mixtures by sensitivity differential scanning calorimetry. *Proc. Natl. Acad. Sci. U.S.A.* 73:3862–3866.
- [79] Loura, L. M., R. F. de Almeida, L. C. Silva, and M. Prieto, 2009. FRET analysis of domain formation and properties in complex membrane systems. *Biochim. Biophys. Acta.* 1788:209–224.
- [80] Degroote, S., J. Wolthoorn, and G. van Meer, 2004. The cell biology of glycosphingolipids. *Semin. Cell Dev. Biol.* 15:375–387.
- [81] Cahn, J. W., 1961. On spinodal decomposition. *Acta Mater.* 9:795–801.
- [82] Sengers, J. V., and J. M. H. L. Sengers, 1986. Thermodynamic Behavior of Fluids Near the Critical Point. *Annu. Rev. Phys. Chem.* 37:189–222.
- [83] Veatch, S. L., and S. L. Keller, 2005. Seeing spots: Complex phase behavior in simple membranes. *Biochim. Biophys. Acta.* 1746:172–185.
- [84] Veatch, S. L., and S. L. Keller, 2003. Separation of Liquid Phases in Giant Vesicles of Ternary Mixtures of Phospholipids and Cholesterol. *Biophys. J.* 85:3074–3083.

Bibliography

- [85] Marsh, D., 2009. Cholesterol-induced fluid membrane domains: A compendium of lipid-raft ternary phase diagrams. *Biochim. Biophys. Acta.* 1788:2114–2123.
- [86] de Almeida, R. F. M., A. Fedorov, and M. Prieto, 2003. Sphingomyelin/Phosphatidylcholine/Cholesterol phase diagram: Boundaries and composition of lipid rafts. *Biophys. J.* 85:2406–2416.
- [87] Veatch, S. L., and S. L. Keller, 2005. Miscibility phase diagrams of giant vesicles containing sphingomyelin. *Phys. Rev. Lett.* 94:148101.
- [88] Pokorny, A., L. E. Yandek, A. I. Elegbede, A. Hinderliter, and P. F. F. Almeida, 2006. Temperature and Composition Dependence of the Interaction of δ -Lysin with Ternary Mixtures of Sphingomyelin/Cholesterol/POPC. *Biophys. J.* 91:2184–2197.
- [89] Zhao, J., J. Wu, H. Shao, F. Kong, N. Jain, G. Hunt, and G. Feigenson, 2007. Phase studies of model biomembranes: Macroscopic coexistence of $L\alpha + L\beta$, with light-induced coexistence of $L\alpha + L_o$ Phases. *Biochim. Biophys. Acta.* 1768:2777–2786.
- [90] Veatch, S. L., O. Soubias, S. L. Keller, and K. Gawrisch, 2007. Critical fluctuations in domain-forming lipid mixtures. *Proc. Natl. Acad. Sci. U.S.A.* 104:17650–17655.
- [91] Chiang, Y.-W., J. Zhao, J. Wu, Y. Shimoyama, J. H. Freed, and G. W. Feigenson, 2005. New method for determining tie-lines in coexisting membrane phases using spin-label ESR. *Biochim. Biophys. Acta.* 1668:99–105.
- [92] Veatch, S. L., K. Gawrisch, and S. L. Keller, 2006. Closed-Loop Miscibility Gap and Quantitative Tie-Lines in Ternary Membranes Containing Diphytanoyl PC. *Biophys. J.* 90:4428–4436.
- [93] Silvius, J. R., D. del Giudice, and M. Lafleur, 1996. Cholesterol at Different Bilayer Concentrations Can Promote or Antagonize Lateral Segregation of Phospholipids of Differing Acyl Chain Length. *Biochemistry* 35:15198–15208.

- [94] Feigenson, G. W., and J. T. Buboltz, 2001. Ternary phase diagram of dipalmitoyl-PC/dilauroyl-PC/cholesterol: nanoscopic domain formation driven by cholesterol. *Biophys. J.* 80:2775–2788.
- [95] Uppamoochikkal, P., S. Tristram-Nagle, and J. F. Nagle, 2010. Orientation of tie-lines in the phase diagram of DOPC:DPPC:cholesterol model biomembranes. *Langmuir* 26:17363–17368.
- [96] Heberle, F. A., J. Wu, S. L. Goh, R. S. Petruzielo, and G. W. Feigenson, 2010. Comparison of three ternary lipid bilayer mixtures: FRET and ESR reveal nanodomains. *Biophys. J.* 99:3309–3318.
- [97] Vist, M. R., and J. H. Davis, 1990. Phase equilibria of cholesterol/dipalmitoylphosphatidylcholine mixtures: deuterium nuclear magnetic resonance and differential scanning calorimetry. *Biochemistry* 29:451–464.
- [98] Feigenson, G. W., 2009. Phase diagrams and lipid domains in multi-component lipid bilayer mixtures. *Biochim. Biophys. Acta* 1788:47–52.
- [99] Bleecker, J. V., P. A. Cox, and S. L. Keller, 2015. Comparing Lo/Ld Membrane Thickness Mismatch and Miscibility Transition Temperatures using Fluorescence and Atomic Force Microscopy. *Biophys. J.* 108:241a.
- [100] Gandhavadi, M., D. Allende, A. Vidal, S. A. Simon, and T. J. McIntosh, 2002. Structure, composition, and peptide binding properties of detergent soluble bilayers and detergent resistant rafts. *Biophys. J.* 82:1469–1482.
- [101] Bleecker, J. V., P. A. Cox, R. N. Foster, D. G. Castner, and S. L. Keller, 2014. Membranes with Thick, Liquid-Disordered and Thin, Liquid-Ordered Phases are Rare. *Biophys. J.* 106:92a.
- [102] Bechinger, B., 2012. Lipid multilayers: Domains stack up. *Nat. Mater.* 11:1005–1006.
- [103] Tayebi, L., Y. Ma, D. Vashaee, G. Chen, S. K. Sinha, and A. N. Parikh, 2012. Long-range interlayer alignment of intralayer domains in stacked lipid bilayers. *Nat. Mater.* 11:1074–1080.

Bibliography

- [104] Tayebi, L., A. Parikh, and D. Vashaee, 2013. Interlamellar organization of phase separated domains in multi-component lipid multilayers: Energetic considerations. *Int. J. Mol. Sci.* 14:3824–3833.
- [105] Konyakhina, T. M., S. L. Goh, J. Amazon, F. A. Heberle, J. Wu, and G. W. Feigenson, 2011. Control of a Nanoscopic-to-Macroscopic Transition: Modulated Phases in Four-Component DSPC/DOPC/POPC/Chol Giant Unilamellar Vesicles. *Biophys. J.* 101:L8–L10.
- [106] Lisy, V., and B. Brutovsky, 2000. Interpretation of static and dynamic neutron and light scattering from microemulsion droplets: Effects of shape fluctuations. *Phys. Rev. E* 61:4045–4053.
- [107] McConnell, H. M., 1991. Structures and Transitions in Lipid Monolayers at the Air-Water Interface. *Annu. Rev. Phys. Chem.* 42:171–195.
- [108] Groves, J. T., 2007. Bending mechanics and molecular organization in biological membranes. *Annu. Rev. Phys. Chem.* 58:697–717.
- [109] Frolov, V. A. J., Y. A. Chizmadzhev, F. S. Cohen, and J. Zimmerberg, 2006. “Entropic Traps” in the Kinetics of Phase Separation in Multicomponent Membranes Stabilize Nanodomains. *Biophys. J.* 91:189–205.
- [110] Esposito, C., A. Tian, S. Melamed, C. Johnson, S.-Y. Tee, and T. Baumgart, 2007. Flicker Spectroscopy of Thermal Lipid Bilayer Domain Boundary Fluctuations. *Biophys. J.* 93:3169–3181.
- [111] Honerkamp-Smith, A. R., S. L. Veatch, and S. L. Keller, 2009. An introduction to critical points for biophysicists; observations of compositional heterogeneity in lipid membranes. *Biochim. Biophys. Acta.* 1788:53–63.
- [112] Schick, M., 2012. Membrane heterogeneity: Manifestation of a curvature-induced microemulsion. *Phys. Rev. E* 85:031902.
- [113] Palmieri, B., and S. A. Safran, 2013. Hybrid Lipids Increase the Probability of Fluctuating Nanodomains in Mixed Membranes. *Langmuir* 29:5246–5261.

- [114] Hirose, Y., S. Komura, and D. Andelman, 2012. Concentration fluctuations and phase transitions in coupled modulated bilayers. *Phys. Rev. E* 86:021916.
- [115] Shlomovitz, R., and M. Schick, 2013. Model of a raft in both leaves of an asymmetric lipid bilayer. *Biophys. J.* 105:1406–1413.
- [116] Shlomovitz, R., L. Maibaum, and M. Schick, 2014. Macroscopic Phase Separation, Modulated Phases, and Microemulsions: A Unified Picture of Rafts. *Biophys. J.* 106:1979–1985.
- [117] Brewster, R., P. Pincus, and S. Safran, 2009. Hybrid Lipids as a Biological Surface-Active Component. *Biophys. J.* 97:1087–1094.
- [118] Leibler, S., and D. Andelman, 1987. Ordered and curved mesostructures in membranes and amphiphilic films. *Eur. Phys. J.* 48:2013–2018.
- [119] Leibler, S., 1986. Curvature instability in membranes. *Eur. Phys. J.* 47:507–516.
- [120] Widom, B., 1965. Surface Tension and Molecular Correlations near the Critical Point. *J. Chem. Phys.* 43:3892–3897.
- [121] Nobili, M., and G. Durand, 1994. Critical Behaviour of a Nematic-Liquid-Crystal Anchoring at a Monostable-Bistable Surface Transition. *EPL-Europhys. Lett.* 25:527.
- [122] Dunlavy, M. J., and D. Venus, 2005. Critical slowing down in the two-dimensional Ising model measured using ferromagnetic ultrathin films. *Phys. Rev. B* 71:144406.
- [123] Honerkamp-Smith, A. R., P. Cicutta, M. D. Collins, S. L. Veatch, M. den Nijs, M. Schick, and S. L. Keller, 2008. Line tensions, correlation lengths, and critical exponents in lipid membranes near critical points. *Biophys. J.* 95:236–246.
- [124] Honerkamp-Smith, A. R., B. B. Machta, and S. L. Keller, 2012. Experimental observations of dynamic critical phenomena in a lipid membrane. *Phys. Rev. Lett.* 108.

Bibliography

- [125] Connell, S. D., G. Heath, P. D. Olmsted, and A. Kisil, 2013. Critical point fluctuations in supported lipid membranes. *Farad. Discuss.* 161:91.
- [126] Davis, J. H., and M. L. Schmidt, 2014. Critical behaviour in DOPC/DPPC/cholesterol mixtures: Static ^2H NMR line shapes near the critical point. *Biophys. J.* 106:1970–1978.
- [127] Goh, S., J. Amazon, and G. Feigenson, 2013. Toward a better raft model: Modulated phases in the four-component bilayer, DSPC/DOPC/POPC/CHOL. *Biophys. J.* 104:853–862.
- [128] Amazon, J. J., S. L. Goh, and G. W. Feigenson, 2013. Competition between line tension and curvature stabilizes modulated phase patterns on the surface of giant unilamellar vesicles: a simulation study. *Phys. Rev. E* 87:022708.
- [129] Akimov, S. A., P. I. Kuzmin, J. Zimmerberg, F. S. Cohen, and Y. A. Chizmadzhev, 2004. An elastic theory for line tension at a boundary separating two lipid monolayer regions of different thickness. *J. Electroanal. Chem.* 564:13–18.
- [130] Benting, J., A. Rietveld, I. Ansorge, and K. Simons, 1999. Acyl and alkyl chain length of GPI-anchors is critical for raft association in vitro. *FEBS Lett.* 462:47–50.
- [131] Sharma, P., R. Varma, R. C. Sarasij, Ira, K. Gousset, G. Krishnamoorthy, M. Rao, and S. Mayor, 2004. Nanoscale organization of multiple GPI-anchored proteins in living cell membranes. *Cell* 116:577–589.
- [132] Young, R. M., D. Holowka, and B. Baird, 2003. A lipid raft environment enhances lyn kinase activity by protecting the active site tyrosine from dephosphorylation. *J. Biol. Chem.* 278:20746–20752.
- [133] Pabst, G., 2013. Coupling of Membrane Elasticity and Structure to Protein Function. In A. Iglic, and C. Kulkarni, editors, *Advances in planar lipid bilayers and liposomes*, Academic Press, volume 18, 282.

- [134] Lundbæk, J. A., O. S. Andersen, T. Werge, and C. Nielsen, 2003. Cholesterol-induced protein sorting: An analysis of energetic feasibility. *Biophys. J.* 84:2080–2089.
- [135] McIntosh, T. J., A. Vidal, and S. A. Simon, 2003. Sorting of Lipids and Transmembrane Peptides Between Detergent-Soluble Bilayers and Detergent-Resistant Rafts. *Biophys. J.* 85:1656–1666.
- [136] Vidal, A., and T. J. McIntosh, 2005. Transbilayer peptide sorting between raft and nonraft bilayers: Comparisons of detergent extraction and confocal microscopy. *Biophys. J.* 89:1102–1108.
- [137] Rawicz, W., B. A. Smith, T. J. McIntosh, S. A. Simon, and E. Evans, 2008. Elasticity, strength, and water permeability of bilayers that contain raft microdomain-forming lipids. *Biophys. J.* 94:4725–4736.
- [138] Cantor, R. S., 1999. The influence of membrane lateral pressures on simple geometric models of protein conformational equilibria. *Chem. Phys. Lipids* 101:45–56.
- [139] Lundbæk, J. A., S. A. Collingwood, H. I. Ingólfsson, R. Kapoor, and O. S. Andersen, 2010. Lipid bilayer regulation of membrane protein function: gramicidin channels as molecular force probes. *J. R. Soc. Interface* 7:373–395.
- [140] Andersen, O. S., and R. E. Koeppe, 2007. Bilayer thickness and membrane protein function: An energetic perspective. *Annu. Rev. Biophys.* 36:107–130.
- [141] Killian, J. A., 1998. Hydrophobic mismatch between proteins and lipids in membranes. *Biochim. Biophys. Acta.* 1376:401–416.
- [142] Ren, J., S. Lew, J. Wang, and E. London, 1999. Control of the transmembrane orientation and interhelical interactions within membranes by hydrophobic helix length. *Biochemistry* 38:5905–5912.
- [143] Bretscher, M. S., and S. Munro, 1993. Cholesterol and the Golgi apparatus. *Science* 261:1280–1281.

Bibliography

- [144] de Planque, M. R. R., E. Goormaghtigh, D. V. Greathouse, R. E. Koeppe, J. A. W. Kruijtzter, R. M. J. Liskamp, B. de Kruijff, and J. A. Killian, 2001. Sensitivity of Single Membrane-Spanning α -Helical Peptides to Hydrophobic Mismatch with a Lipid Bilayer: Effects on Backbone Structure, Orientation, and Extent of Membrane Incorporation. *Biochemistry* 40:5000–5010.
- [145] McIntosh, T. J., S. A. Simon, D. Needham, and C. H. Huang, 1992. Interbilayer interactions between sphingomyelin and sphingomyelin/cholesterol bilayers. *Biochemistry* 31:2020–2024.
- [146] Gruner, S. M., 1985. Intrinsic curvature hypothesis for biomembrane lipid composition: a role for nonbilayer lipids. *Proc. Natl. Acad. Sci. U.S.A.* 82:3665–3669.
- [147] Cantor, R. S., 1997. Lateral pressures in cell membranes: a mechanism for modulation of protein function. *J. Phys. Chem. B* 101:1723–1725.
- [148] Brown, A. C., and S. P. Wrenn, 2013. Nanoscale phase separation in DSPC–Cholesterol systems. *Langmuir* 29:9832–9840.
- [149] Binder, W. H., V. Barragan, and F. M. Menger, 2003. Domains and rafts in lipid membranes. *Angew. Chem. Int. Ed.* 42:5802–5827.
- [150] Veatch, S. L., and S. L. Keller, 2002. Organization in lipid membranes containing cholesterol. *Phys. Rev. Lett.* 89:268101.
- [151] Pitcher III, W. H., S. L. Keller, and W. H. Huestis, 2002. Interaction of nominally soluble proteins with phospholipid monolayers at the air–water interface. *Biochim. Biophys. Acta.* 1564:107–113.
- [152] Chiang, Y.-W., Y. Shimoyama, G. W. Feigenson, and J. H. Freed, 2004. Dynamic molecular structure of DPPC-DLPC-cholesterol ternary lipid system by spin-label electron spin resonance. *Biophys. J.* 87:2483–2496.
- [153] Ionova, I. V., V. A. Livshits, and D. Marsh, 2012. Phase diagram of ternary cholesterol/palmitoylsphingomyelin/palmitoyloleoylphosphatidylcholine mixtures: Spin-label EPR study of lipid-raft formation. *Biophys. J.* 102:1856–1865.

- [154] Tokumasu, F., A. J. Jin, G. W. Feigenson, and J. A. Dvorak, 2003. Nanoscopic lipid domain dynamics revealed by atomic force microscopy. *Biophys. J.* 84:2609–2618.
- [155] Mills, T. T., S. Tristram-Nagle, F. A. Heberle, N. F. Morales, J. Zhao, J. Wu, G. E. S. Toombes, J. F. Nagle, and G. W. Feigenson, 2008. Liquid-Liquid Domains in Bilayers Detected by Wide Angle X-Ray Scattering. *Biophys. J.* 95:682–690.
- [156] Chen, L., Z. Yu, and P. J. Quinn, 2007. The partition of cholesterol between ordered and fluid bilayers of phosphatidylcholine: A synchrotron X-ray diffraction study. *Biochim. Biophys. Acta.* 1768:2873–2881.
- [157] Bennett, W. F. D., and D. P. Tieleman, 2013. Computer simulations of lipid membrane domains. *Biochim. Biophys. Acta.* 1828:1765–1776.
- [158] Khelashvili, G., B. Kollmitzer, P. Heftberger, G. Pabst, and D. Harries, 2013. Calculating the bending modulus for multicomponent lipid membranes in different thermodynamic phases. *J. Chem. Theory Comput.* 9:3866–3871.
- [159] Veatch, S. L., I. V. Polozov, K. Gawrisch, and S. L. Keller, 2004. Liquid domains in vesicles investigated by NMR and fluorescence microscopy. *Biophys. J.* 86:2910–2922.
- [160] Dietrich, C., L. A. Bagatolli, Z. N. Volovyk, N. L. Thompson, M. Levi, K. Jacobson, and E. Gratton, 2001. Lipid rafts reconstituted in model membranes. *Biophys. J.* 80:1417–1428.
- [161] Veatch, S. L., S. S. W. Leung, R. E. W. Hancock, and J. L. The-walt, 2007. Fluorescent probes alter miscibility phase boundaries in ternary vesicles. *J. Phys. Chem. B* 111:502–504.
- [162] Ayuyan, A. G., and F. S. Cohen, 2006. Lipid peroxides promote large rafts: Effects of excitation of probes in fluorescence microscopy and electrochemical reactions during vesicle formation. *Biophys. J.* 91:2172–2183.

Bibliography

- [163] Haluska, C. K., A. P. Schröder, P. Didier, D. Heissler, G. Duportail, Y. Mély, and C. M. Marques, 2008. Combining Fluorescence Lifetime and Polarization Microscopy to Discriminate Phase Separated Domains in Giant Unilamellar Vesicles. *Biophys. J.* 95:5737–5747.
- [164] Kinosita, K., S. Kawato, and A. Ikegami, 1984. Dynamic structure of biological and model membranes: analysis by optical anisotropy decay measurement. *Adv. Biophys.* 17:147–203.
- [165] London, E., and G. W. Feigenson, 1981. Fluorescence quenching in model membranes. 1. Characterization of quenching caused by a spin-labeled phospholipid. *Biochemistry* 20:1932–1938.
- [166] Schneider, D. J., and J. H. Freed, 1989. Calculating Slow Motional Magnetic Resonance Spectra. In L. J. Berliner, and J. Reuben, editors, Spin Labeling, Springer US, number 8 in Biological Magnetic Resonance, 1–76.
- [167] Sahl, S. J., M. Leutenegger, M. Hilbert, S. W. Hell, and C. Eggeling, 2010. Fast molecular tracking maps nanoscale dynamics of plasma membrane lipids. *Proc. Natl. Acad. Sci. U.S.A.* 107:6829–6834.
- [168] Veiga, M. P., J. L. R. Arrondo, F. M. Goñi, A. Alonso, and D. Marsh, 2001. Interaction of cholesterol with sphingomyelin in mixed membranes containing phosphatidylcholine, studied by spin-label ESR and IR spectroscopies. A possible stabilization of gel-phase sphingolipid domains by cholesterol†. *Biochemistry* 40:2614–2622.
- [169] de Wit, G., J. S. H. Danial, P. Kukura, and M. I. Wallace, 2015. Real-Time Imaging of Nanoscopic Lipid Domains using iSCAT. *Biophys. J.* 108:17a–18a.
- [170] Blaurock, A. E., and C. R. Worthington, 1966. Treatment of Low Angle X-Ray Data from Planar and Concentric Multilayered Structures. *Biophys. J.* 6:305–312.
- [171] McIntosh, T. J., A. D. Magid, and S. A. Simon, 1989. Range of the solvation pressure between lipid membranes: dependence on the packing density of solvent molecules. *Biochemistry* 28:7904–7912.

- [172] Pabst, G., M. Rappolt, H. Amenitsch, and P. Laggner, 2000. Structural information from multilamellar liposomes at full hydration: Full q -range fitting with high quality x-ray data. *Phys. Rev. E* 62:4000–4009.
- [173] Kučerka, N., J. F. Nagle, J. N. Sachs, S. E. Feller, J. Pencer, A. Jackson, and J. Katsaras, 2008. Lipid bilayer structure determined by the simultaneous analysis of neutron and X-ray scattering data. *Biophys. J.* 95:2356–2367.
- [174] Carpenter, J. M., 2006. Introduction to Theory of Neutron Scattering.
- [175] Rappolt, M., and G. Pabst, 2008. Flexibility and Structure of Fluid Bilayer Interfaces. In K. Nag, editor, *Structure and Dynamics of Membranous Interfaces*, John Wiley & Sons, Inc., 45–81.
- [176] Pabst, G., R. Koschuch, B. Pozo-Navas, M. Rappolt, K. Lohner, and P. Laggner, 2003. Structural analysis of weakly ordered membrane stacks. *J. Appl. Crystallogr.* 36:1378–1388.
- [177] Peiser, H. S., 1963. X-Ray Diffraction in Crystals, Imperfect Crystals, and Amorphous Bodies. A. Guinier. Translated from the French edition (Paris, 1956) by Paul Lorrain and Dorothee Sainte-Marie Lorrain. Freeman, San Francisco, 1963. 378 pp. Illus. *Science* 142:1564–1564.
- [178] Heftberger, P., B. Kollmitzer, F. A. Heberle, J. Pan, M. Rappolt, H. Amenitsch, N. Kučerka, J. Katsaras, and G. Pabst, 2013. Global small-angle X-ray scattering data analysis for multilamellar vesicles: the evolution of the scattering density profile model. *J. Appl. Crystallogr.* 47:173–180.
- [179] Kučerka, N., J. D. Perlmutter, J. Pan, S. Tristram-Nagle, J. Katsaras, and J. N. Sachs, 2008. The effect of cholesterol on short- and long-chain monounsaturated lipid bilayers as determined by molecular dynamics simulations and X-ray scattering. *Biophys. J.* 95:2792–2805.
- [180] Greenwood, A. I., S. Tristram-Nagle, and J. F. Nagle, 2006. Partial molecular volumes of lipids and cholesterol. *Chem. Phys. Lipids* 143:1–10.

Bibliography

- [181] Caillé, A., 1972. Remarques sur la diffusion des rayons X dans les smectiques A. *C.R.Acad.Sc.Paris B* 274:891–893.
- [182] Zhang, R., R. M. Suter, and J. F. Nagle, 1994. Theory of the structure factor of lipid bilayers. *Phys. Rev. E* 50:5047–5060.
- [183] Petrache, H. I., N. Gouliarov, S. Tristram-Nagle, R. Zhang, R. M. Suter, and J. F. Nagle, 1998. Interbilayer interactions from high-resolution x-ray scattering. *Phys. Rev. E* 57:7014–7024.
- [184] Fröhlich, T., G. Fritz, N. Freiberger, and O. Glatter, 2004. Structure and order in lamellar phases determined by small-angle scattering. *J. Appl. Crystallogr.* 37:703–710.
- [185] Klauda, J. B., N. Kučerka, B. R. Brooks, R. W. Pastor, and J. F. Nagle, 2006. Simulation-based methods for interpreting X-ray data from lipid bilayers. *Biophys. J.* 90:2796–2807.
- [186] Kučerka, N., Y. Liu, N. Chu, H. I. Petrache, S. Tristram-Nagle, and J. F. Nagle, 2005. Structure of fully hydrated fluid phase DMPC and DLPC lipid bilayers using X-ray scattering from oriented multilamellar arrays and from unilamellar vesicles. *Biophys. J.* 88:2626–2637.
- [187] Kučerka, N., M.-P. Nieh, and J. Katsaras, 2011. Fluid phase lipid areas and bilayer thicknesses of commonly used phosphatidylcholines as a function of temperature. *Biochim. Biophys. Acta.* 1808:2761–2771.
- [188] Seelig, J., H.-U. Gally, and R. Wohlgemuth, 1977. Orientation and flexibility of the choline head group in phosphatidylcholine bilayers. *Biochim. Biophys. Acta.* 467:109–119.
- [189] Luzzati, V., and F. Husson, 1962. The structure of the liquid-crystalline phases of lipid-water systems. *J. Cell. Biol.* 12:207–219.
- [190] Hodzic, A., M. Rappolt, H. Amenitsch, P. Lagner, and G. Pabst, 2008. Differential modulation of membrane structure and fluctuations by plant sterols and cholesterol. *Biophys. J.* 94:3935–3944.
- [191] Wiener, M. C., S. Tristram-Nagle, D. A. Wilkinson, L. E. Campbell, and J. F. Nagle, 1988. Specific volumes of lipids in fully hydrated bilayer dispersions. *Biochim. Biophys. Acta.* 938:135–142.

- [192] Uhríková, D., P. Rybár, T. Hianik, and P. Balgavý, 2007. Component volumes of unsaturated phosphatidylcholines in fluid bilayers: a densitometric study. *Chem. Phys. Lipids* 145:97–105.
- [193] Koenig, B. W., and K. Gawrisch, 2005. Specific volumes of unsaturated phosphatidylcholines in the liquid crystalline lamellar phase. *Biochim. Biophys. Acta.* 1715:65–70.
- [194] Marsh, D., 2010. Molecular volumes of phospholipids and glycolipids in membranes. *Chem. Phys. Lipids* 163:667–677.
- [195] Goldberg, D., 1989. Genetic algorithms in search, optimization, and machine learning. Addison-Wesley Professional, New York.
- [196] Press, W. H., S. A. Teukolsky, W. A. Vetterling, and B. P. Flannery, 2007. Numerical recipes 3rd edition: The art of scientific computing. Cambridge University Press, Cambridge.
- [197] Rajpaul, V., 2012. Genetic algorithms in astronomy and astrophysics. *arXiv:1202.1643* Proceedings of SAIP2011, the 56th Annual Conference of the South African Institute of Physics, pp. 519–524.
- [198] Rakoff, H., 1982. Preparation of fatty acids and esters containing deuterium. *Prog. Lipid Res.* 21:225–254.
- [199] Tulloch, A. P., 1983. Synthesis, analysis and application of specifically deuterated lipids. *Prog. Lipid Res.* 22:235–256.
- [200] Mildner, D. t., and J. M. Carpenter, 1984. Optimization of the experimental resolution for small-angle scattering. *J. Appl. Crystallogr.* 17:249–256.
- [201] Jacrot, B., 1976. The study of biological structures by neutron scattering from solution. *Rep. Prog. Phys.* 39:911.
- [202] Heftberger, P., B. Kollmitzer, A. Rieder, H. Amenitsch, and G. Pabst, 2015. In Situ Determination of Structure and Fluctuations of Coexisting Fluid Membrane Domains. *Biophys. J.* 108:854–862.

Bibliography

- [203] Buboltz, J. T., C. Bwalya, K. Williams, and M. Schutzer, 2007. High resolution mapping of phase behavior in a ternary lipid mixture: Do lipid-raft phase boundaries depend on sample-prep procedure? *arXiv:0706.1374 [physics]* .
- [204] Pan, J., S. Tristram-Nagle, and J. F. Nagle, 2009. Effect of cholesterol on structural and mechanical properties of membranes depends on lipid chain saturation. *Phys. Rev. E* 80:021931.
- [205] Ohvo-Rekilä, H., B. Ramstedt, P. Leppimäki, and J. Peter Slotte, 2002. Cholesterol interactions with phospholipids in membranes. *Prog. Lipid Res.* 41:66–97.
- [206] McConnell, H. M., and A. Radhakrishnan, 2003. Condensed complexes of cholesterol and phospholipids. *Biochim. Biophys. Acta* 1610:159–173.
- [207] Pabst, G., H. Amenitsch, D. P. Kharakoz, P. Laggner, and M. Rappolt, 2004. Structure and fluctuations of phosphatidylcholines in the vicinity of the main phase transition. *Phys. Rev. E* 70:021908.
- [208] Pabst, G., J. Katsaras, V. A. Raghunathan, and M. Rappolt, 2003. Structure and interactions in the anomalous swelling regime of phospholipid bilayers. *Langmuir* 19:1716–1722.
- [209] Akimov, S. A., P. I. Kuzmin, J. Zimmerberg, and F. S. Cohen, 2007. Lateral tension increases the line tension between two domains in a lipid bilayer membrane. *Phys. Rev. E* 75:011919.
- [210] Ackerman, D. G., and G. W. Feigenson, 2015. Multiscale Modeling of Four-Component Lipid Mixtures: Domain Composition, Size, Alignment, and Properties of the Phase Interface. *J. Phys. Chem. B* .
- [211] García-Sáez, A. J., S. Chiantia, and P. Schwille, 2007. Effect of Line Tension on the Lateral Organization of Lipid Membranes. *J. Biol. Chem.* 282:33537–33544.
- [212] Travasset, A., 2006. Effect of dipolar moments in domain sizes of lipid bilayers and monolayers. *J. Chem. Phys.* 125:084905.

- [213] Hu, J., T. Weikl, and R. Lipowsky, 2011. Vesicles with multiple membrane domains. *Soft Matter* 7:6092–6102.
- [214] Ursell, T. S., W. S. Klug, and R. Phillips, 2009. Morphology and interaction between lipid domains. *Proc. Natl. Acad. Sci. U.S.A.* 106:13301–13306.
- [215] Semrau, S., T. Idema, T. Schmidt, and C. Storm, 2009. Membrane-Mediated Interactions Measured Using Membrane Domains. *Biophys. J.* 96:4906–4915.
- [216] Rozovsky, S., Y. Kaizuka, and J. T. Groves, 2005. Formation and Spatio-Temporal Evolution of Periodic Structures in Lipid Bilayers. *J. Am. Chem. Soc.* 127:36–37.
- [217] Kučerka, N., B. W. Holland, C. G. Gray, B. Tomberli, and J. Katsaras, 2012. Scattering density profile model of POPG bilayers as determined by molecular dynamics simulations and small-angle neutron and X-ray scattering experiments. *J. Phys. Chem. B* 116:232–239.
- [218] Kučerka, N., J. Pencer, J. N. Sachs, J. F. Nagle, and J. Katsaras, 2007. Curvature effect on the structure of phospholipid bilayers. *Langmuir* 23:1292–1299.
- [219] Smith, A. K., and J. H. Freed, 2009. The determination of tie-line fields for coexisting lipid phases: an ESR study. *J. Phys. Chem. B* 113:3957–3971.
- [220] Farkas, E. R., and W. W. Webb, 2010. Precise and millidegree stable temperature control for fluorescence imaging: Application to phase transitions in lipid membranes. *Rev. Sci. Instrum.* 81.
- [221] Kollmitzer, B., P. Heftberger, M. Rappolt, and G. Pabst, 2013. Monolayer spontaneous curvature of raft-forming membrane lipids. *Soft Matter* 9:10877.
- [222] Sapp, K., and L. Maibaum, 2015. The Effect of Lipid Bilayers on Membrane-Bound Proteins. *Biophys. J.* 108:77a.

Appendix A.

First author papers

Heftberger, P., B. Kollmitzer, F. A. Heberle, J. Pan, M. Rappolt, H. Amenitsch, N. Kučerka, J. Katsaras, and G. Pabst, 2013. Global small-angle X-ray scattering data analysis for multilamellar vesicles: the evolution of the scattering density profile model. *J. Appl. Crystallogr.* 47:173–180.

P. Heftberger implemented the global SAXS/SANS data analysis technique, designed and performed the SAXS experiments, did the data reduction and analysis, and wrote the manuscript as well as the supplementary information. B. Kollmitzer and G. Pabst were involved in SAXS experiments and data reduction, discussed results and wrote the paper. F.A. Heberle performed the SANS experiments on POPC including SANS data reduction and wrote the paper. J. Pan and N. Kučerka provided tools to set-up the analysis. M. Rappolt and H. Amenitsch performed experiments. J. Katsaras wrote the paper.

Heftberger, P., B. Kollmitzer, A. Rieder, H. Amenitsch, and G. Pabst, 2015. In Situ Determination of Structure and Fluctuations of Coexisting Fluid Membrane Domains. *Biophys. J.* 108:854–862.

P. Heftberger and B. Kollmitzer designed and performed the SAXS experiments including sample preparation and data reduction. P. Heftberger developed and implemented the SAXS data analysis, performed lipid volume measurements by dilatometry, analyzed and interpreted the SAXS data, and wrote the manuscript as well as the supplementary information. A.Rieder, H. Amenitsch and G. Pabst performed experiments. G. Pabst and B. Kollmitzer took part in discussions about data analysis and interpretation, and wrote the paper.

Appendix B.

Co-authored papers

Khelashvili, G., B. Kollmitzer, P. Heftberger, G. Pabst, and D. Harries, 2013. Calculating the bending modulus for multicomponent lipid membranes in different thermodynamic phases. *J. Chem. Theory Comput.* 9:3866–3871.

Kollmitzer, B., P. Heftberger, M. Rappolt, and G. Pabst, 2013. Monolayer spontaneous curvature of raft-forming membrane lipids. *Soft Matter* 9:10877.

Kollmitzer, B., P. Heftberger, R. Podgornik, J. F. Nagle and G. Pabst, 2015. Bending rigidities and interdomain forces in membranes with coexisting lipid domains. *arXiv [cond-mat, physics:physics]* 1502.07472

Appendix C.

Scientific publications

Global small-angle X-ray scattering data analysis for multilamellar vesicles: the evolution of the scattering density profile model

Peter Heftberger,^a Benjamin Kollmitzer,^a Frederick A. Heberle,^b Jianjun Pan,^{b,c} Michael Rappolt,^{d,e} Heinz Amenitsch,^d Norbert Kučerka,^f John Katsaras^{b,g,h,i} and Georg Pabst^{a*}

^aInstitute of Molecular Biosciences, Biophysics Division, University of Graz, Austria, ^bBiology and Soft Matter Division, Oak Ridge National Laboratory, Oak Ridge, TN, USA, ^cDepartment of Physics, University of South Florida, Tampa, FL 33620, USA, ^dInstitute of Inorganic Chemistry, Graz University of Technology, Austria, ^eSchool of Food Science and Nutrition, University of Leeds, UK, ^fCanadian Neutron Beam Centre, National Research Council, Chalk River, ON, Canada, ^gJoint Institute for Neutron Sciences, Oak Ridge, TN, USA, ^hDepartment of Physics and Astronomy, University of Tennessee, Knoxville, TN, USA, and ⁱDepartment of Physics, Brock University, St Catharines, ON, Canada. Correspondence e-mail: georg.pabst@uni-graz.at

The highly successful scattering density profile (SDP) model, used to jointly analyze small-angle X-ray and neutron scattering data from unilamellar vesicles, has been adapted for use with data from fully hydrated, liquid crystalline multilamellar vesicles (MLVs). Using a genetic algorithm, this new method is capable of providing high-resolution structural information, as well as determining bilayer elastic bending fluctuations from standalone X-ray data. Structural parameters such as bilayer thickness and area per lipid were determined for a series of saturated and unsaturated lipids, as well as binary mixtures with cholesterol. The results are in good agreement with previously reported SDP data, which used both neutron and X-ray data. The inclusion of deuterated and non-deuterated MLV neutron data in the analysis improved the lipid backbone information but did not improve, within experimental error, the structural data regarding bilayer thickness and area per lipid.

1. Introduction

Phospholipids are a major component of biological membranes, and the structural analysis of pure lipid membranes is an important area of research, as it can provide valuable insights into membrane function, including how the membrane's mechanical properties affect lipid/protein interactions (Escribá *et al.*, 2008; Mouritsen, 2005). Of the liquid crystalline mesophases formed by phospholipids in aqueous solutions, most effort has been expended in studying fluid bilayers (L_α), because of their commonly accepted biological significance.

Over the years, scattering techniques such as small-angle X-ray and neutron scattering (SAXS and SANS) have been widely used to determine the structural parameters and mechanical properties of biomimetic membranes. With regard to bilayer structure, two important structural parameters are bilayer thickness and lateral area per lipid A (Lee, 2004; Pabst *et al.*, 2010; Heberle *et al.*, 2012); the latter is directly related to lipid volume and inversely proportional to bilayer thickness. Importantly, A plays a key role in the validation of molecular dynamics (MD) simulations (Klauda *et al.*, 2006), and as such, its value for different lipids must be accurately known.

Historically, for a given lipid, a range of values for A have been reported (Kučerka *et al.*, 2007). Since lipid volumes are determined from independent and highly accurate densitometry measurements (Nagle & Tristram-Nagle, 2000; Greenwood *et al.*, 2006; Uhríková *et al.*, 2007), differences in A must therefore result from differences in bilayer thickness. To accurately determine lipid areas, a precise measure of the Luzzati thickness d_B (Luzzati & Husson, 1962), which is given by the Gibbs dividing surface of the water/bilayer interface (Kučerka, Nagle *et al.*, 2008), is needed. Other frequently used definitions of bilayer thickness are the headgroup-to-headgroup thickness d_{HH} and the steric bilayer thickness (Pabst, Katsara *et al.*, 2003). The latter two bilayer thicknesses can also be used to determine A ; however, assumptions regarding the headgroup size or the distance to the chain/headgroup interface have to be made.

There are two important issues that one must consider when measuring membrane thickness. Firstly, owing to the thermal disorder of fluid bilayers, there is no distinct division between lipids and water; instead a water concentration gradient exists at the membrane's interface. Secondly, X-rays and neutrons are sensitive to different parts of the bilayer. X-rays, for example, are strongly scattered from the electron-dense

phosphate group, which is part of the phosphorylcholine headgroup, and hence accurate values for d_{HH} can be obtained. On the other hand, neutrons are scattered by atomic nuclei and can be used for contrast variation analyses, since hydrogen and its isotope deuterium scatter neutrons with similar efficiencies but 180° out-of-phase with each other (*i.e.* deuterium's coherent scattering length is positive, while hydrogen's is negative). In the case of protiated lipid bilayers, SANS is highly sensitive to locating the hydrogen-depleted carbonyl groups. Importantly, however, neutron contrast can be easily tuned by varying the hydrogen–deuterium content of the water (by varying the $\text{H}_2\text{O}/\text{D}_2\text{O}$ ratio) or of the bilayer (through the use of deuterated lipids) (Pabst *et al.*, 2010). As mentioned, in the case of protiated lipid bilayers in 100% D_2O , neutrons are most sensitive to the lipid's glycerol backbone. Moreover, the Gibbs dividing surface for the apolar/polar interface is typically located between the headgroup phosphate and the lipid backbone. Therefore a combined analysis of X-ray and neutron data should yield the most accurate values of d_{B} and A (Kučerka, Nagle *et al.*, 2008; Kučerka *et al.*, 2011; Pan, Heberle *et al.*, 2012). In this combined data analysis, commonly known as the scattering density profile (SDP) model, the lipid bilayer is represented by volume distributions of quasi-molecular fragments, which are easily converted into electron density or neutron scattering length density distributions by scaling them (for a given molecular group) with the appropriate electron or neutron scattering length density [see Heberle *et al.* (2012) for a recent review].

Scattering techniques are also capable of probing membrane elasticity. Lipid bilayers are two-dimensional fluids which exhibit significant bending fluctuations of entropic origin. In multilamellar arrangements, *e.g.* in liquid crystalline multilamellar vesicles (MLVs) or surface-supported multibilayers, this leads to a characteristic power-law decay of the positional correlation function, known as quasi-long-range order, with Bragg peaks having characteristic line shapes (Liu & Nagle, 2004; Salditt, 2005; Pabst *et al.*, 2010). Membrane elasticity can therefore be determined from line-shape analysis of the Bragg peaks, and the underlying physics of this phenomenon is described by the Caillé (1972) or modified Caillé theory (MCT) (Zhang *et al.*, 1994). The resulting fluctuation, or Caillé parameter η , is a function of the bilayer bending modulus and the bulk modulus of interbilayer compression. Owing to the higher-resolution data, compared to neutrons, X-rays are better suited for line-shape analysis of Bragg peaks.

Just over a decade ago, Pabst and co-workers were the first to report a full- q -range analysis of MLV SAXS data using MCT (Pabst *et al.*, 2000; Pabst, Koschuch *et al.*, 2003). In that method, quasi-Bragg peaks and diffuse scattering were both taken into account when analyzing the data, and the electron density profile was modeled by a simple summation of Gaussians representing the electron-rich lipid headgroup and electron-poor (in relation to the headgroup) hydrocarbon chains. Selected examples of this SAXS method of data analysis can be found in the recent reviews by Pabst *et al.* (2010, 2012).

The work described here extends the global analysis program (GAP; Pabst *et al.*, 2000; Pabst, Koschuch *et al.*, 2003) for MLVs, by making use of the SDP description of the lipid bilayer. This modified technique, termed herein the SDP–GAP model, has several advantages. Firstly, compared to extruded unilamellar vesicles (ULVs), spontaneously forming MLVs are easier to prepare (Heberle *et al.*, 2012). Secondly, the SDP description of the bilayer imparts to GAP the ability to simultaneously analyze SANS and SAXS data, while enabling the SDP model to determine bending fluctuations and, hence, bilayer interactions.

In the present study we also attempted to determine precise values of d_{B} and A using standalone X-ray data. Such analysis, however, is complicated by the use of an increased number of fitting parameters, as compared to GAP, and inherently less scattering contrast, as compared to the SDP model, which simultaneously makes use of SANS and SAXS data. To address these shortcomings we used a genetic algorithm, as an optimization routine, in combination with information from other sources, thereby reducing the number of parameters needed by the SDP–GAP model. To test the new SDP–GAP model, we analyzed a series of saturated and unsaturated phospholipids, as well as binary lipid mixtures with cholesterol. The results compare favorably with previously reported data obtained using the SDP model, including the commonly accepted bilayer condensation effect induced by cholesterol. We also include SANS data of protiated and deuterated palmitoyl-oleoyl phosphatidylcholine (POPC) in our analysis, which gives rise to a better resolved location of the lipid's glycerol backbone. Compared to standalone SAXS analysis, any differences in the values of A and d_{B} obtained from SDP–GAP model analysis are well within experimental uncertainty.

2. Material and methods

2.1. Sample preparation

1,2-Dipalmitoyl-*sn*-glycero-3-phosphocholine (DPPC), 1-palmitoyl-2-oleoyl-*sn*-glycero-3-phosphocholine (POPC), 1-palmitoyl(d31)-2-oleoyl-*sn*-glycero-3-phosphocholine (POPC-d31), 1-stearoyl-2-oleoyl-*sn*-glycero-3-phosphocholine (SOPC) and 1,2-dioleoyl-*sn*-glycero-3-phosphocholine (DOPC) were purchased from Avanti Polar Lipids, Alabaster, AL, USA, and cholesterol was obtained from Sigma–Aldrich (Austria). 99.8% D_2O was obtained from Alfa Aesar (Ward Hill, MA, USA). All lipids were used without further purification.

For X-ray experiments, lipid stock solutions (DPPC, POPC, SOPC, DOPC) were prepared by dissolving predetermined amounts of dry lipids in chloroform/methanol (2:1, v/v). Binary mixtures with cholesterol (20 mol%) were obtained by mixing lipid stock solutions in the appropriate ratios. Lipid solutions were subsequently dried under a stream of nitrogen and placed under vacuum for about 12 h, forming a thin lipid film on the bottom of glass vials. Films were hydrated using $18\text{ M}\Omega\text{ cm}^{-1}$ water by incubation for 2 h above the lipid melting temperature, with vortex mixing every 15 min. The final lipid concentration for each sample was 50 mg ml^{-1} .

For neutron experiments, MLVs of POPC-d31 at 10 mg ml^{-1} were prepared by weighing 15 mg of dry lipid powder into $13 \times 100 \text{ mm}$ glass culture tubes and hydrating with 1.50 ml D_2O preheated to 313 K, followed by vigorous vortexing to disperse the lipid. The resultant MLV suspension was incubated at 313 K for 1 h, with intermittent vortexing, and then subjected to five freeze/thaw cycles between 193 and 313 K to reduce the average number of lamellae and facilitate extrusion (Kaaagaard *et al.*, 2003; Mayer *et al.*, 1985). A 0.75 ml aliquot of the MLV sample was used to prepare ULVs using a hand-held miniextruder (Avanti Polar Lipids, Alabaster, AL, USA) assembled with a 50 nm-pore-diameter polycarbonate filter and heated to 313 K. The suspension was passed through the filter 41 times. ULV samples were measured within 24 h of extrusion. The final sample concentrations were 10 mg ml^{-1} , which allows for sufficient water between vesicles to eliminate the interparticle structure factor, thereby simplifying data analysis.

2.2. Small-angle X-ray scattering

X-ray scattering data were acquired at the Austrian SAXS beamline, which is situated at the Elettra synchrotron (Trieste, Italy), using 8 keV photons. Diffraction profiles were detected utilizing a Mar300 image-plate detector (Marresearch GmbH, Norderstedt, Germany) and calibrated using a powder sample of silver behenate. Lipid dispersions were taken up in 1 mm-thick quartz capillaries and inserted into a multi-position sample holder. Samples were equilibrated for a minimum of 10 min prior to measurement at a predetermined temperature with an uncertainty of $\pm 0.1 \text{ K}$ using a circulating water bath. The exposure time was set to 240 s. Scattering patterns were integrated using the program *FIT2D* (Hammersley, 1997). Background scattering originating from water and air was subtracted, and data sets were normalized using the transmitted intensity, which was measured by a photodiode placed in the beamstop.

2.3. Small-angle neutron scattering

Neutron scattering experiments were performed using the Extended- Q -range Small-Angle Neutron Scattering (EQ-SANS, BL-6) instrument at the Spallation Neutron Source (SNS) located at Oak Ridge National Laboratory (ORNL). ULVs were loaded into 2 mm-path-length quartz banjo cells (Hellma USA, Plainview, NY, USA) and mounted in a temperature-controlled cell paddle with a 1 K accuracy. In 60 Hz operation mode, a 4 m sample-to-detector distance with a 2.5–6.1 Å wavelength band was used to obtain the relevant wavevector transfer. Scattered neutrons were collected with a two-dimensional ($1 \times 1 \text{ m}$) ^3He position-sensitive detector made up of 192×256 pixels. Two-dimensional data were reduced using *MantidPlot* (<http://www.mantidproject.org/>). During data reduction, the measured scattering intensity was corrected for detector pixel sensitivity, dark current, sample transmission, and background scattering contribution from the water and empty cell. The one-dimensional scattering

intensity, I versus q , was obtained by radial averaging of the corrected two-dimensional data.

2.4. Modeling of phospholipid bilayer

To analyze the scattering profile of MLVs, we adopted the full- q -range GAP model of Pabst and co-workers (Pabst *et al.*, 2000; Pabst, Koschuch *et al.*, 2003), which takes into account diffuse scattering N_{diff} originating from positionally uncorrelated bilayers):

$$I(q) = (1/q^2) \left[|F(q)|^2 S(q) (1 - N_{\text{diff}}) + |F(q)|^2 N_{\text{diff}} \right], \quad (1)$$

where the scattering vector magnitude $q = 4\pi \sin \theta / \lambda$, λ is the wavelength, 2θ is the scattering angle relative to the incident beam, $F(q)$ is the bilayer form factor and $S(q)$ is the inter-bilayer structure factor. For fluid lipid bilayers, $S(q)$ is given by the Caillé theory, which is described in detail elsewhere (Caillé, 1972; Zhang *et al.*, 1994; Pabst *et al.*, 2000; Pabst, Koschuch *et al.*, 2003). Averaging over variations in scattering domain size was performed following Frühwirth *et al.* (2004). One of the important parameters determined from fitting $S(q)$ using MCT is the Caillé parameter η , which is a measure of bending fluctuations (Pabst *et al.*, 2010). The number of positionally correlated bilayers N_{mean} affects the width of the Bragg peaks (Pabst, Koschuch *et al.*, 2003) and must be optimized through fitting of the data. In the case of the present samples, the number of bilayers N_{mean} contributing to Bragg scattering varied between ten and 30. Instrumental resolution was taken into account by convoluting equation (1) with the beam profile (Pabst *et al.*, 2000; Qian & Heller, 2011), and incoherent background scattering was accounted for by an additive constant.

The form factor is the Fourier transform of the electron density or neutron scattering length density profile. In the present study, we implemented the SDP model (Kučerka, Nagle *et al.*, 2008) to describe the bilayer. The SDP model describes the membrane in terms of the volume distributions of quasi-molecular fragments. A detailed description of volume probability distribution functions is given in the article by Kučerka, Nagle *et al.* (2008). The water-subtracted scattering length density distributions $[\Delta\rho(z)]$ are calculated by scaling the volume probability distributions using component total electron densities (for X-rays) or neutron scattering length densities. The form factor is then calculated as

$$F(q) = \int \Delta\rho(z) \exp(-iqz) dz. \quad (2)$$

Kučerka and co-workers originally parsed phosphatidylcholines into the following components: choline methyl (CholCH_3); phosphate + $\text{CH}_2\text{CH}_2\text{N}$ (PCN); carbonyl + glycerol (CG); hydrocarbon methylene (CH_2); and hydrocarbon terminal methyl (CH_3). An additional methine (CH) group was added for unsaturated hydrocarbon chains. However, the contrast between CH and CH_2 is weak, even for SANS (Kučerka, Nagle *et al.*, 2008), and effectively zero for SAXS. Hence, our parsing scheme combined the CH with the CH_2 group (Fig. 1).

To avoid nonphysical results, the following constraints were adopted following Klauda *et al.* (2006) and Kučerka, Nagle *et al.* (2008). Because of bilayer symmetry, the position of the terminal methyl group z_{CH_3} was set to zero and the height of the error function, which describes the hydrocarbon chains, was set to one in order to comply with spatial conservation. The width of the choline methyl group σ_{CholCH_3} was fixed to 2.98 Å, and the width of the error function describing the hydrocarbon chain was constrained within accepted limits ($\sigma_{\text{HC}} \in [2.4, 2.6]$ Å) (Klauda *et al.*, 2006; Kučerka, Nagle *et al.*, 2008).

We also implemented new constraints to aid the standalone X-ray data analysis. Firstly, the distances between the CholCH₃ and PCN groups, and the hydrocarbon chain interface (z_{HC}) and CG (z_{CG}) groups, were not allowed to exceed 2 Å because of their spatial proximity. Secondly, volumes of the quasi-molecular fragments, necessary for calculating electron or neutron scattering length densities, were taken from previous reports (Kučerka *et al.*, 2005, 2011; Kučerka, Nagle *et al.*, 2008; Klauda *et al.*, 2006; Greenwood *et al.*, 2006) and allowed to vary by $\pm 20\%$. The total volume of the headgroup components (*i.e.* CholCH₃, PCN and CG) was constrained to a target value of 331 Å³, as reported by Trisram-Nagle *et al.* (2002), whereby the value is allowed to deviate from the target value, but in doing so, incurs a goodness-of-fit penalty.

For lipid mixtures with cholesterol, cholesterol's volume distribution was merged with that of the CH₂ group, following Pan, Cheng *et al.* (2012). This is justified on the basis of cholesterol's strong hydrophobic tendency, which dictates its location within the hydrocarbon chain region, and the fact that its hydroxy group resides in the vicinity of the apolar/polar interface (Pan, Cheng *et al.*, 2012). In calculating the lipid area for binary mixtures, the apparent area per lipid $A = 2V_L/d_B$

was used (Pan, Cheng *et al.*, 2012; Pan *et al.*, 2009). The volume of cholesterol within lipid bilayers was taken to be 630 Å³ (Greenwood *et al.*, 2006).

2.5. Determination of structural parameters

On the basis of volume probability distributions and scattering length density profiles, membrane structural parameters were defined as follows: (i) the headgroup-to-headgroup distance d_{HH} is the distance between maxima of the total electron density (*i.e.* the sum of the component distributions); (ii) the hydrocarbon chain length d_C is the position of the error function representing the hydrocarbon region z_{HC} ; and (iii) the Luzzati thickness d_B is calculated from the integrated water probability distribution (Kučerka, Nagle *et al.*, 2008):

$$d_B = d - 2 \int_0^{d/2} P_W(z) dz, \quad (3)$$

where d is the lamellar repeat distance. The volume distribution function of water was previously defined as (Kučerka, Nagle *et al.*, 2008)

$$P_W(z) = 1 - \sum P_i(z), \quad (4)$$

where i indexes the lipid component groups (*i.e.* CholCH₃, PCN, CG, CH₂ and CH₃). In order to increase the robustness of the analysis for d_B , P_W obtained from the SDP analysis was fitted with an error function, thus giving greater weight to the region close to the lipid headgroup (owing to the higher X-ray contrast) compared to the hydrocarbon chain region. We also attempted to include the P_W model function in the SDP fit; however, the results were not satisfactory. The area per lipid is then given by (Kučerka, Nagle *et al.*, 2008)

$$A = 2V_L/d_B, \quad (5)$$

where V_L is the molecular lipid volume determined by separate experiments. Finally, the thickness of the water layer was defined as

$$d_W = d - d_B. \quad (6)$$

2.6. Fitting procedure

Owing to the large number of adjustable parameters (*i.e.* 21) and our goal to apply the SDP-GAP model to standalone X-ray data, we chose to use a genetic algorithm in the optimization routine. The main benefit of this algorithm, compared to simple gradient descent routines or more sophisticated optimization algorithms (*e.g.* Levenberg-Marquardt), is that the fitting procedure does not easily fall into local minima (Goldberg, 1989). Briefly, a random set of adjustable parameters (termed a population) is chosen within fixed boundaries and tested for its fitness, defined here as the reduced chi squared (χ^2) value, which is equal to the sum of the squared residuals divided by the degrees of freedom (Press *et al.*, 2007). The best solutions are then combined to obtain a new and better population, in a manner similar to the evolutionary process of genetic recombination [for details, see Goldberg (1989)]. Several hundred generations with popula-

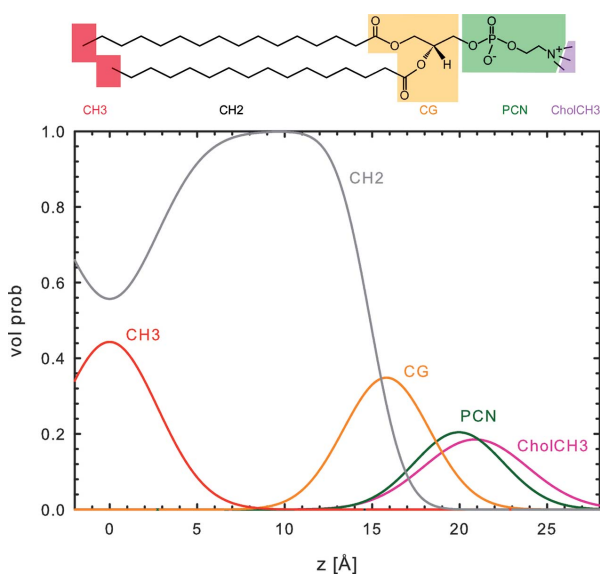


Figure 1 Illustration of the bilayer parsing scheme (top panel) and volume probability distribution (bottom panel) for DPPC. Data are from experiments carried out in the present study.

tions of ~2000 individuals were tested for their fitness. If χ^2 does not change after 100 generations, the optimization is assumed to have converged and the routine is terminated. Solutions with the lowest χ^2 values are then compared with respect to differences in structural parameters. From the resulting distributions we estimate that the uncertainty of all parameters reported in the present work is $\leq \pm 2\%$. Application of genetic algorithms comes with a greater computational cost, and they are most efficient when using parallel processing techniques. For the present study, all routines were encoded in IDL (Interactive Data Language), using the *SOLBER* optimization routine (Rajpaul, 2012). Typical runtimes for one X-ray scattering profile were between three and five hours on a six core machine (Intel Xeon 2.67 GHz).

3. Results and discussion

3.1. X-ray standalone data

The SDP-GAP model was tested on SAXS data obtained from single component L_α lipid bilayers and selected binary

Table 1

Comparison of structural parameters.

Parameter uncertainties are estimated to be $<2\%$ as described in *Materials and methods*.

		SDP-GAP	GAP	SDP†
DPPC (323 K)	A (\AA^2)	63.1	61.8	63.1
	d_B (\AA)	39.0	n.a.	38.9
	d_{HH} (\AA)	37.9	37.3	38.4
	d_C (\AA)	13.9	14.5	14.2
	η	0.08	0.067	n.a.
POPC (303 K)	A (\AA^2)	65.4	64.3	64.4
	d_B (\AA)	38.4	n.a.	39.0
	d_{HH} (\AA)	37.3	37.0	36.5
	d_C (\AA)	14.0	14.4	14.4
	η	0.06	0.056	n.a.
SOPC (303 K)	A (\AA^2)	66.3	60.3	65.5
	d_B (\AA)	39.5	n.a.	40.0
	d_{HH} (\AA)	38.7	40.7	38.6
	d_C (\AA)	14.6	16.2	15.0
	η	0.06	0.08	n.a.
DOPC (303 K)	A (\AA^2)	67.6	69.7	67.4
	d_B (\AA)	38.5	n.a.	38.7
	d_{HH} (\AA)	36.9	36.1	36.7
	d_C (\AA)	14.2	13.9	14.4
	η	0.1	0.1	n.a.

† From Kučerka, Nagle *et al.* (2008) and Kučerka *et al.* (2011).

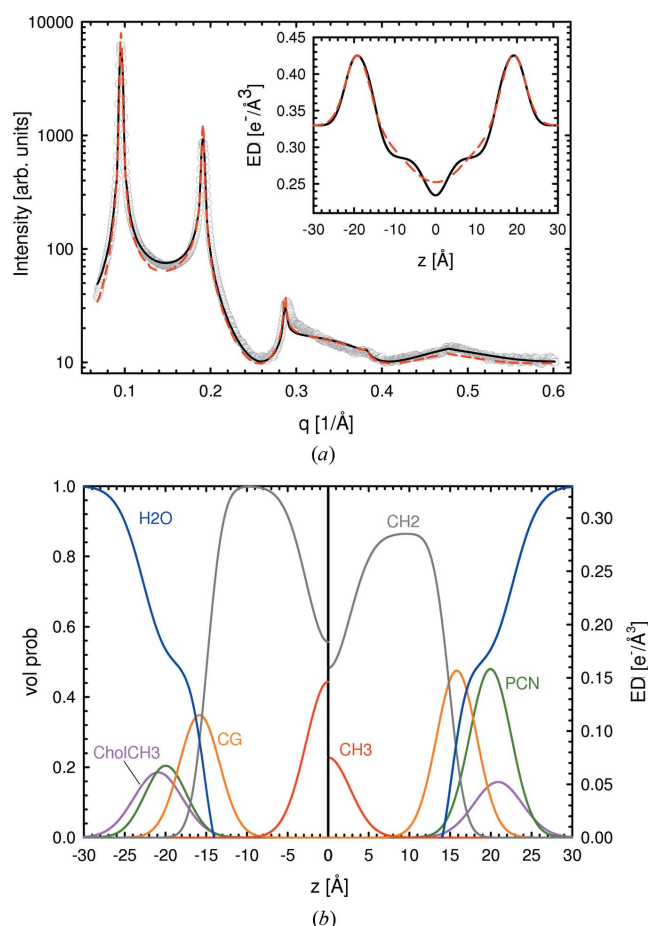


Figure 2
SDP-GAP analysis of SOPC MLVs at 303 K. Panel (a) compares the SDP-GAP (black line) and GAP models (red dashed line) with experimental data (grey circles). The inset to the figure compares the corresponding electron density profiles. Panel (b) shows the volume probability distribution (left hand side) and the electron density distributions of the defined quasi-molecular fragments (right hand side).

mixtures of phosphatidylcholines with cholesterol. As an example of our analysis, we present results for SOPC bilayers with five lamellar diffraction orders (Fig. 2). Fits from all other bilayers, including tables with structural parameters, are given in the supporting material (Figs. S1–S3, Table S1).¹ All SAXS patterns showed significant diffuse scattering, originating from membrane fluctuations common to L_α bilayers. In particular, bending fluctuations lead to a rapid decrease in diffraction peak amplitudes as a function of q , and quasi-Bragg peaks with characteristic line shapes. Such effects are accounted for in the structure factor used. We found good agreement between the SDP-GAP model and experimental SOPC data ($\chi^2 = 0.78$). Fits from other MLV systems yielded similar χ^2 values (Table S1). Omitting the constraints introduced in §2.4 led to slightly improved χ^2 values but produced nonphysical results.

Results from the SDP-GAP model were compared with those from the GAP model. The GAP data were in reasonable agreement with the experimental data (Fig. 2), albeit with poorer fit statistics ($\chi^2 = 4.78$), which could be attributed to the small deviations of the model between the various Bragg peaks. Despite the good fits produced using the GAP model, the structural features obtained from SDP-GAP analysis are significantly richer (Fig. 2, lower panel). This point is illustrated by the total electron density shown in the inset to Fig. 2, where the methyl trough is smeared out in the GAP electron density profile.

Table 1 provides the main structural parameters obtained from SDP-GAP and GAP analyses of the same data, as well as literature values obtained from SDP analysis (*i.e.* joint

¹ Supporting information for this article is available from the IUCr electronic archives (Reference: FS0506).

refinement of SAXS and SANS data). The calculation of structural parameters using the GAP model is detailed by Pabst, Katsaras *et al.* (2003). Our results using the SDP-GAP model are in good quantitative agreement with the reference data. Deviations from the GAP model are, however, larger (though still reasonable) because of the simplified electron density model that was used. Interestingly, in the case of some lipids, we also find significant differences for the fluctuation parameter; these are attributable to the form factor, which modulates peak intensity. It therefore stands to reason that the better fits to the experimental data by the SDP-GAP model should result in more accurate η values.

We further tested the SDP-GAP model using the same lipid systems, but this time with the addition of 20 mol% cholesterol. Cholesterol is abundant in mammalian plasma membranes and is well known for the condensing effect it has on lipid bilayers, which at the molecular level is explained by the umbrella model (Huang & Feigenson, 1999). In scattering studies, this effect shows up as an increase in d_B and a concomitant decrease in A , as well as in reduced bending fluctuations (see *e.g.* Hodzic *et al.*, 2008). Fig. 3 shows the fits to SOPC/cholesterol membrane data. The SDP-GAP model is able to describe the better resolved higher diffraction orders

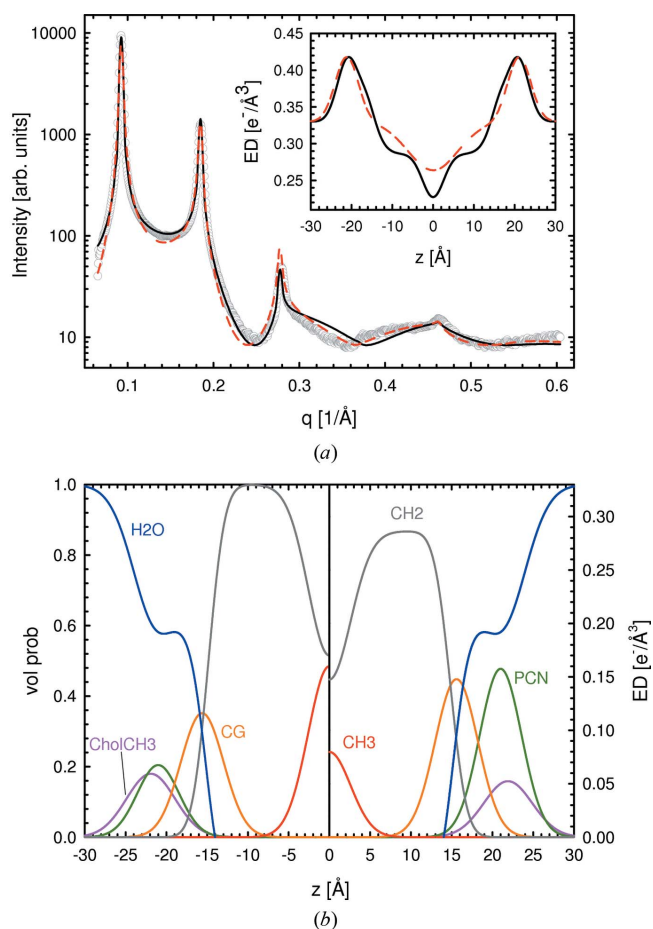


Figure 3 Comparing SDP-GAP and GAP fits to data from SOPC MLVs, with 20 mol% cholesterol at 303 K. The meaning of the lines is the same as in Fig. 2.

Table 2

Structural parameters from the SDP-GAP model of lipid bilayers containing 20 mol% cholesterol.

Parameter uncertainties are estimated to be <2% as described in *Materials and methods*.

Lipid	A (Å ²)	d_B (Å)	d_{HH} (Å)	d_C (Å)	η
DPPC (323 K)	61.2	40.1	42.3	14.2	0.02
POPC (303 K)	63.1	39.8	40.3	14.3	0.05
SOPC (303 K)	60.6	40.5	42.1 (42.1)†	14.9 (16.1)†	0.05
DOPC (303 K)	66.2	39.4	40.9 (39.0)†	13.5 (14.6)†	0.14

† From Pan *et al.* (2009).

resulting from the presence of cholesterol. Our results show that cholesterol shifts the PCN and CholCH₃ groups further away from the bilayer center (Fig. 3, bottom panel, and Tables 2 and S2), in good agreement with previous reports (Pan, Cheng *et al.*, 2012). On the other hand, we could not observe a significant shift of the CG group from the bilayer center or a higher value for the hydrocarbon chain thickness (Tables 2 and S2).

Structural parameters for all lipid mixtures are reported in Table 2. In agreement with previous reports, the addition of cholesterol causes A to decrease and d_B and d_{HH} to increase (Hung *et al.*, 2007; Kučerka, Perlmutter *et al.*, 2008; Pan *et al.*, 2008; Hodzic *et al.*, 2008; Pan, Cheng *et al.*, 2012). Compared to other membrane systems, bending fluctuations in DPPC bilayers experience a greater degree of damping when cholesterol is introduced, in agreement with the notion that cholesterol preferentially associates with saturated hydrocarbon chains (Pan *et al.*, 2009, 2008; Ohvo-Rekilä *et al.*, 2002). This effect is smaller for lipids having one monounsaturated chain (*i.e.* SOPC and POPC) and is completely absent when a second monounsaturated chain is introduced (*e.g.* DOPC). This latter finding is in good agreement with studies that reported no change in the bending rigidity of DOPC bilayers in the absence or presence of cholesterol (Pan *et al.*, 2008).

SOPC/cholesterol mixtures were also analyzed with the GAP model. Although reasonable fits are obtained (Fig. 3, $\chi^2_{SDP-GAP} = 1.04$, $\chi^2_{GAP} = 3.93$), the differences in structural parameters when comparing GAP data with SDP-GAP data are more pronounced. For example, the total electron density profiles show clear deviations in the acyl chain and headgroup regions. Cholesterol increases the asymmetry of the electron density distribution in the headgroup region, as determined from the SDP-GAP model, an effect that is not captured by the single-headgroup Gaussian of the GAP model. As a result, parameters such as area per lipid ($A_{SDP-GAP} = 60.7$ Å², $A_{GAP} = 57.4$ Å²) and hydrocarbon chain length ($d_{C,SDP-GAP} = 14.9$ Å, $d_{C,GAP} = 17$ Å) differ between the two methods, whereas the values for headgroup-to-headgroup thickness ($d_{HH,SDP-GAP} = 42.1$ Å, $d_{HH,GAP} = 42.3$ Å) and the Caillé parameter ($\eta_{SDP-GAP} = 0.05$, $\eta_{GAP} = 0.04$) are in reasonably good agreement.

3.2. Addition of SANS data

SANS data were obtained from POPC and POPC-d31 MLVs and ULVs in pure D₂O to see whether or not additional

information substantially alters the results. The protocol devised by Kučerka and co-workers used SANS data from protiated bilayers at different H₂O/D₂O contrasts (Kučerka, Nagle *et al.*, 2008).

Replacing H with D shifts the neutron scattering length density (NSLD) profile of the hydrocarbon region from negative to positive values (Fig. 4*b*, inset). Hence, relative to

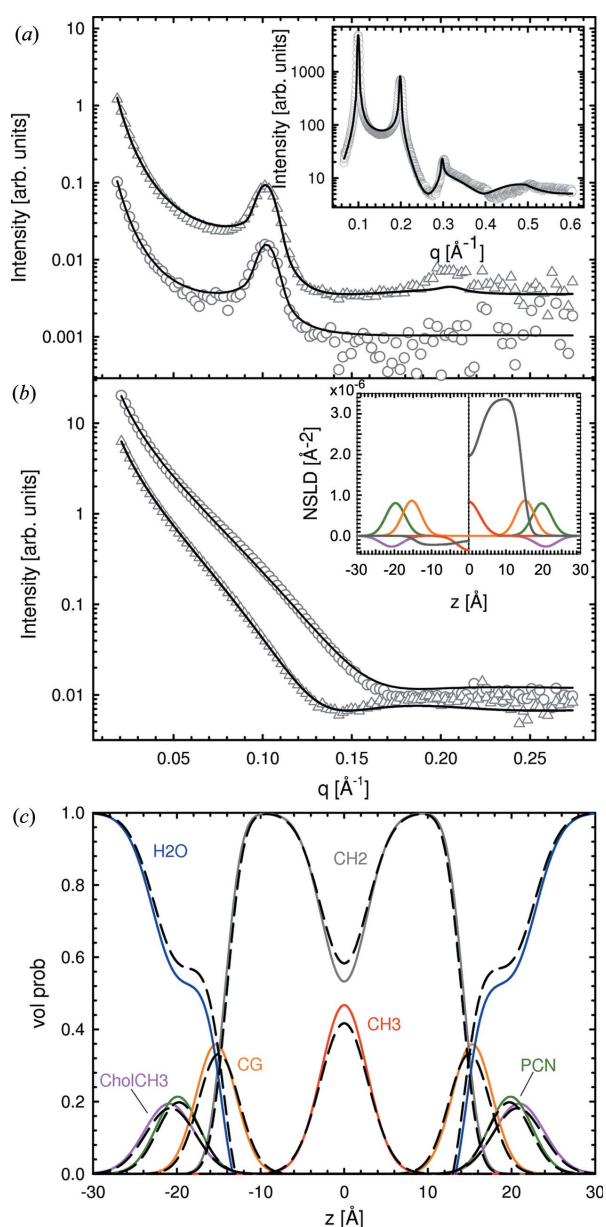


Figure 4
Results of simultaneous SAXS and SANS analysis of data from POPC ULVs and MLVs at 303 K. Panel (a) shows SANS data of POPC (circles) and POPC-d31 (triangles) MLVs, and corresponding data obtained from ULVs (same symbols) are shown in panel (b). Solid lines are best fits to the data using the SDP-GAP model. The insets in panels (a) and (b) show the corresponding SAXS fits and neutron scattering length density profiles for POPC (left) and POPC-d31 (right), respectively. Panel (c) shows the changes in volume distributions from a SAXS-only analysis (dashed black lines) to a simultaneous SAXS/SANS analysis (colored lines; same color coding as in Figs. 2 and 3).

Table 3

Structural parameters for POPC using different combinations of SAXS and SANS data.

Parameter uncertainties are estimated to be <2% as described in *Materials and methods*.

	SAXS†	n-MLV _u ‡	n-MLV _d §	All data¶	SDP††
A (Å ²)	65.4	64.9	63.1	63.6	64.4
d_B (Å)	38.4	38.7	39.8	39.5	39.0
d_{HH} (Å)	37.3	37.1	37.3	37.5	36.5
d_C (Å)	14.0	14.6	14.4	14.3	14.4
z_{CG} (Å)	15.0	15.3	15.4	15.3	15.3

† Results obtained using SAXS data only. ‡ SAXS (POPC-MLV) and SANS (POPC-MLV) data. § SAXS (POPC-MLV) and SANS (POPC-d31-MLV) data. ¶ SAXS (POPC-MLV) and SANS (POPC-ULV/MLV, POPC-d31-ULV/MLV) data. †† From Kučerka *et al.* (2011).

D₂O with an SLD = 6.4×10^{-14} cm Å³, the hydrocarbon chain region contrast is significantly altered. This change in contrast manifested itself by producing two additional Bragg peaks in the case of POPC-d31 MLVs, compared to their protiated counterparts (Fig. 4*a*). Similarly, ULV data show a shift of the minimum at low q to higher q vector magnitudes for POPC compared to POPC-d31 (Fig. 4*b*), which is also attributed to the change in contrast of the deuterated lipids in D₂O.

We used SDP-GAP to simultaneously analyze SAXS data in several combinations with SANS data: (i) protiated MLVs; (ii) deuterated MLVs; and (iii) all four SANS data sets (*i.e.* deuterated and protiated MLVs and ULVs). We also fitted all MLV data sets simultaneously and all ULV data sets separately. Fit results are shown in Fig. 4 and the determined structural parameters are summarized in Tables 3 and S3. The addition of a single SANS data set produced variations in the structural parameters, causing them to deviate from values determined from standalone SAXS analysis and those from the literature. This disagreement was rectified by including either both MLV data sets or all MLV and ULV data sets in the analysis. In the latter case, significant differences, compared to the standalone SAXS analysis, are found regarding the positions of the CG group, z_{CG} and d_C . This can be understood in terms of the better neutron contrast of the lipid backbone. Changes in volume distribution functions are shown in Fig. 4(*c*). The changes to A and d_B are within the experimental error and consequently of no significance. We thus conclude that the addition of SANS data helps to improve the location of the CG group and d_C , but offers little improvement to values of A and d_B .

4. Conclusion

We have modified the full- q -range SAXS data analysis, which previously used a simplified electron density profile (Pabst *et al.*, 2000), with a high-resolution representation of scattering density profiles, based on volume distributions of quasi-molecular fragments (Kučerka, Nagle *et al.*, 2008). The new SDP-GAP method, as its name implies, is a hybrid model that combines advantages offered by the GAP and SDP models. The SDP-GAP model can be used to analyze MLV and ULV data and is capable of simultaneously analyzing SAXS and

SANS data. MLVs are spontaneously formed membrane systems, and the development of this new hybrid model opens up new opportunities for the study of their bilayer interactions and membrane mechanical properties (e.g. elasticity) (Pabst *et al.*, 2010).

An additional feature of this new model is its ability to obtain high-resolution structural information from standalone SAXS data. This is achieved by implementing an optimization routine based on a genetic algorithm, which is able to deal with the large number of adjustable parameters, even though additional constraints and input parameters are required in order to limit parameter space. Compared to the GAP and SDP models, which use Levenberg–Marquardt and downhill simplex optimization routines, respectively, the computational effort required by the SDP–GAP model is significantly higher. Typical CPU times on parallel processors are of the order of a few hours, as compared to a few minutes for SDP or GAP. However, an advantage is that the genetic algorithm prevents the optimization routine from stalling in local minima. By using different seeds for the random number generator, robust results with good convergence are readily obtained.

We have tested the SDP–GAP model using different saturated and unsaturated phosphatidylcholine bilayers, with and without cholesterol. Results for d_B and A are in good agreement with previous reports using the SDP model, although we note that the position and width of the CG group are subject to greater variabilities, as a result of the lower X-ray contrast of this particular group. This inadequacy was, however, ameliorated by including ULV SANS data. MLV SAXS data combined with ULV SANS data of POPC and POPC-d31 bilayers improved both the position of the CG group and the hydrocarbon chain thickness (Fig. 3c and Table 3). However, the values of A and d_B remained practically unchanged.

This work was supported by the Austrian Science Fund FWF, project No. P24459-B20 (to GP). Support was received from the Laboratory Directed Research and Development Program of Oak Ridge National Laboratory (to JK), managed by UT-Battelle, LLC, for the US Department of Energy (DOE). This work acknowledges additional support from the Scientific User Facilities Division of the DOE Office of Basic Energy Sciences, for the EQ-SANS instrument at the ORNL Spallation Neutron Source. This facility is managed for the DOE by UT-Battelle, LLC, under contract No. DE-AC05-00OR2275.

References

Caillé, A. (1972). *C. R. Acad. Sci. Paris B*, **274**, 891–893.
 Escribá, P. V., González-Ros, J. M., Goñi, F. M., Kinnunen, P. K., Vigh, L., Sánchez-Magraner, L., Fernández, A. M., Busquets, X., Horváth, I. & Barceló-Coblijn, G. (2008). *J. Cell. Mol. Med.* **12**, 829–875.
 Frühwirth, T., Fritz, G., Freiburger, N. & Glatter, O. (2004). *J. Appl. Cryst.* **37**, 703–710.
 Goldberg, D. (1989). *Genetic Algorithms in Search, Optimization, and Machine Learning*. New York: Addison-Wesley Professional.

Greenwood, A. I., Tristram-Nagle, S. & Nagle, J. F. (2006). *Chem. Phys. Lipids*, **143**, 1–10.
 Hammersley, A. (1997). *FIT2D*. Internal Report ESRF97HA02T. European Synchrotron Radiation Facility, Grenoble, France.
 Heberle, F. A., Pan, J., Standaert, R. F., Drazba, P., Kučerka, N. & Katsaras, J. (2012). *Eur. Biophys. J.* **41**, 875–890.
 Hodzic, A., Rappolt, M., Amenitsch, H., Laggner, P. & Pabst, G. (2008). *Biophys. J.* **94**, 3935–3944.
 Huang, J. & Feigenson, G. W. (1999). *Biophys. J.* **76**, 2142–2157.
 Hung, W. C., Lee, M. T., Chen, F. Y. & Huang, H. W. (2007). *Biophys. J.* **92**, 3960–3967.
 Kaasgaard, T., Mouritsen, O. G. & Jørgensen, K. (2003). *Biochim. Biophys. Acta Biomembr.* **1615**, 77–83.
 Klauda, J. B., Kucerka, N., Brooks, B. R., Pastor, R. W. & Nagle, J. F. (2006). *Biophys. J.* **90**, 2796–2807.
 Kucerka, N., Liu, Y., Chu, N., Petrache, H. I., Tristram-Nagle, S. & Nagle, J. F. (2005). *Biophys. J.* **88**, 2626–2637.
 Kučerka, N., Nagle, J. F., Sachs, J. N., Feller, S. E., Pencer, J., Jackson, A. & Katsaras, J. (2008). *Biophys. J.* **95**, 2356–2367.
 Kučerka, N., Nieh, M.-P. & Katsaras, J. (2011). *Biochim. Biophys. Acta Biomembr.* **1808**, 2761–2771.
 Kučerka, N., Pencer, J., Nieh, M.-P. & Katsaras, J. (2007). *Eur. Phys. J. E Soft Matter*, **23**, 247–254.
 Kučerka, N., Perlmutter, J. D., Pan, J., Tristram-Nagle, S., Katsaras, J. & Sachs, J. N. (2008). *Biophys. J.* **95**, 2792–2805.
 Lee, A. G. (2004). *Biochim. Biophys. Acta Biomembr.* **1666**, 62–87.
 Liu, Y. & Nagle, J. F. (2004). *Phys. Rev. E*, **69**, 040901.
 Luzzati, V. & Husson, F. (1962). *J. Cell Biol.* **12**, 207–219.
 Mayer, L., Hope, M., Cullis, P. & Janoff, A. (1985). *Biochim. Biophys. Acta Biomembr.* **817**, 193–196.
 Mouritsen, O. G. (2005). *Life as a Matter of Fat: the Emerging Science of Lipidomics*. Berlin: Springer-Verlag.
 Nagle, J. F. & Tristram-Nagle, S. (2000). *Biochim. Biophys. Acta Biomembr.* **1469**, 159–195.
 Ohvo-Rekilä, H., Ramstedt, B., Leppimäki, P. & Slotte, J. P. (2002). *Prog. Lipid Res.* **41**, 66–97.
 Pabst, G., Katsaras, J., Raghunathan, V. A. & Rappolt, M. (2003). *Langmuir*, **19**, 1716–1722.
 Pabst, G., Koschuch, R., Pozo-Navas, B., Rappolt, M., Lohner, K. & Laggner, P. (2003). *J. Appl. Cryst.* **36**, 1378–1388.
 Pabst, G., Kucerka, N., Nieh, M. P., Rheinstädter, M. C. & Katsaras, J. (2010). *Chem. Phys. Lipids*, **163**, 460–479.
 Pabst, G., Rappolt, M., Amenitsch, H. & Laggner, P. (2000). *Phys. Rev. E*, **62**, 4000–4009.
 Pabst, G., Zwegtick, D., Prassl, R. & Lohner, K. (2012). *Eur. Biophys. J.* **41**, 915–929.
 Pan, J., Cheng, X., Heberle, F. A., Mostofian, B., Kučerka, N., Drazba, P. & Katsaras, J. (2012). *J. Phys. Chem. B*, **116**, 14829–14838.
 Pan, J., Heberle, F. A., Tristram-Nagle, S., Szymanski, M., Koepfinger, M., Katsaras, J. & Kučerka, N. (2012). *Biochim. Biophys. Acta Biomembr.* **1818**, 2135–2148.
 Pan, J., Mills, T. T., Tristram-Nagle, S. & Nagle, J. F. (2008). *Phys. Rev. Lett.* **100**, 198103.
 Pan, J., Tristram-Nagle, S. & Nagle, J. F. (2009). *Phys. Rev. E*, **80**, 021931.
 Press, W. H., Teukolsky, S. A., Vetterling, W. A. & Flannery, B. P. (2007). *Numerical Recipes: The Art of Scientific Computing*, 3rd ed. Cambridge University Press.
 Qian, S. & Heller, W. T. (2011). *J. Phys. Chem. B*, **115**, 9831–9837.
 Rajpaul, V. (2012). *arXiv:1202.1643[astro-ph.IM]*.
 Salditt, T. (2005). *J. Phys. Condens. Matter*, **17**, R287–R314.
 Tristram-Nagle, S., Liu, Y., Legleiter, J. & Nagle, J. F. (2002). *Biophys. J.* **83**, 3324–3335.
 Uhríková, D., Rybár, P., Hianik, T. & Balgavý, P. (2007). *Chem. Phys. Lipids*, **145**, 97–105.
 Zhang, R., Suter, R. M. & Nagle, J. F. (1994). *Phys. Rev. E*, **50**, 5047–5060.

Supplementary Material

Global SAXS data analysis for multilamellar vesicles: The evolution of the scattering density profile (SDP) model

Peter Heftberger, Benjamin Kollmitzer, Frederick A. Heberle, Jianjun Pan, Michael Rappolt, Heinz Amenitsch, Norbert Kučerka, John Katsaras, Georg Pabst

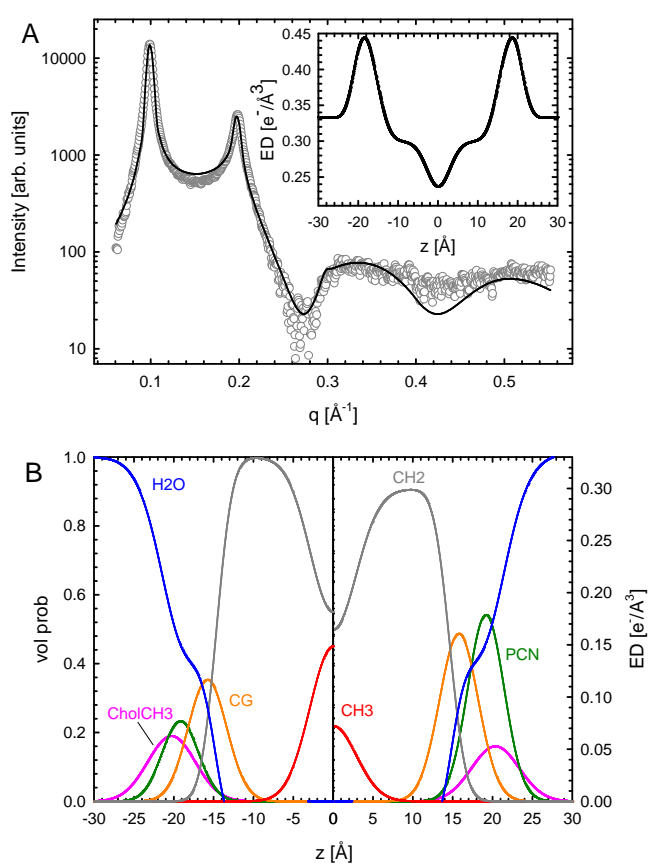


Figure S1: SDP-GAP analysis of DOPC MLVs at 30 °C. Panel A compares the best SDP-GAP fit (black line) to experimental data (grey circles). The insert represents the corresponding electron density profile. Panel B shows the volume probability distribution (left hand side) and the electron density distributions of the considered quasi-molecular fragments (right hand side).

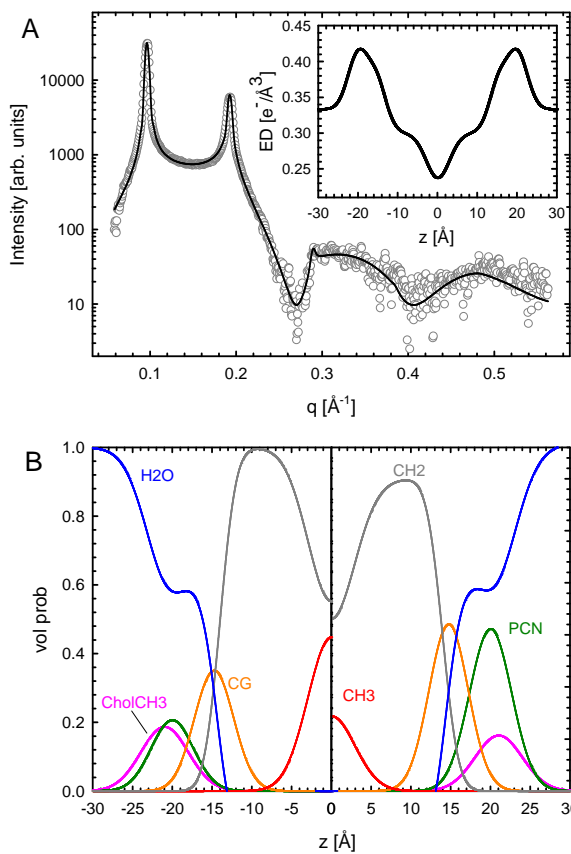


Figure S2: SDP-GAP analysis of DPPC MLVs at 50°C. Panel A compares the best SDP-GAP fit (black line) to experimental data (grey circles). The insert represents the corresponding electron density profiles. Panel B shows the volume probability distribution (left hand side) and the electron density distributions of the considered quasi-molecular fragments (right hand side).

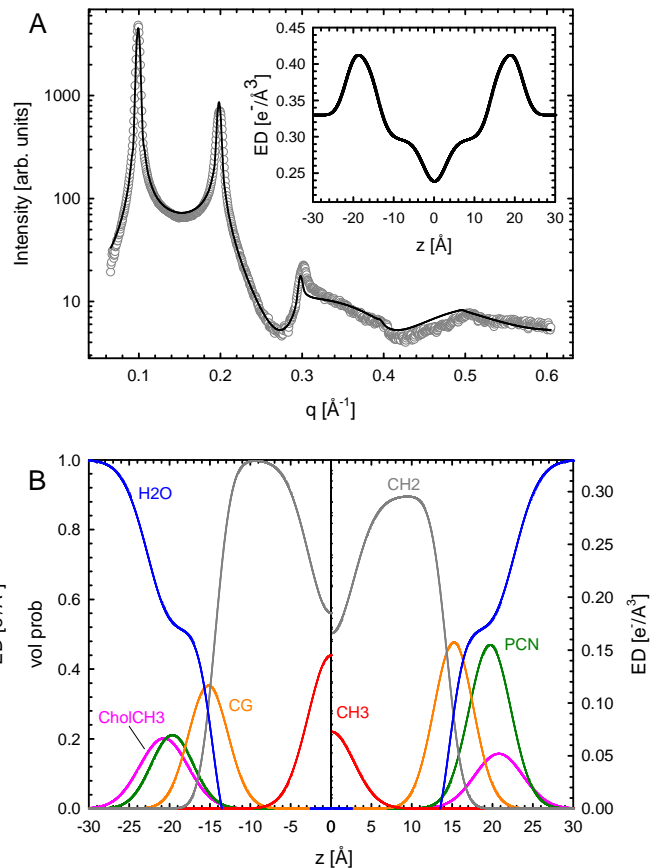


Figure S3: SDP-GAP analysis of POPC MLVs at 30°C. Panel A compares the best SDP-GAP fit (black line) to experimental data (grey circles). The insert represents the corresponding electron density profiles. Panel B shows the volume probability distribution (left hand side) and the electron density distributions of the considered quasi-molecular fragments (right hand side).

Table S1: Structural parameters of four different phospholipid bilayers analyzed by SDP-GAP. Parameter uncertainties are estimated to be $< 2\%$ as described in Materials and Methods.

Par	DPPC	POPC	SOPC	DOPC
Temp	50°C	30°C	30°C	30°C
V_L [\AA^3]	1229	1256	1309	1303
V_{HL} [\AA^3]	331	331	331	331
A [\AA^2]	63.1	65.4	66.3	67.6
d_B [\AA]	39	38.4	39.5	38.5
d_{HH} [\AA]	37.9	37.3	38.7	36.9
d_C [\AA]	13.9	14.0	14.6	14.2
$z_{CholCH3}^*$ [\AA]	21.2	20.7	21.2	20.3
$\sigma_{CholCH3}^\dagger$ [\AA]	2.98	2.98	2.98	2.98
z_{PCN}^* [\AA]	20.2	19.7	20.2	19.3
σ_{PCN}^\dagger [\AA]	2.7	2.6	2.5	2.5
z_{CG}^* [\AA]	14.7	15.0	15.6	15.2
σ_{CG}^\dagger [\AA]	2.4	2.4	2.5	2.5
σ_{HC}^\dagger [\AA]	2.4	2.4	2.4	2.4
σ_{CH3}^\dagger [\AA]	2.8	2.9	2.8	2.6
d [\AA]	65.19	63.31	65.71	63.46
d_W [\AA]	26.2	24.9	26.3	24.9
η	0.08	0.06	0.06	0.1
χ^2	0.65	1.23	0.87	1.31

* z_i representing the position of molecular fragments.

† σ_i representing the width of Gaussians of molecular fragments.

Table S2: Structural parameters of four different phospholipid bilayers containing 20 mol% cholesterol analyzed by SDP-GAP. Parameter uncertainties are estimated to be $< 2\%$ as described in Materials and Methods.

Par	DPPC	POPC	SOPC	DOPC
Temp	50°C	30°C	30°C	30°C
V_L [\AA^3]	1229	1256	1309	1303
V_{HL} [\AA^3]	331	331	331	331
A [\AA^2]	61.2	63.6	60.7	66.2
d_B [\AA]	40.1	39.5	40.5	39.4
d_{HH} [\AA]	42.3	40.3	42.1	40.9
d_C [\AA]	14.2	14.4	14.9	13.5
$z_{CholCH3}$ [\AA]	22.4	21.7	22.3	21.8
$\sigma_{CholCH3}$ [\AA]	2.98	2.98	2.98	2.98
z_{PCN} [\AA]	21.5	20.7	21.3	20.8
σ_{PCN} [\AA]	2.6	2.6	2.5	2.6
z_{CG} [\AA]	15.1	15.2	15.6	14.1
σ_{CG} [\AA]	2.6	2.6	2.6	2.6
σ_{HC} [\AA]	2.4	2.4	2.4	2.4
σ_{CH3} [\AA]	2.4	2.5	2.6	2.1
d [\AA]	67.48	65.78	67.95	67.46
d_W [\AA]	27.3	26.3	27.4	28.1
η	0.02	0.05	0.05	0.14
χ^2	1.9	0.75	0.99	1.59

Table S3: Structural parameters for POPC at 30°C using diverse combinations of SAXS and SANS data. Parameter uncertainties are estimated to be < 2% as described in Materials and Methods.

Par	n-ULV _u [*]	n-ULV _d [†]	n-MLV _u [‡]	n-MLV _d [§]	all data [¶]
A [Å]	65.0	63.1	63.6	63.1	63.6
d_B [Å]	38.6	39.8	39.5	39.8	39.5
d_{HH} [Å]	36.8	37.4	37.1	37.3	37.5
d_C [Å]	14.1	14.4	14.6	14.4	14.3
$z_{CholCH3}$ [Å]	20.4	20.9	20.5	20.7	20.9
$\sigma_{CholCH3}$ [Å]	2.98	2.98	2.98	2.98	2.98
z_{PCN} [Å]	19.4	19.9	19.5	19.7	19.9
σ_{PCN} [Å]	2.5	2.6	2.6	2.5	2.6
z_{CG} [Å]	15.0	15.4	15.3	15.4	15.3
σ_{CG} [Å]	2.4	2.4	2.4	2.4	2.4
σ_{HC} [Å]	2.4	2.4	2.4	2.4	2.4
σ_{CH3} [Å]	2.8	2.8	2.8	2.7	2.8

*SAXS (POPC-MLV) and SANS (POPC-ULV) data.

†SAXS (POPC-MLV) and SANS (POPC-d31-ULV) data.

‡SAXS (POPC-MLV) and SANS (POPC-MLV) data.

§SAXS (POPC-MLV) and SANS (POPC-d31-MLV) data.

¶SAXS (POPC-MLVs) and SANS (POPC-ULVs/MLVs, POPC-d31-ULVs/MLVs) data.

Article

In Situ Determination of Structure and Fluctuations of Coexisting Fluid Membrane Domains

Peter Heftberger,^{1,2} Benjamin Kollmitzer,^{1,2} Alexander A. Rieder,^{1,2} Heinz Amenitsch,³ and Georg Pabst^{1,2,*}¹Biophysics Division, Institute of Molecular Biosciences, University of Graz, NAWI Graz, Graz, Austria; ²BioTechMed-Graz, Graz, Austria; and ³Institute of Inorganic Chemistry, Graz University of Technology, Graz, Austria

ABSTRACT Biophysical understanding of membrane domains requires accurate knowledge of their structural details and elasticity. We report on a global small angle x-ray scattering data analysis technique for coexisting liquid-ordered (L_o) and liquid-disordered (L_d) domains in fully hydrated multilamellar vesicles. This enabled their detailed analysis for differences in membrane thickness, area per lipid, hydrocarbon chain length, and bending fluctuation as demonstrated for two ternary mixtures (DOPC/DSPC/CHOL and DOPC/DPPC/CHOL) at different cholesterol concentrations. L_o domains were found to be ~ 10 Å thicker, and laterally up to 20 Å²/lipid more condensed than L_d domains. Their bending fluctuations were also reduced by $\sim 65\%$. Increase of cholesterol concentration caused significant changes in structural properties of L_d , while its influence on L_o properties was marginal. We further observed that temperature-induced melting of L_o domains is associated with a diffusion of cholesterol to L_d domains and controlled by L_o/L_d thickness differences.

INTRODUCTION

Since the formulation of the raft model in 1997 by Simons and Ikonen (1) significant scientific efforts have been devoted to the characterization of physical properties of liquid-disordered L_d and liquid-ordered L_o domains (2–11). Membrane rafts are thought to be small (nanoscopic) and highly dynamic platforms enriched in sphingolipids and cholesterol, enabling diverse cellular functions, but have so far escaped any direct visualization in live cells (5,12). Hence, the existence of rafts remains a highly controversial issue. For example Frisz et al. (13,14), using secondary ion mass spectrometry on fibroblasts, observed sphingolipid domains, in which cholesterol was evenly distributed throughout the membrane, thus challenging the standard raft hypotheses.

In contrast to natural membranes, domains in lipid-only systems can grow up to several micrometers in size, enabling their detection (e.g., by optical microscopy (15)) and study with respect to the physics pertaining to their stability, size, or effect on protein sorting, to name but a few examples (8). One of the parameters involved in, e.g., protein sorting, is the difference in thickness between the L_o and L_d domains and the corresponding match to the protein's transmembrane region (see, e.g., Killian (16) and Pabst (17)).

To address these issues, diverse experimental and theoretical techniques have been employed to explore structural

and elastic properties of L_o/L_d phases (see, e.g., the literature (18–32)). Scattering experiments are of particular interest in this respect, because they allow for a label-free determination of membrane structure and dynamics (33). However, contrast between L_o and L_d domains is low. This can be addressed, for example, by contrast variation, using neutron scattering (34). In recent years, this technique has been used largely by Katsaras and coworkers, showing, e.g., the coupling of domain size and membrane thickness mismatch between L_o and L_d (35).

Alternatively, early x-ray experiments used Triton X-100 (Dow Chemical, Midland, MI) to separate detergent-resistant from detergent-soluble membranes, respectively (22). However, the application of detergents on membranes may adversely influence the mixing behavior of membrane lipids (36), limiting the applicability of this approach.

Another possibility, which is being explored in this work, makes use of the experimental finding that macroscopic domains are typically in registry in multilamellar systems (see, e.g., Chen et al. (28), Tayebi et al. (37), and Karmakar et al. (38)), meaning: L_o and L_d domains form lamellar lattices with distinct Bragg peaks. The challenges to be met here are 1) overlapping L_o/L_d Bragg reflections, in particular at low scattering angles; and 2) the small number of solid orders (only 2–3) displayed by L_d phases in fully hydrated multilamellar vesicles (MLVs), limiting the structural information content when only Bragg peak intensities are analyzed (39).

The latter issue is particularly well known for single-phase fluid bilayers, and has led to the development of a global SAXS data analysis technique that takes into account both Bragg peaks and diffuse scattering (39). Most recently,

Submitted October 16, 2014, and accepted for publication November 24, 2014.

*Correspondence: georg.pabst@uni-graz.at

This is an open access article under the CC BY license (<http://creativecommons.org/licenses/by/4.0/>).

Editor: Anne Kenworthy.

© 2015 The Authors

0006-3495/15/02/0854/9 \$2.00

<http://dx.doi.org/10.1016/j.bpj.2014.11.3488>



we have advanced the technique by incorporating the scattering density profile (SDP) model (40), enabling us to determine membrane structure and bending fluctuations from homogeneous MLVs at high resolution (41).

To access coexisting fluid domains in MLVs, the global SAXS data analysis needs to be further extended. This was achieved in this work by assuming a linear combination of scattering intensities originating from L_o and L_d phases. The method was applied to two ternary mixtures, with the high-melting lipids DPPC (dipalmitoylphosphatidylcholine) or DSPC (distearoylphosphatidylcholine), the low-melting lipid DOPC (dioleoylphosphatidylcholine), and CHOL (cholesterol). Summaries of the studied samples and applied nomenclature are given in Fig. 1 and Table S1 in the Supporting Material.

We observed distinct structural and elastic properties of L_o and L_d domains as a function of temperature and composition (lipid chain length and cholesterol concentration).

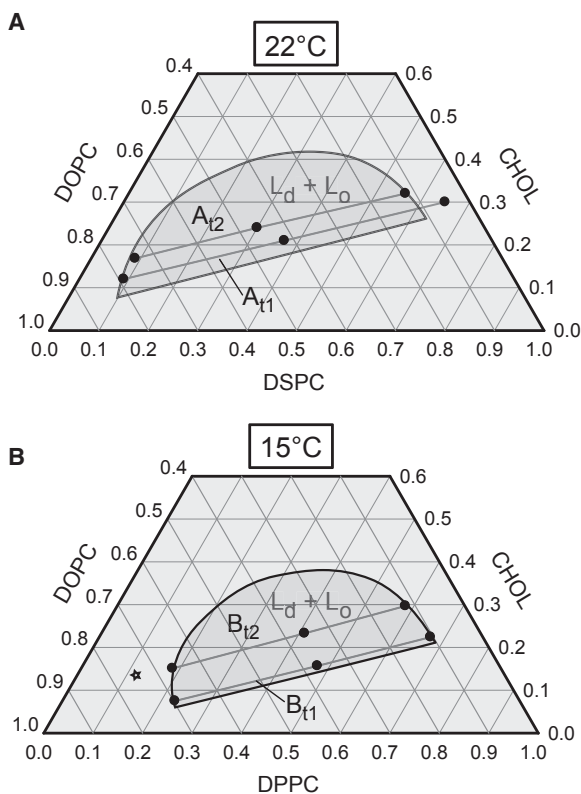


FIGURE 1 Overview of samples studied in this work. (Solid circles) Their location is shown in previously reported compositional phase diagrams of (A) DOPC/DSPC/CHOL (50) and (B) DOPC/DPPC/CHOL (49). In fluid-fluid phase coexistence regions (dark-shaded areas), demixing into L_o and L_d domains occurs along tielines. Two tielines for each system (A_{t1} , A_{t2} and B_{t1} , B_{t2}) with three different compositions at the L_d , L_o endpoints and the tieline center were studied (see Table S1 for detailed lipid composition). Note that tieline endpoints for L_o on A_{t1} and L_d on B_{t2} (star) are outside previously reported phase boundaries. This is either due to updates in phase boundaries for isolated tielines (A_{t1} (35)) or experiments performed in this study (B_{t2} , see Results).

Most interestingly, we found that increased cholesterol concentrations reduce the thickness difference between L_d and L_o domains, which leads to a decrease of line tension and in turn promotes the temperature induced melting of L_o domains.

MATERIALS AND METHODS

Sample preparation

DPPC, DSPC, and DOPC were purchased from Avanti Polar Lipids (Alabaster, AL), and cholesterol was obtained from Sigma-Aldrich (Vienna, Austria). All lipids were used without further purification, with all chemicals being of professional analysis quality. Lipid stock solutions were prepared by dissolving weighted amounts of dry lipid in chloroform/methanol (2:1, v/v) and then mixed at appropriate ratios (see Table S1 for all samples and their corresponding compositions). Subsequently, lipid solutions were dried under a stream of nitrogen and then placed under vacuum for ~12 h, forming a thin lipid film on the bottom of glass vials. Dry films were hydrated using 18 MΩ/cm water and incubated for 6 h above the main transition temperature of the high-melting lipid (DPPC or DSPC), repetitively cycling vortex-mixing and freeze-thaw procedures using liquid N_2 . The final lipid concentration for each sample was 50 mg/mL. All samples were prepared at least twice (with a time delay of several weeks) starting from pure lipid powders to check for reproducibility. Lattice constants (d -values) varied by $< \pm 0.5\%$. Furthermore, thin layer chromatography on randomly selected samples revealed no decomposition of the samples into lyso lipids or free fatty acids.

Small angle x-ray scattering

X-ray scattering data were acquired at the Austrian SAXS beamline Elettra Trieste, Trieste, Italy, using 8 keV photons. Diffraction profiles were detected utilizing a Mar300-image-plate detector (MarResearch, Norderstedt, Germany) and calibrated using silver behenate. Lipid dispersions were taken up in 1-mm-thick quartz capillaries and inserted into a multiposition sample holder. All samples were equilibrated for a minimum of 10 min before measurement using a circulating water bath. The exposure time was set to 30 s. Scattering patterns were integrated using the program FIT2D (42). Background scattering originating from capillaries, water, and air was subtracted (43), and data sets were normalized using the transmitted intensity, which was measured by a photodiode placed in the beam stop.

Analysis of coexisting domains

To analyze the scattering profile of MLVs exhibiting L_o/L_d phase coexistence, we adopted the full- q -range model by Hefterberger et al. (41) for homogeneous bilayers. For the latter systems, the scattered intensity is given by

$$I(q) = \frac{1}{q^2} [|F(q)|^2 S(q) (1 - N_{\text{diff}}) + |F(q)|^2 N_{\text{diff}}], \quad (1)$$

where $q = 4\pi \sin\theta/\lambda$ is the scattering vector, λ is the wavelength, 2θ is the scattering angle relative to the incident beam, and N_{diff} is the diffuse scattering originating from positionally uncorrelated bilayers. The structure factor $S(q)$ is given by the Caillé theory (39,44–46), yielding access to bending fluctuations via the Caillé parameter

$$\eta \propto \frac{T}{\sqrt{K_c B}},$$

with K_C as the bilayer bending rigidity and B as the bulk modulus of interactions (39). The form factor $F(q)$ is the Fourier transform of the electron density profile of a bilayer, described in terms of the SDP model (40).

Neglecting putative cross-correlations between L_o and L_d domains, the scattered intensity of coexisting fluid domains can be modeled by a linear combination of the individual L_o/L_d intensities,

$$I(q) = \frac{1}{q^2} [(1 - N_{\text{diff}})I_{\text{corr}}(q) + N_{\text{diff}}I_{\text{uncorr}}(q)], \quad (2)$$

where

$$I_{\text{corr}}(q) = |F_{L_d}(q)|^2 S_{L_d}(q) c_{L_d} + |F_{L_o}(q)|^2 S_{L_o}(q) (1 - c_{L_d})$$

and

$$I_{\text{uncorr}}(q) = |F_{L_d}(q)|^2 c_{L_d} + |F_{L_o}(q)|^2 (1 - c_{L_d})$$

are the scattering intensities originating from positionally correlated and uncorrelated bilayers, respectively. The subscripts L_o and L_d denote the individual contributions of the domains to $S(q)$ and $F(q)$, and c_{L_d} refers to the L_d phase fraction in the sample. Analysis of the scattered intensity of coexisting phases in terms of this model yields bilayer structural parameters and bending fluctuations simultaneously for L_o and L_d . A strict requirement for its application is that domains are in registry in the direction normal to the bilayer plane, meaning: two distinct lamellar lattices need to be observed. This is typically the case for macroscopic domains, observed for example when diunsaturated lipids such as DOPC are used as low-melting membrane component in ternary raftlike mixtures (28,37,38).

The SDP model, used to describe the form factors, parses the bilayer lipids into quasi-molecular fragments and calculates their volume probability distributions. The model was originally designed for determining single lipid component bilayers (40,47). Pan et al. (48) extended the SDP analysis to binary lipid mixtures containing cholesterol. To this end the contribution of cholesterol was merged with that of methylene (CH_2) groups, which was recently also applied successfully to homogenous MLVs (41). Because our studied L_o and L_d domains contain different amounts of three lipids, effective lipid molecules were constructed for the SDP description, by first merging the contributions from the unsaturated and saturated lipids and then adding cholesterol to the CH_2 regime as described above. Saturated and unsaturated lipids differ with respect to the number of CH_2 and methine (CH) groups. Due to the absence of scattering contrast between CH and CH_2 for x-rays, these groups can be merged (40,41). Our final parsing approach consisted of five groups for each phase, composed of the following: 1) CholCH_3 (Choline methyl), 2) PCN (Phosphate + $\text{CH}_2\text{CH}_2\text{N}$), 3) CG (Carbonyl + glycerol) groups, 4) CH_2 , and 5) CH_3 methyl groups at the bilayer center.

This approach is further justified by its compatibility to previously reported molecular dynamics (MD) data (31), as demonstrated in Fig. 2. For details of the functional forms used to describe the individual groups, we refer to the literature (40,41,48). As detailed previously (41), a genetic algorithm was applied for fitting the global model to experimental data.

Membrane structural parameters such as hydrocarbon chain length d_C , Luzzati thickness d_B , water layer thickness d_W , and the area per lipid $A = 2V_L/d_B$ were defined and calculated from the SDP profiles as described in Heftberger et al. (41). V_L is the total lipid volume, which is assumed to be given by the molecular-weighted average

$$V_L(T) = \sum_i x_i(T) V_i(T), \quad (3)$$

where x_i values are the lipid molar ratios in L_d and L_o taken from Uppamoochikkal et al. (49) and Heberle et al. (50), V_i values are the corresponding molecular lipid volumes, and T is the temperature. Temperature-dependent V_i values were calculated according to the method of Koenig and Gawrisch (51), and the volume of cholesterol within lipid bilayers was taken to be

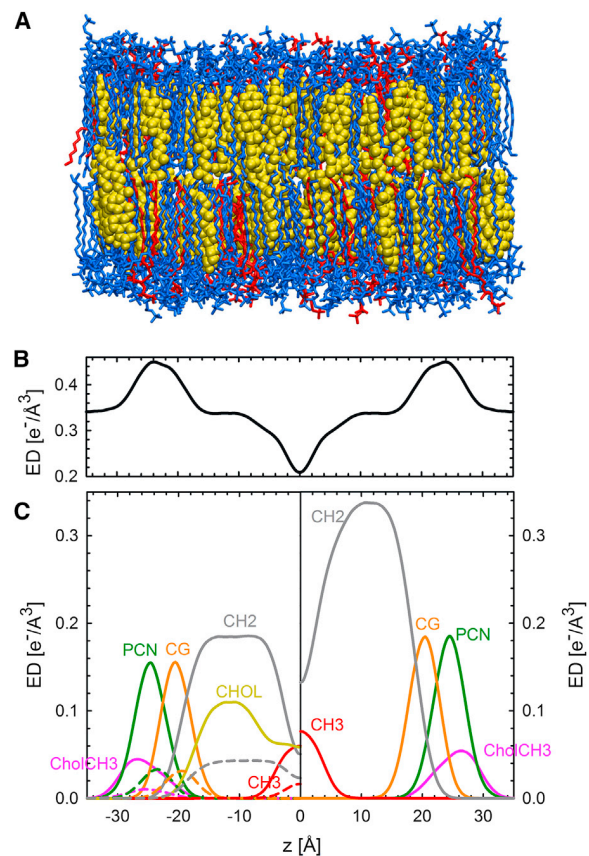


FIGURE 2 Parsing scheme of ternary lipid mixtures based on MD simulations of an L_o phase of DOPC/DPPC/CHOL (31). (A) Snapshot of the equilibrated system. DPPC lipids, blue; DOPC, red; cholesterol, yellow. (B) Calculated electron density profile. (C) Electron densities of molecular groups, calculated using SIMTOEXP (70). (Left) Individual contributions of DPPC (solid lines) and DOPC (dashed lines) for the CholCH_3 , PCN, CG, CH_2 , and CH_3 groups. (Yellow line) Contribution of cholesterol. (Right) Condensed parsing scheme after merging individual contributions as detailed in the main text. To see this figure in color, go online.

630 \AA^3 (52). Calculated tieline endpoint V_L were in good agreement ($<2\%$) with experimental values determined by dilatometry (Supporting Material). Note that dilatometry yields a globally averaged value for the lipid volume and is thus not able to discern between L_o and L_d in the phase coexistence regime. Thus experimental V_L can be obtained for tieline endpoints, only. The temperature dependence of x_i was estimated by the lever rule using the experimentally determined L_d and L_o fractions (c_{L_d} and $1 - c_{L_d}$), assuming 1) that the inclination of the tieline remains constant, and 2) that the tieline length changes according to the L_o fraction with temperature (Supporting Material).

RESULTS AND DISCUSSION

Establishing the global analysis for two phases

Our strategy to validate this analysis was as follows. 1) We evaluated tieline endpoint SAXS data. At endpoints, either L_o or L_d should exist as a single phase, thus allowing application of our previous analysis for homogeneous MLVs (41). 2) The phase coexistence model was applied to a

composition close to the tieline midpoint and the achieved results were compared to endpoint data.

Phase boundaries, in particular, are subject to considerable uncertainties (8,49,53–55), whereas recent tieline orientation data are considered to be more reliable. In this study, we applied previously published compositional phase diagrams from Heberle et al. (50) and Uppamoochikkal et al. (49). Note that Uppamoochikkal et al. (49) used the phase diagram reported by Veatch et al. (54), and constructed tielines using x-ray scattering on oriented lipid films.

Our measurement strategy allowed for an independent check of these data, as follows: 1) Bragg peaks of all samples measured per tieline are required to overlap, if tieline orientation is correct (49); and 2) only a single lamellar lattice should be observed at the phase boundaries.

For all samples, including replicas, L_o/L_d peak positions for tieline midpoints and endpoints matched, reassuring not only tieline orientation data, but also our sample preparation. The L_d endpoints of DOPC/DPPC/CHOL contained significant residual scattering from an L_o phase, revealing errors in the reported phase boundary. However, because L_o peaks overlapped with those of the L_o endpoint, we were able to subtract the L_o contribution (Fig. S1 in the Supporting Material). In independent experiments, using a laboratory x-ray camera, we determined for B_{12} a new L_d endpoint by measuring several samples along the tieline until the L_o contributions vanished. The new endpoint composition is 0.748/0.124/0.128 (Fig. 1); corresponding SAXS data are shown in Fig. S2.

Fig. 3 details the results and analysis of the A_{11} tieline. The L_d endpoint in this study showed some residual L_o contribution. However, it was small enough to be neglected. Global fits to tieline endpoints and midpoints show that our model is able to capture both the single-phase and two-phase coexistence, respectively. Insets to Fig. 3 show the volume probability distributions of individual quasi-molecular groups (see previous section) for L_o , L_d endpoints and the resulting electron density (ED) profiles for the coexisting case. The absolute ED in the hydrocarbon chain region of the L_o phase is significantly higher than in L_d . This can be explained by the higher amount of cholesterol in the L_o phase, with substantial ED contributions from the sterol ring.

All structural parameters for coexisting domains agreed remarkably to tieline endpoints (Tables 1 and S2), thereby validating our analysis. For example, the membrane thickness d_B for L_d and L_o endpoints is 37.5 and 49.7 Å, respectively. This compares well to $d_B = 38.1$ and 48.6 Å for L_d and L_o in the coexistence regime, meaning: differences are within <1 Å. Note that height differences Δd_B between L_d and L_o domains are in the same range as those reported between detergent-resistant and detergent-soluble membranes (22).

The two-phase analysis was further tested by checking whether a decrease of the hydrocarbon chain length of the

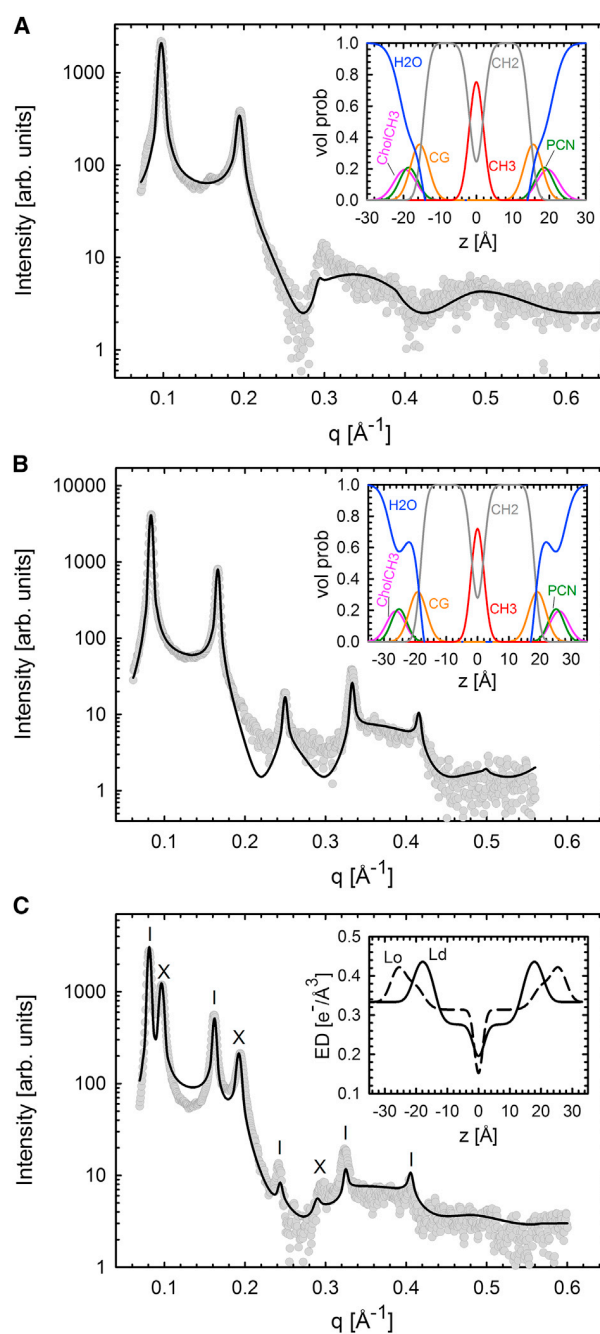


FIGURE 3 Validation of the global analysis for two coexisting phases for the A_{11} tieline ($T = 22^\circ\text{C}$). (A and B) Fits to L_d and L_o endpoint data, respectively. (Insets, both panels) Derived volume probability distributions. (C) Best fit to SAXS data at the A_{11} tieline midpoint. Bragg reflections of L_o (dashes) and L_d (crosses) domains. (Inset) ED profiles for L_o and L_d phases. To see this figure in color, go online.

mixture's high-melting lipid leads to reasonable changes in domain structure. Exchanging DSPC with DPPC affected mainly the structure of the L_o phase. Picking for example the $t1$ tielines, d_B decreased by 2.6 Å, whereas only a minor decrease of 0.6 Å was found for L_d . Similar changes were found for other tielines, including d_c -values (Table 1).

TABLE 1 Structural results and bending fluctuations for coexisting L_d/L_o domains

Term	d_B	A	d_W	d_C	η
$A_{t1}(L_d)$	38.5	63.1	26.6	14.5	0.091
$A_{t1}(L_o)$	49.8	43.2	27.6	18.8	0.030
$A_{t2}(L_d)$	39.2	60.3	26.5	14.9	0.092
$A_{t2}(L_o)$	49.2	43.1	26.8	18.5	0.029
$B_{t1}(L_d)$	37.9	64.9	26.0	14.2	0.074
$B_{t1}(L_o)$	47.2	44.4	25.1	17.7	0.021
$B_{t2}(L_d)$	38.9	61.2	25.8	14.7	0.068
$B_{t2}(L_o)$	46.4	43.5	23.3	17.3	0.024

Parameter uncertainties are $<2\%$.

Our findings are in excellent agreement with tieline orientation (Fig. 1); because the high-melting lipid is located in L_o domains, we observe a thinning by exchanging DSPC to DPPC, which contains two CH_2 groups less per acyl chain. Kučerka et al. (47) reported a similar thickness difference for pure DSPC and DPPC bilayers. L_d phases contain mainly DOPC and are consequently barely effected by the lipid exchange. Further structural parameters for L_d (Table 1) are close to that of pure DOPC (40).

Finally, we compare areas per lipid, A , which differ significantly between L_d and L_o phases (Table 1). The L_d domains exhibited A values between 60 and 65 \AA^2 , which is in the range of values reported for fluid single lipid bilayers (40,47). Areas are $\sim 20 \text{ \AA}^2$ smaller for L_o domains. The main reason for this difference is the condensing effect of cholesterol, which was previously reported for several binary phosphatidylcholine/cholesterol mixtures (48,56–58) and is now also observed for coexisting L_o/L_d domains. Another manifestation of this ordering effect is the decrease of the bending fluctuation parameter from $\eta \sim 0.08$ (L_d) to ~ 0.03 (L_o).

Thus, concluding this section: our global SAXS data analysis yields, within typical uncertainties of the SDP model, robust high-resolution results for structure and fluctuations of coexisting L_o/L_d domains. This allows us to obtain reliable insights on changes of these parameters, e.g., as a function of composition or temperature. Results of such experiments are presented in the following sections.

Effect of cholesterol on domains

To study the influence of raising cholesterol concentration, we compare the $t1$ and $t2$ tieline midpoints for both ternary mixtures. Scattering profiles and fits are plotted in Fig. 3 (Figs. S3, S4, and S5), while results for structural and elastic parameters are presented in Table 1. For both systems studied, d increased by $\sim 0.75 \text{ \AA}$ for L_d domains, but decreased by $\sim 2 \text{ \AA}$ for L_o upon increasing cholesterol content. Our analysis revealed that the increase of d for L_d is mainly due to a thickening of its bilayer, whereas only approximately one-third of the decrease of d for L_o can be attributed to d_B . A decrease of d_B for L_o upon increasing

cholesterol concentration may seem counterintuitive, but the marginal additional ordering effect due to more cholesterol is overcompensated by a reduction of the high-melting lipid concentration. Most of the change in d for L_o is due to a decrease of the interstitial water layer ($1\text{--}2 \text{ \AA}$), which may originate either from an increase in net attractive forces, or a decrease in net repulsive forces between L_o domains. This effect cannot be attributed to an increased bending rigidity due to the higher cholesterol content (59), because the fluctuations did not decrease (Table 1). Instead, a decrease of hydration or an increase of van der Waals forces might be the reason.

The area per lipid was found to be smaller for L_d domains of the $t2$ tielines (Table 1), which can be attributed to the well-known condensing effect of cholesterol (58). For L_o domains, changes for A were found to be insignificant (within experimental uncertainty). However, it is interesting to note that the variation of A for L_o even across DOPC/DPPC/CHOL and DOPC/DSPC/CHOL is within $< \pm 2\%$. This indicates that the average value $A \sim 43.6 \text{ \AA}^2$ could be the tightest possible packing of lipids in the L_o phase. More structural data on L_o would certainly be needed to validate this notion.

Temperature dependence of L_o/L_d domains

Starting from the reported compositional phase diagrams (Fig. 1), we increased temperature in steps of 5°C until we reached a homogeneous phase. The transition is observed as a merging of the L_o and L_d lattices into a single L_d phase lattice (Fig. 4). For DOPC/DSPC/CHOL, the transition at T_C occurred between 45 and 50°C , and for DOPC/DPPC/CHOL, between 30 and 35°C . Note that our temperature resolution does not allow us to determine T_C with high accuracy. Fig. 5 A compares the results for d_B of A_{t1} and B_{t1} . The L_o phase of B_{t1} was found to be 3 \AA thinner than that of A_{t1} . Because changes with temperature are similar for both $t1$ and $t2$ tielines (Figs. 5 and S6), we can therefore limit the discussion to the $t1$ tielines. In the temperature range of $22\text{--}45^\circ\text{C}$ d_B of L_d domains increased monotonously by $\sim 1\text{--}1.5 \text{ \AA}$, whereas d_B for L_o decreased at the same time by 2 \AA . Close to T_C , these changes are significantly accelerated. Above the transition temperature, d_B is similar to that of the L_d phase just below T_C . Interestingly, d_B is approximately equal for DSPC- and DPPC-containing samples above T_C , including the $t2$ tielines (Fig. S6) despite the difference in hydrocarbon chain length.

The thickness of single-phase fluid lipid bilayers typically decreases with increasing temperature (47,60,61). Thus, the thickening of the L_d domains upon approaching T_C from below is surprising. Davis and Schmidt (23) recently suggested, based on NMR data, that the cholesterol fraction in L_o decreases with temperature. Consequently, L_d would get enriched in cholesterol. Because of the associated condensation effect of cholesterol, one would then expect

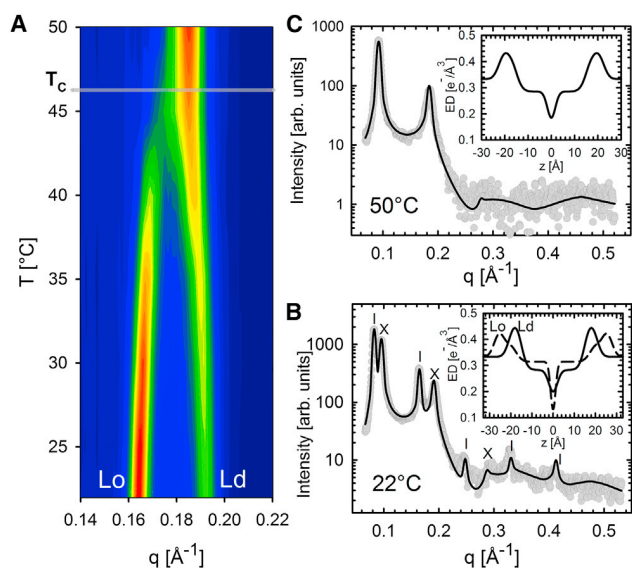


FIGURE 4 Temperature behavior of DOPC/DSPC/CHOL (tieline t_2) as revealed by SAXS. (A) Contour plot of the second-order Bragg reflections indicated as L_o and L_d . Note that the smooth appearance of data is due to an interpolation procedure between the individual frames. The critical temperature T_C is between 45 and 50°C. At $>T_C$, only a single lamellar lattice is observed. (B) Measured scattering at 22°C with the indicated Bragg reflections for L_o (dashes) and L_d (crosses) domains. (C) The same, for 50°C. (Solid lines) Best fits. (Insets, both panels) Resulting ED profiles for L_o and L_d phases. To see this figure in color, go online.

an increase of the L_d domain thickness. Our results consequently corroborate this scenario.

The area per lipid is inversely proportional to d_B . Hence the temperature changes of A are similar to d_B , but just with inverted trends, i.e., A decreases for L_d and increases for L_o , as observed in Fig. 5 B. We further note that areas above T_C are alike for all systems and tielines studied, which appears reasonable in view of the similar A -values reported for single-component DPPC and DSPC membranes (47). Changes of the water layers in turn appear to be decoupled from the trends of d_B and A . We found a general increase of d_W for L_d domains and a decrease for L_o domains (Fig. 5 C) below T_C , with changes close to T_C being more pronounced for the L_o phase. These findings are not straightforward to explain, in particular because the Caillé parameter did not show a strong increase of bending fluctuations for L_d , or decrease for L_o , respectively. Instead, an overall decrease in η was found for L_d (Fig. 6) and an increase in the vicinity of T_C for L_o . These two trends can be explained by the temperature-driven diffusion of cholesterol to L_d , as discussed above. Specific changes in d_W in turn appear to be caused by other influences on intermembrane interactions. Additional experiments, such as a combination of SAXS with osmotic stress (62), are needed to address this issue properly.

Melting of L_o domains can be further assessed by c_{Ld} , corresponding to the L_d phase fraction (Eq. 2). All studied systems show a steady increase of c_{Ld} as T_C is approached from

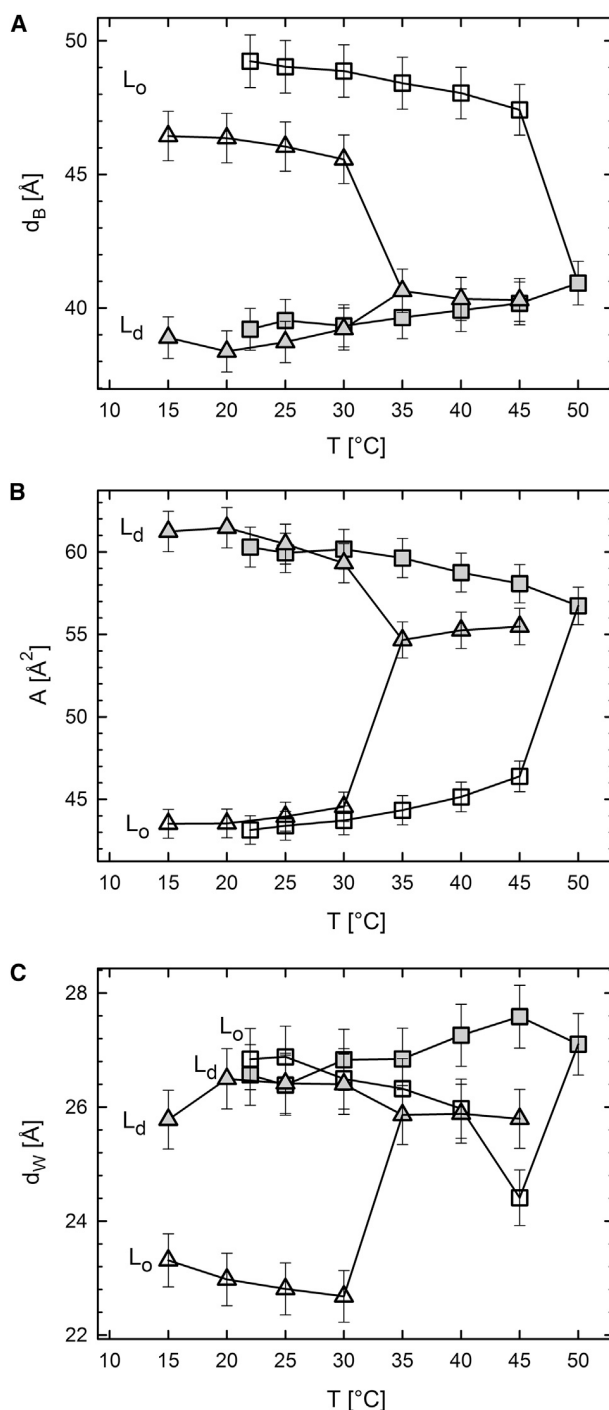


FIGURE 5 Temperature dependence of structural parameters of DOPC/DSPC/CHOL (squares) and DOPC/DPPC/CHOL (triangles), starting from the t_1 tieline midpoints (Fig. 1). (A) Bilayer thickness, (B) area per lipid, and (C) water layer thickness, for L_d (solid symbols) and L_o (open symbols) domains as a function of temperature.

below, while the t_2 composition of DOPC/DSPC/CHOL exhibited the largest overall L_d fraction (Fig. 7). The increase of c_{Ld} also signifies that the L_d tieline endpoints approach the chosen midpoints more rapidly than the L_o endpoints.

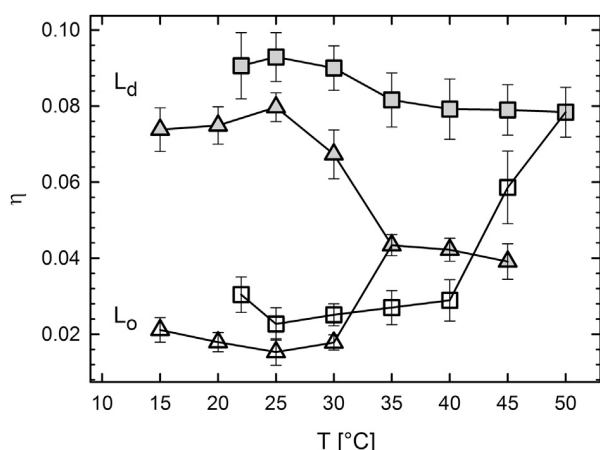


FIGURE 6 Temperature dependence of bending fluctuations of coexisting DOPC/DSPC/CHOL (squares) and DOPC/DPPC/CHOL (triangles) domains, for $t1$ tieline compositions (Fig. 1 and Table S1). (Shaded symbols) Results for L_d domain; (open symbols) results for L_o domain.

Hence, the L_o/L_d coexistence regime reduces asymmetrically with temperature, i.e., closes-in faster on the L_d boundary than on the L_o boundary, in agreement with Buboltz et al. (63) (and see the Supporting Material).

Finally, it is interesting to compare the relative increase of the L_d fraction in the studied temperature range. For DOPC/DSPC/CHOL, c_{L_d} increased with temperature by 16% for the $t1$ and 25% for the $t2$ tieline, respectively. Differences are smaller for DOPC/DPPC/CHOL, with $\Delta c_{L_d} = 9\%$ for $t1$ and 16% for $t2$, but here changes are more pronounced at higher cholesterol content. Hence, increasing cholesterol concentration appears to promote melting of L_o . This can be understood by reviewing the height differences between L_d and L_o domains (Table 1). For DSPC-containing mixtures, $\Delta d_B = 11.3 \text{ \AA}$ for the $t1$ tieline and $\Delta d_B = 10 \text{ \AA}$ or $t2$, whereas $\Delta d_B = 9.7 \text{ \AA}$ and $\Delta d_B = 7.5 \text{ \AA}$ for the $t1$ and $t2$ tielines in DOPC/DPPC/CHOL. Thus, Δd_B decreases with cholesterol concentration for both systems. The height differences are

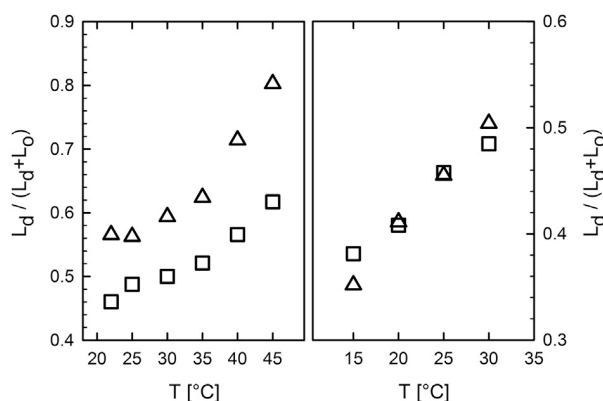


FIGURE 7 Variation of L_d phase fraction with temperature. (Left) Results for DOPC/DSPC/CHOL. (Right) Results for DOPC/DPPC/CHOL. (Squares) Results for $t1$ tielines; (triangles) results for $t2$ tielines.

related to the line tension γ between L_d and L_o domains. In particular, Akimov et al. (30) showed that $\gamma \propto \Delta d_B^2$. Consequently, the cholesterol-induced decrease of Δd_B leads to a lowering of γ , facilitating the melting of L_o domains.

CONCLUSIONS

We introduced a global SAXS data analysis technique, which yields structural and elastic properties of coexisting L_o/L_d domains in multilamellar vesicles. The model captures 1) high structural resolution by incorporating the SDP model (40) and 2) bending fluctuations through a Bragg peak line-shape analysis in terms of the Caillé theory structure factor (39). The method has been verified on DOPC/DSPC/CHOL and DOPC/DPPC/CHOL mixtures by comparing tieline endpoint with midpoint data of corresponding phase coexistence samples, and by essaying whether it captures the effects of chain length increase for L_o domains, such as thickness increase or a decrease of lipid area.

We further characterized two tielines for each ternary mixture to study effects of increased cholesterol concentration. Interestingly, additional cholesterol affected mostly structural properties of the L_d phase (increase of d_B and d_C , decrease of A , and decrease of η), whereas L_o appeared to be already saturated. A further effect of higher cholesterol concentration was a decrease of the thickness difference between L_o and L_d domains, leading to a lowering of line tension and consequently to a destabilization of L_o domains that is somehow analogous to the well-known order/disorder effect of cholesterol in binary lipid mixtures (64). The temperature behavior revealed structural and elastic changes during melting of L_o domains, which suggest that cholesterol diffuses into L_d domains even below T_C .

Because of its ability to analyze phase coexistence data without using labels, our technique should be able contribute to resolving several open questions in the field. One of the many controversial issues of raftlike lipid mixtures, for example, is their critical behavior across the transition into a homogeneous phase. According to theory, any defined order parameter should vary $\propto (T_C - T)^\beta$, where the critical exponent β is either 0.125 or 0.325, depending on whether the system follows the two- or three-dimensional Ising model, respectively (23,65–68). Fluorescence microscopy experiments on compositional fluctuations in the vicinity of T_C revealed a two-dimensional Ising model-like behavior (65–67). In contrast, atomic force measurements on the height-difference of L_o/L_d (68) and first momenta of NMR spectra (23) reported critical exponents favoring the three-dimensional Ising model. We analyzed the height difference between L_o and L_d phases across T_C to determine a critical exponent (Fig. S8). Our results favor the two-dimensional Ising model, but the apparently coarse temperature steps preclude us from any firm statement.

Future studies will be designed to exactly address this issue. Another interesting application for our technique will be to predict protein activity and partitioning in domains (17), which can be achieved by adding information on spontaneous curvatures (69) and bending elasticities (31,33) of L_o and L_d domains. This work is underway in our laboratory.

SUPPORTING MATERIAL

Supporting Materials and Methods, nine figures, and two tables are available at [http://www.biophysj.org/biophysj/supplemental/S0006-3495\(14\)04817-6](http://www.biophysj.org/biophysj/supplemental/S0006-3495(14)04817-6).

ACKNOWLEDGMENTS

We are grateful to George Khelashvili and Milka Doktorova for sharing MD simulation data on L_o phases and for providing us with the MD simulation snapshot. We further thank Frederick A. Heberle, Jianjun Pan, and John Katsaras for valuable discussions.

This work was supported by the Austrian Science Fund FWF, Project No. P24459-B20 (to G.P.).

REFERENCES

1. Simons, K., and E. Ikonen. 1997. Functional rafts in cell membranes. *Nature*. 387:569–572.
2. Simons, K., and D. Toomre. 2000. Lipid rafts and signal transduction. *Nat. Rev. Mol. Cell Biol.* 1:31–39.
3. Edidin, M. 2003. The state of lipid rafts: from model membranes to cells. *Annu. Rev. Biophys. Biomol. Struct.* 32:257–283.
4. McMullen, T. P. W., R. N. A. H. Lewis, and R. N. McElhaney. 2004. Cholesterol-phospholipid interactions, the liquid-ordered phase, and lipid rafts in model and biological membranes. *Curr. Opin. Colloid Interface Sci.* 8:459–468.
5. London, E. 2005. How principles of domain formation in model membranes may explain ambiguities concerning lipid raft formation in cells. *Biochim. Biophys. Acta.* 1746:203–220.
6. Brown, D. A., and E. London. 2000. Structure and function of sphingolipid- and cholesterol-rich membrane rafts. *J. Biol. Chem.* 275:17221–17224.
7. Brown, D. A., and E. London. 1998. Structure and origin of ordered lipid domains in biological membranes. *J. Membr. Biol.* 164:103–114.
8. Goñi, F. M., A. Alonso, ..., J. L. Thewalt. 2008. Phase diagrams of lipid mixtures relevant to the study of membrane rafts. *Biochim. Biophys. Acta.* 1781:665–684.
9. Marsh, D. 2010. Liquid-ordered phases induced by cholesterol: a compendium of binary phase diagrams. *Biochim. Biophys. Acta.* 1798:688–699.
10. Marsh, D. 2009. Cholesterol-induced fluid membrane domains: a compendium of lipid-raft ternary phase diagrams. *Biochim. Biophys. Acta.* 1788:2114–2123.
11. Heberle, F. A. 2014. Liposome-based models for membrane rafts: methodology and applications. In *Liposomes, Lipid Bilayers and Model Membranes: From Basic Research to Application*. CRC Press, Boca Raton, FL.
12. van Meer, G., D. R. Voelker, and G. W. Feigenson. 2008. Membrane lipids: where they are and how they behave. *Nat. Rev. Mol. Cell Biol.* 9:112–124.
13. Frisz, J. F., H. A. Klitzing, ..., M. L. Kraft. 2013. Sphingolipid domains in the plasma membranes of fibroblasts are not enriched with cholesterol. *J. Biol. Chem.* 288:16855–16861.
14. Frisz, J. F., K. Lou, ..., M. L. Kraft. 2013. Direct chemical evidence for sphingolipid domains in the plasma membranes of fibroblasts. *Proc. Natl. Acad. Sci. USA.* 110:E613–E622.
15. Veatch, S. L., and S. L. Keller. 2005. Seeing spots: complex phase behavior in simple membranes. *Biochim. Biophys. Acta.* 1746:172–185.
16. Killian, J. A. 1998. Hydrophobic mismatch between proteins and lipids in membranes. *Biochim. Biophys. Acta.* 1376:401–415.
17. Pabst, G. 2013. Coupling of membrane elasticity and structure to protein function. In *Advances in Planar Lipid Bilayers and Liposomes, Vol. 18*. A. Iglic, and C. Kulkarni, editors. Academic Press, London, United Kingdom, p. 282.
18. Binder, W. H., V. Barragan, and F. M. Menger. 2003. Domains and rafts in lipid membranes. *Angew. Chem. Int. Ed. Engl.* 42:5802–5827.
19. Veatch, S. L., and S. L. Keller. 2002. Organization in lipid membranes containing cholesterol. *Phys. Rev. Lett.* 89:268101.
20. Pitcher, 3rd, W. H., S. L. Keller, and W. H. Huestis. 2002. Interaction of nominally soluble proteins with phospholipid monolayers at the air-water interface. *Biochim. Biophys. Acta.* 1564:107–113.
21. McIntosh, T. J., A. Vidal, and S. A. Simon. 2003. Sorting of lipids and transmembrane peptides between detergent-soluble bilayers and detergent-resistant rafts. *Biophys. J.* 85:1656–1666.
22. Gandhavadi, M., D. Allende, ..., T. J. McIntosh. 2002. Structure, composition, and peptide binding properties of detergent soluble bilayers and detergent resistant rafts. *Biophys. J.* 82:1469–1482.
23. Davis, J. H., and M. L. Schmidt. 2014. Critical behavior in DOPC/DPPC/cholesterol mixtures: static ^2H NMR line shapes near the critical point. *Biophys. J.* 106:1970–1978.
24. Chiang, Y.-W., Y. Shimoyama, ..., J. H. Freed. 2004. Dynamic molecular structure of DPPC-DLPC-cholesterol ternary lipid system by spin-label electron spin resonance. *Biophys. J.* 87:2483–2496.
25. Ionova, I. V., V. A. Livshits, and D. Marsh. 2012. Phase diagram of ternary cholesterol/palmitoylsphingomyelin/palmitoyl-oleoyl-phosphatidylcholine mixtures: spin-label EPR study of lipid-raft formation. *Biophys. J.* 102:1856–1865.
26. Tokumasu, F., A. J. Jin, ..., J. A. Dvorak. 2003. Nanoscopic lipid domain dynamics revealed by atomic force microscopy. *Biophys. J.* 84:2609–2618.
27. Mills, T. T., S. Tristram-Nagle, ..., G. W. Feigenson. 2008. Liquid-liquid domains in bilayers detected by wide angle x-ray scattering. *Biophys. J.* 95:682–690.
28. Chen, L., Z. Yu, and P. J. Quinn. 2007. The partition of cholesterol between ordered and fluid bilayers of phosphatidylcholine: a synchrotron x-ray diffraction study. *Biochim. Biophys. Acta.* 1768:2873–2881.
29. Bennett, W. F. D., and D. P. Tieleman. 2013. Computer simulations of lipid membrane domains. *Biochim. Biophys. Acta.* 1828:1765–1776.
30. Akimov, S. A., P. I. Kuzmin, ..., Y. A. Chizmadzhev. 2004. An elastic theory for line tension at a boundary separating two lipid monolayer regions of different thickness. *J. Electroanal. Chem.* 564:13–18.
31. Khelashvili, G., B. Kollmitzer, ..., D. Harries. 2013. Calculating the bending modulus for multicomponent lipid membranes in different thermodynamic phases. *J. Chem. Theory Comput.* 9:3866–3871.
32. Rawicz, W., B. A. Smith, ..., E. Evans. 2008. Elasticity, strength, and water permeability of bilayers that contain raft microdomain-forming lipids. *Biophys. J.* 94:4725–4736.
33. Pabst, G., N. Kučerka, ..., J. Katsaras. 2010. Applications of neutron and x-ray scattering to the study of biologically relevant model membranes. *Chem. Phys. Lipids.* 163:460–479.
34. Pan, J., F. A. Heberle, ..., J. Katsaras. 2013. Using small-angle neutron scattering to detect nanoscopic lipid domains. *Chem. Phys. Lipids.* 170:171–19–32.
35. Heberle, F. A., R. S. Petruzielo, ..., J. Katsaras. 2013. Bilayer thickness mismatch controls domain size in model membranes. *J. Am. Chem. Soc.* 135:6853–6859.

36. Tsamaloukas, A., H. Szadkowska, and H. Heerklotz. 2006. Nonideal mixing in multicomponent lipid/detergent systems. *J. Phys. Condens. Matter*. 18:S1125–S1138.
37. Tayebi, L., Y. Ma, ..., A. N. Parikh. 2012. Long-range interlayer alignment of intralayer domains in stacked lipid bilayers. *Nat. Mater*. 11:1074–1080.
38. Karmakar, S., B. R. Sarangi, and V. A. Raghunathan. 2006. Phase behavior of lipid-cholesterol membranes. *Solid State Commun.* 139: 630–634.
39. Pabst, G., M. Rappolt, ..., P. Lagner. 2000. Structural information from multilamellar liposomes at full hydration: full q -range fitting with high quality x-ray data. *Phys. Rev. E Stat. Phys. Plasmas Fluids Relat. Interdiscip. Topics*. 62 (3 Pt B):4000–4009.
40. Kučerka, N., J. F. Nagle, ..., J. Katsaras. 2008. Lipid bilayer structure determined by the simultaneous analysis of neutron and x-ray scattering data. *Biophys. J.* 95:2356–2367.
41. Heftberger, P., B. Kollmitzer, ..., G. Pabst. 2014. Global small-angle x-ray scattering data analysis for multilamellar vesicles: the evolution of the scattering density profile model. *J. Appl. Cryst.* 47:173–180.
42. Hammersley, A. 1997. ESRF Internal Report, ESRF97HA02T, FIT2D: An Introduction and Overview. European Synchrotron Radiation Facility. Grenoble, France.
43. Glatter, O., and O. Kratky. 1982. Small Angle X-Ray Scattering, Vol. 102. Academic Press, London, United Kingdom.
44. Caillé, A. 1972. Notes on the distribution of x-rays in smectics [Remarques sur la diffusion des rayons x dans les smectiques A]. *Acad. Sci. Paris B.* 274:891–893.
45. Zhang, R., R. M. Suter, and J. F. Nagle. 1994. Theory of the structure factor of lipid bilayers. *Phys. Rev. E Stat. Phys. Plasmas Fluids Relat. Interdiscip. Topics*. 50:5047–5060.
46. Pabst, G., R. Koschuch, ..., P. Lagner. 2003. Structural analysis of weakly ordered membrane stacks. *J. Appl. Cryst.* 36:1378–1388.
47. Kučerka, N., M.-P. Nieh, and J. Katsaras. 2011. Fluid phase lipid areas and bilayer thicknesses of commonly used phosphatidylcholines as a function of temperature. *Biochim. Biophys. Acta.* 1808:2761–2771.
48. Pan, J., X. Cheng, ..., J. Katsaras. 2012. Interactions between ether phospholipids and cholesterol as determined by scattering and molecular dynamics simulations. *J. Phys. Chem. B.* 116:14829–14838.
49. Uppamoohikkal, P., S. Tristram-Nagle, and J. F. Nagle. 2010. Orientation of tie-lines in the phase diagram of DOPC/DPPC/cholesterol model biomembranes. *Langmuir*. 26:17363–17368.
50. Heberle, F. A., J. Wu, ..., G. W. Feigenson. 2010. Comparison of three ternary lipid bilayer mixtures: FRET and ESR reveal nanodomains. *Biophys. J.* 99:3309–3318.
51. Koenig, B. W., and K. Gawrisch. 2005. Specific volumes of unsaturated phosphatidylcholines in the liquid crystalline lamellar phase. *Biochim. Biophys. Acta.* 1715:65–70.
52. Greenwood, A. I., S. Tristram-Nagle, and J. F. Nagle. 2006. Partial molecular volumes of lipids and cholesterol. *Chem. Phys. Lipids.* 143:1–10.
53. Davis, J. H., J. J. Clair, and J. Juhasz. 2009. Phase equilibria in DOPC/DPPC-d62/cholesterol mixtures. *Biophys. J.* 96:521–539.
54. Veatch, S. L., O. Soubias, ..., K. Gawrisch. 2007. Critical fluctuations in domain-forming lipid mixtures. *Proc. Natl. Acad. Sci. USA.* 104: 17650–17655.
55. Veatch, S. L., I. V. Polozov, ..., S. L. Keller. 2004. Liquid domains in vesicles investigated by NMR and fluorescence microscopy. *Biophys. J.* 86:2910–2922.
56. Pan, J., S. Tristram-Nagle, and J. F. Nagle. 2009. Effect of cholesterol on structural and mechanical properties of membranes depends on lipid chain saturation. *Phys. Rev. E Stat. Nonlin. Soft Matter Phys.* 80:021931.
57. McConnell, H. M., and A. Radhakrishnan. 2003. Condensed complexes of cholesterol and phospholipids. *Biochim. Biophys. Acta.* 1610:159–173.
58. Hodzic, A., M. Rappolt, ..., G. Pabst. 2008. Differential modulation of membrane structure and fluctuations by plant sterols and cholesterol. *Biophys. J.* 94:3935–3944.
59. Pan, J., T. T. Mills, ..., J. F. Nagle. 2008. Cholesterol perturbs lipid bilayers nonuniversally. *Phys. Rev. Lett.* 100:198103.
60. Pabst, G., H. Amenitsch, ..., M. Rappolt. 2004. Structure and fluctuations of phosphatidylcholines in the vicinity of the main phase transition. *Phys. Rev. E Stat. Nonlin. Soft Matter Phys.* 70:021908.
61. Pabst, G., J. Katsaras, ..., M. Rappolt. 2003. Structure and interactions in the anomalous swelling regime of phospholipid bilayers. *Langmuir*. 19:1716–1722.
62. Parsegian, V. A., R. P. Rand, and D. C. Rau. 1995. Macromolecules and water: probing with osmotic stress. In *Energetics of Biological Macromolecules*, Vol. 259, Methods in Enzymology. M. L. Johnson and G. K. Ackers, editors. Academic Press, London, United Kingdom, pp. 43–94.
63. Buboltz, J. T., C. Bwalya, ..., M. Schutzer. 2007. High resolution mapping of phase behavior in a ternary lipid mixture: do lipid-raft phase boundaries depend on sample-prep procedure? *Langmuir*. 23:11968–11971.
64. Mouritsen, O. G., and K. Jørgensen. 1994. Dynamical order and disorder in lipid bilayers. *Chem. Phys. Lipids.* 73:3–25.
65. Honerkamp-Smith, A. R., P. Cicuta, ..., S. L. Keller. 2008. Line tensions, correlation lengths, and critical exponents in lipid membranes near critical points. *Biophys. J.* 95:236–246.
66. Honerkamp-Smith, A. R., B. B. Machta, and S. L. Keller. 2012. Experimental observations of dynamic critical phenomena in a lipid membrane. *Phys. Rev. Lett.* 108:265702.
67. Veatch, S. L., P. Cicuta, ..., B. Baird. 2008. Critical fluctuations in plasma membrane vesicles. *ACS Chem. Biol.* 3:287–293.
68. Connell, S. D., G. Heath, ..., A. Kasil. 2013. Critical point fluctuations in supported lipid membranes. *Faraday Discuss.* 161:91–150.
69. Kollmitzer, B., P. Heftberger, ..., G. Pabst. 2013. Monolayer spontaneous curvature of raft-forming membrane lipids. *Soft Matter*. 9:10877–10884.
70. Kučerka, N., J. Katsaras, and J. F. Nagle. 2010. Comparing membrane simulations to scattering experiments: introducing the SIMTOEXP software. *J. Membr. Biol.* 235:43–50.

Supporting Material

In situ determination of structure and fluctuations of coexisting fluid membrane domains

Peter Heftberger,^{†,‡} Benjamin Kollmitzer,^{†,‡} Alexander A. Rieder,^{†,‡} Heinz Amenitsch[§], and Georg Pabst^{†,‡} *

[†] University of Graz, Institute of Molecular Biosciences, Biophysics Division, NAWI Graz, Humboldtstr. 50/III, A-8010 Graz, Austria.

[‡] BioTechMed-Graz, Austria.

[§] Graz University of Technology, Institute of Inorganic Chemistry, Stremayrgasse 9/IV, A-8010 Graz, Austria.

* Correspondence: georg.pabst@uni-graz.at

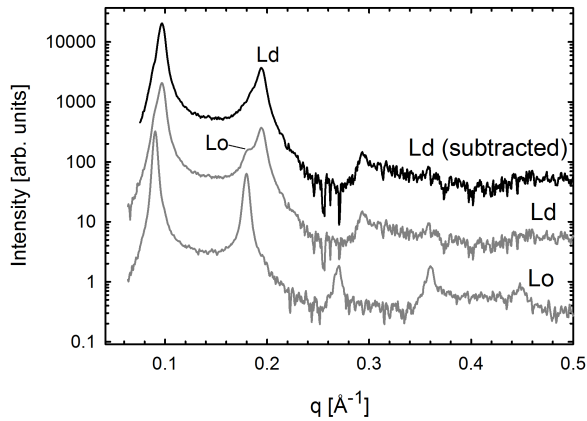


Figure S1: Subtraction of L_o contribution from L_d endpoint of B_{t2} . Scattering intensities are scaled by a constant for clarity. Second order Bragg reflections of L_o and L_d phases are indicated. Because of the overlap of L_o peaks for L_o and L_d endpoints (gray lines), we were able to subtract a fraction of L_o from the L_d endpoint sample. The result is shown in the top scattering pattern (black line).

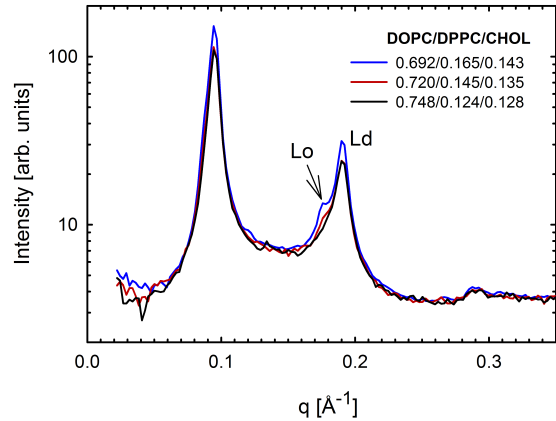


Figure S2: Determination of new L_d tieline endpoint for B_{t2} . Scattering patterns for three different lipid compositions, extending the B_{t2} tieline (1) toward the pure L_d regime (same angle), are shown. Data were recorded on a S3-Micro compact Kratky camera (Hecus X-ray Systems, Graz, Austria) at 15 °C. The second order Bragg peak clearly indicates L_o contamination. No residual L_o was observed for the DOPC/DPPC/CHOL composition 0.748/0.124/0.128 (molar fractions).

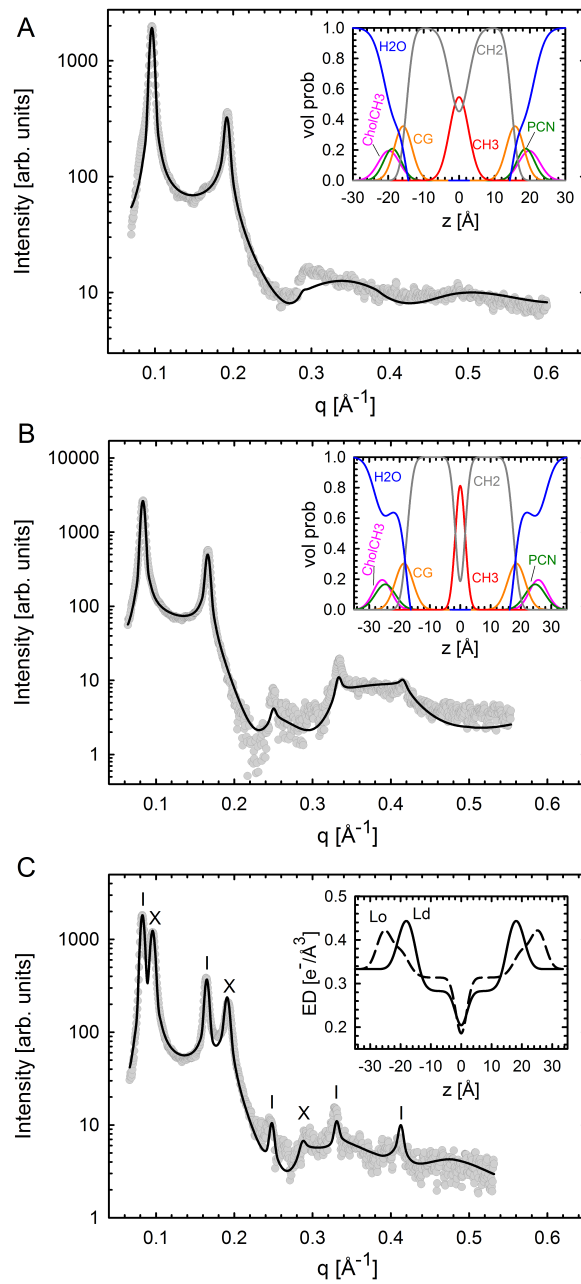


Figure S3: Validation of the global analysis for two coexisting phases for the A_{t2} tieline ($T = 22^\circ\text{C}$). Panels A and B show fits to L_d and L_o endpoint data, respectively. The insets to both panels give the derived volume probability distributions. Panel C shows the best fit to SAXS data at the A_{t2} tieline midpoint. Bragg reflections of L_o and L_d domains are indicated with dashes and crosses, respectively. The corresponding inset gives the ED profiles for L_o and L_d phases.

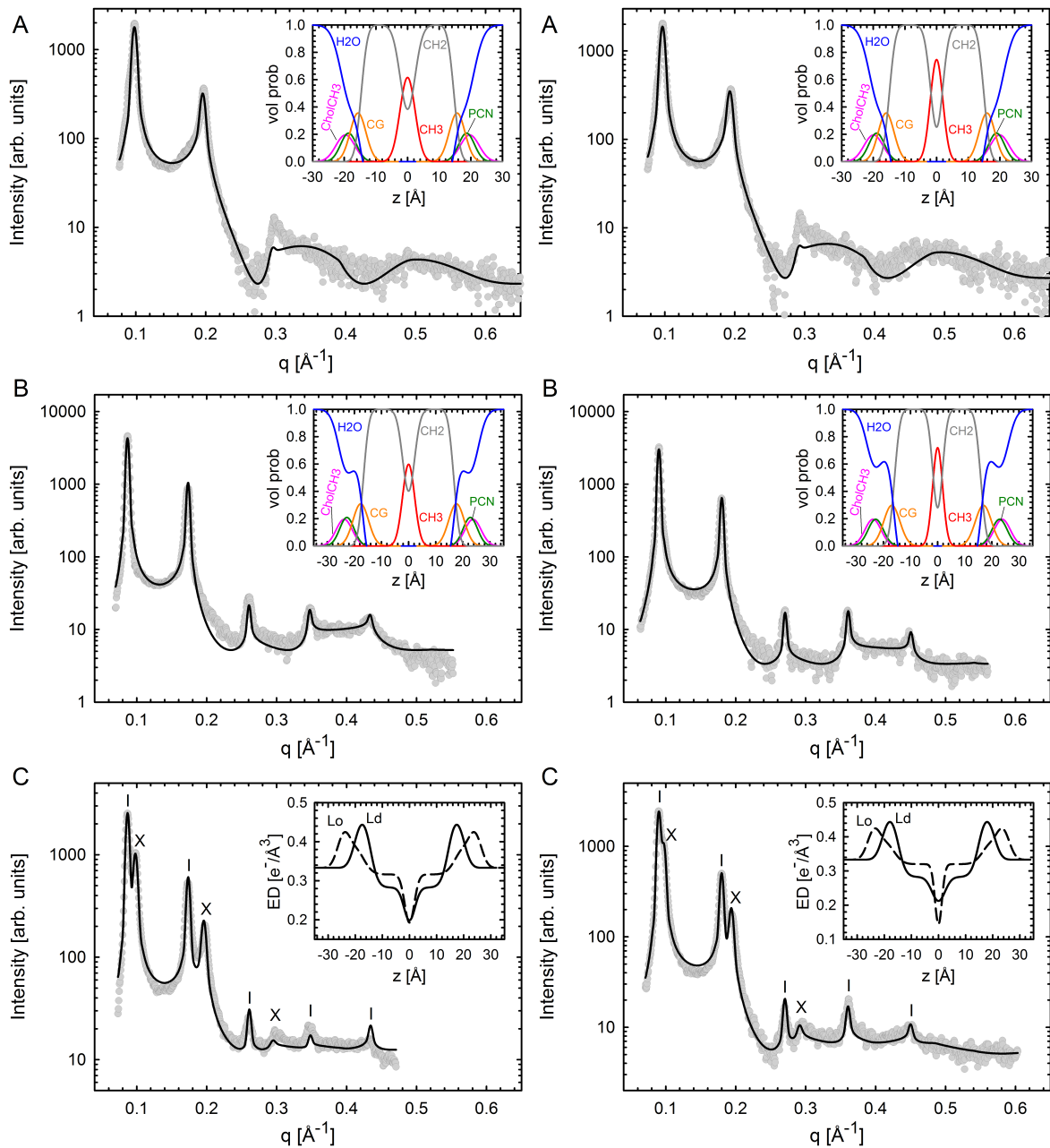


Figure S4: Validation of the global analysis for two coexisting phases for the B_{t1} tieline ($T = 15^\circ\text{C}$). Panels A and B show fits to L_d and L_o endpoint data, respectively. The insets to both panels give the derived volume probability distributions. Panel C shows the best fit to SAXS data at the B_{t1} tieline midpoint. Bragg reflections of L_o and L_d domains are indicated with dashes and crosses, respectively. The corresponding inset gives the ED profiles for L_o and L_d phases.

Figure S5: Validation of the global analysis for two coexisting phases for the B_{t2} tieline ($T = 15^\circ\text{C}$). Panels A and B show fits to L_d and L_o endpoint data, respectively. The insets to both panels give the derived volume probability distributions. Panel C shows the best fit to SAXS data at the B_{t2} tieline midpoint. Bragg reflections of L_o and L_d domains are indicated with dashes and crosses, respectively. The corresponding inset gives the ED profiles for L_o and L_d phases.

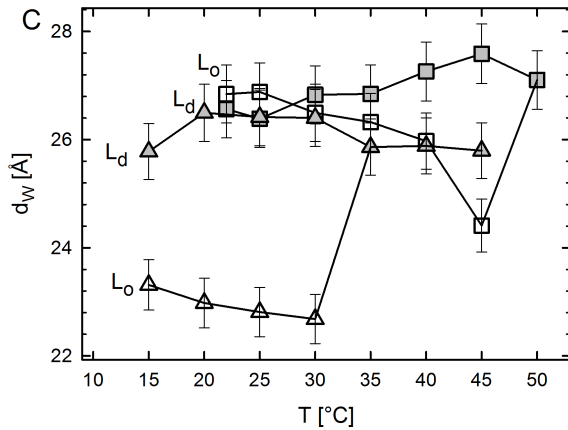
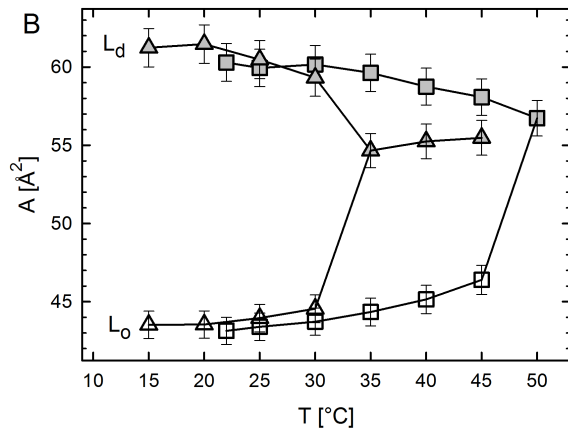
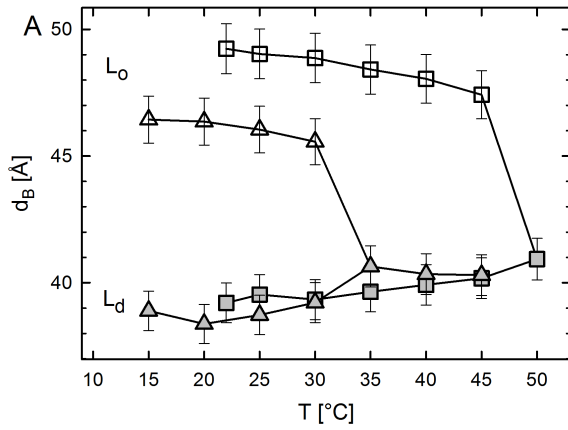


Figure S6: Temperature dependence of structural parameters of coexisting DOPC/DSPC/CHOL (squares) and DOPC/DPPC/CHOL (triangles) domains for t_2 tieline compositions (Fig. 1, Table S1). Panels A–C show the bilayer thickness, area per lipid, and water layer thickness, respectively for L_d (solid symbols) and L_o (open symbols) domains.

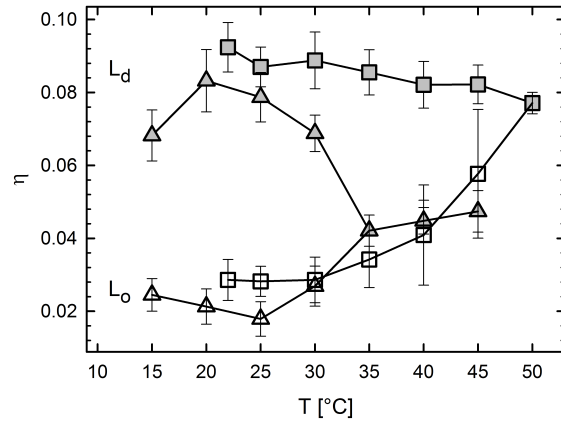


Figure S7: Temperature dependence of bending fluctuations of coexisting DOPC/DSPC/CHOL (squares) and DOPC/DPPC/CHOL (triangles) domains for t_2 tieline compositions (Fig. 1, Table S1). Solid symbols show results for L_d and open symbols for L_o domains, respectively.

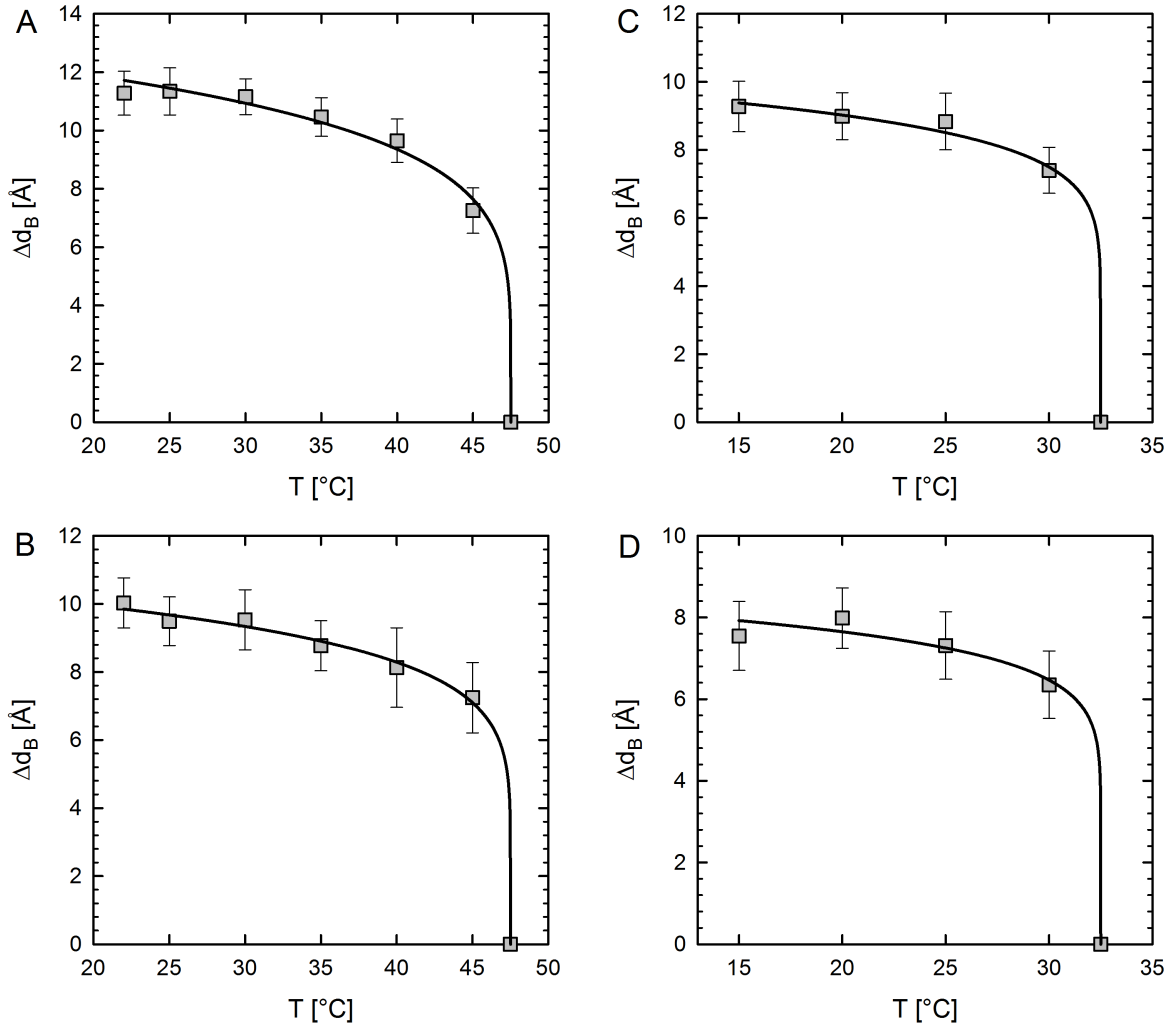


Figure S8: Critical behavior of height difference Δd_B between L_o and L_d domains of tieline midpoint samples A_{t1} (A), A_{t2} (B), B_{t1} (C) and B_{t2} (D). Solid lines correspond to the best fits using $\Delta d_B \propto (T_C - T)^\beta$. T_C was estimated to be 47.5°C for (A,B) and 32.5°C for (C,D) yielding the critical exponents $\beta_A = 0.18$, $\beta_B = 0.14$, $\beta_C = 0.115$ and $\beta_D = 0.105$. To evaluate the influence of our choice of T_C , T_C was varied between the extremes of the experimental temperature interval. For $T_C^{min} = 46/31^\circ\text{C}$ (for A,B/C,D), we obtained $\beta_A = 0.14$, $\beta_B = 0.11$, $\beta_C = 0.08$ and $\beta_D = 0.08$. For $T_C^{max} = 50/35^\circ\text{C}$ (for A,B/C,D), we found $\beta_A = 0.24$, $\beta_B = 0.19$, $\beta_C = 0.16$ and $\beta_D = 0.24$.

Table S1: Lipid compositions (molar fractions) of measured samples according to published compositional phase diagrams (1, 2). Two tielines with a lower (A_{t1}, B_{t1}) and higher (A_{t2}, B_{t2}) cholesterol concentration were studied (see Fig. 1).

		DOPC	DSPC	CHOL
A_{t1}	L_d	0.79	0.09	0.12
	L_o	0.05	0.65	0.30
	L_d/L_o	0.42	0.37	0.21
A_{t2}	L_d	0.74	0.09	0.17
	L_o	0.12	0.56	0.32
	L_d/L_o	0.46	0.30	0.24
		DOPC	DPPC	CHOL
B_{t1}	L_d	0.70	0.23	0.07
	L_o	0.11	0.68	0.21
	L_d/L_o	0.37	0.47	0.16
B_{t2}	L_d	0.66	0.19	0.15
	L_o	0.12	0.58	0.30
	L_d/L_o	0.36	0.41	0.23

Table S2: Structural results and bending fluctuations for the studied tieline endpoints. V_L are the calculated and V'_L the experimentally determined molecular volumes of an effective lipid molecule, including contributions from all three components (for details, see subsequent section). Parameter uncertainties are $< 2\%$.

	$d_B[\text{\AA}]$	$A[\text{\AA}^2]$	$d_W[\text{\AA}]$	$d_C[\text{\AA}]$	η	$V_L[\text{\AA}^3]$	$V'_L[\text{\AA}^3]$
$A_{t1}-L_d$	38.6	62.9	25.8	14.6	0.079	1215	1233
$A_{t1}-L_o$	48.6	44.2	26.9	18.2	0.047	1075	1063
$A_{t2}-L_d$	39.1	60.5	26.3	14.8	0.097	1183	1200
$A_{t2}-L_o$	48.0	44.3	27.4	17.9	0.060	1065	1058
$B_{t1}-L_d$	38.8	63.5	25.2	14.7	0.082	1231	1227
$B_{t1}-L_o$	46.6	44.9	25.8	17.4	0.027	1047	1049
$B_{t2}-L_d$	39.3	60.6	25.6	14.9	0.078	1191	1183
$B_{t2}-L_o$	45.9	44.0	23.7	17.0	0.028	1010	1015

Lipid volume calculation

The calculated lipid volumes of the ternary mixtures described in Material and Methods, were compared to experimentally determined volumes using the density sound analyzer DSA5000 (Anton Paar, Graz, Austria). Specifically, experiments yielded the partial specific volume (see e.g. (3))

$$v_s = \frac{1}{\rho_0} \left(1 - \frac{\rho_s - \rho_0}{c} \right), \quad (1)$$

where ρ_0 is the density of the solvent, ρ_s density of the solution and c the solute concentration. The experimental volume per molecule is then calculated according to Greenwood et al. as (4):

$$V'_L = \frac{v_s}{N_A} (x_1 M_1 + x_2 M_2 + x_3 M_3), \quad (2)$$

where N_A is Avogadro's number, x_i molar fraction and M_i the molecular weights.

Alternatively, volumes can be calculated by (5)

$$V_L(T) = V_H + n_{CH} V_{CH}(T) + n_{CH_2} V_{CH_2}(T) + n_{CH_3} V_{CH_3}(T), \quad (3)$$

where the head group volume V_H is kept fixed at 319 \AA^3 . V_{CH} , V_{CH_2} , V_{CH_3} are the segmental volumes of methine-, methylene-, and methyl groups and n_{CH} , n_{CH_2} , n_{CH_3} are the number of CH, CH₂, CH₃ groups per lipid molecule, respectively. A detailed description of the temperature dependence can be found in (5). Experimental and calculated molecular volumes were found to agree within experimental uncertainties (Table S2).

Estimation of temperature dependent compositional changes

Assuming that the inclination of tielines remains constant with temperature, tieline endpoints can be estimated using the lever rule. Specifically, we determined the distances between tieline midpoints and tieline endpoints \overline{Ld} , \overline{Lo} using

$$c_{Ld}(T) = \frac{\overline{Lo}(T)}{\overline{tl}(T)} \quad (4)$$

$$c_{Lo}(T) = 1 - c_{Ld}(T) = \frac{\overline{Ld}(T)}{\overline{tl}(T)}, \quad (5)$$

where $\overline{tl}(T)$ is the overall tieline length. \overline{tl} was estimated to change with temperature in proportion to the L_o fraction. Arbitrary functions were used to fit $c_{Ld}(T)$ data. Results are shown in Fig. S9. Estimates reproduce the asymmetric closing-in of the phase boundaries reported previously (6), which originate here from the measured increase of the L_d phase fraction.

Uppamoochikkal et al. (1) reported a small but significant increase of the tieline inclination angle with temperature. Therefore we checked, how this would influence our structural results. Note that this concerns only the area per lipid A , as results for all other parameter do not depend on knowing the specific lipid compositions of L_o/L_d domains. Hence, we tested several functions for the temperature behavior of the tielines, without finding any effects on the relative changes of A . Changes were observed for absolute values of A at the higher temperatures. However, they remained small, i.e. within $\pm 3\%$.

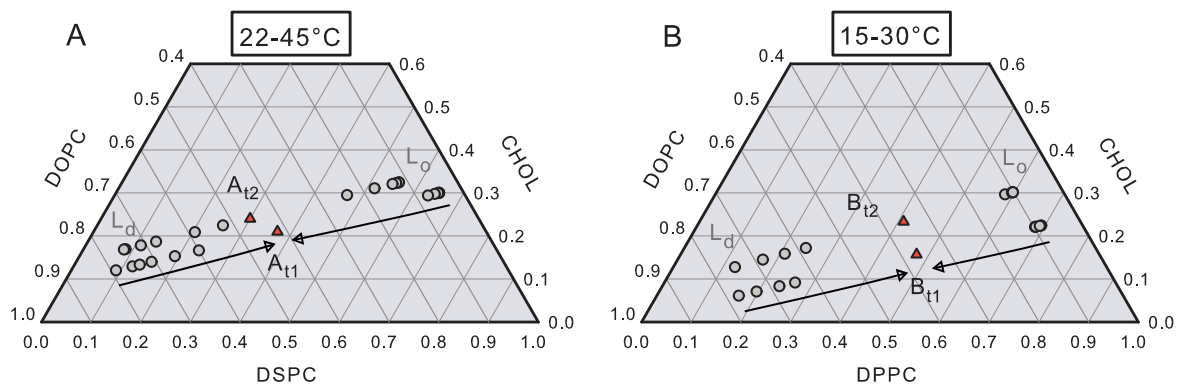


Figure S9: Estimated temperature dependence of tie-line endpoints for DOPC/DSPC/CHOL (panel A) and DOPC/DPPC/CHOL (panel B). Triangles represent starting points at the tie-line midpoints. Circles indicate the corresponding estimated tie-line endpoints, which shift toward the midpoints as temperature is increased. The temperature increment was 5°C only the first temperature step for DOPC/DSPC/CHOL was smaller (3°C). Note that L_d endpoints approach tie-line midpoints more rapidly than L_o endpoints.

Supporting References

1. Uppamoochikkal, P., S. Tristram-Nagle, and J. F. Nagle, 2010. Orientation of tie-lines in the phase diagram of DOPC:DPPC:cholesterol model biomembranes. *Langmuir* 26:17363–17368.
2. Heberle, F. A., J. Wu, S. L. Goh, R. S. Petruzielo, and G. W. Feigenson, 2010. Comparison of three ternary lipid bilayer mixtures: FRET and ESR reveal nanodomains. *Biophys. J.* 99:3309–3318.
3. Hodzic, A., M. Rappolt, H. Amenitsch, P. Laggner, and G. Pabst, 2008. Differential modulation of membrane structure and fluctuations by plant sterols and cholesterol. *Biophys. J.* 94:3935–3944.
4. Greenwood, A. I., S. Tristram-Nagle, and J. F. Nagle, 2006. Partial molecular volumes of lipids and cholesterol. *Chem. Phys. Lipids* 143:1–10.
5. Koenig, B. W., and K. Gawrisch, 2005. Specific volumes of unsaturated phosphatidylcholines in the liquid crystalline lamellar phase. *Biochim. Biophys. Acta.* 1715:65–70.
6. Buboltz, J. T., C. Bwalya, K. Williams, and M. Schutzer, 2007. High resolution mapping of phase behavior in a ternary lipid mixture: Do lipid-raft phase boundaries depend on sample-prep procedure? *arXiv:0706.1374 [physics]* arXiv: 0706.1374.